

2020

## Teasing apart excited-state intramolecular proton transfer (ESIPT) fluorescence: An evaluation of solvent, substituent, and aromaticity effects

Bryan Lampkin  
Iowa State University

Follow this and additional works at: <https://lib.dr.iastate.edu/etd>

### Recommended Citation

Lampkin, Bryan, "Teasing apart excited-state intramolecular proton transfer (ESIPT) fluorescence: An evaluation of solvent, substituent, and aromaticity effects" (2020). *Graduate Theses and Dissertations*. 18163.

<https://lib.dr.iastate.edu/etd/18163>

This Dissertation is brought to you for free and open access by the Iowa State University Capstones, Theses and Dissertations at Iowa State University Digital Repository. It has been accepted for inclusion in Graduate Theses and Dissertations by an authorized administrator of Iowa State University Digital Repository. For more information, please contact [digirep@iastate.edu](mailto:digirep@iastate.edu).

**Teasing apart excited-state intramolecular proton transfer (ESIPT) fluorescence: An evaluation of solvent, substituent, and aromaticity effects**

by

**Bryan J. Lampkin**

A dissertation submitted to the graduate faculty  
in partial fulfillment of the requirements for the degree of  
DOCTOR OF PHILOSOPHY

Major: Organic Chemistry

Program of Study Committee:  
Brett VanVeller, Major Professor  
Arthur H. Winter  
Levi M. Stanley  
Vincenzo Venditti  
Monica H. Lamm

The student author, whose presentation of the scholarship herein was approved by the program of study committee, is solely responsible for the content of this dissertation. The Graduate College will ensure this dissertation is globally accessible and will not permit alterations after a degree is conferred.

Iowa State University

Ames, Iowa

2020

Copyright © Bryan J. Lampkin, 2020. All rights reserved.

## DEDICATION

This is dedicated to my beautiful daughter, Graelynn Marie, of which, this thesis will always be older, but forever less important, than she will ever be.

## TABLE OF CONTENTS

	Page
LIST OF FIGURES .....	v
LIST OF TABLES .....	x
LIST OF SCHEMES .....	xi
ACKNOWLEDGMENTS .....	xii
ABSTRACT .....	xiv
CHAPTER 1. GENERAL INTRODUCTION .....	1
Introduction .....	1
Thesis Organization .....	5
References .....	7
CHAPTER 2. A DESIGNED PROTEIN BINDING-POCKET TO CONTROL EXCITED-STATE INTRAMOLECULAR PROTON TRANSFER FLUORESCENCE.....	11
Abstract.....	11
Introduction .....	12
Results and Discussion .....	17
Conclusion.....	24
Experimental.....	25
Synthetic Procedures .....	25
Expression and Purification of Wild-Type TTR and A108G-TTR.....	30
Fluorescence binding assay .....	30
Binding Studies of 3 and 5 in A108G Protein.....	33
References .....	36
CHAPTER 3. SUBSTITUENT EFFECTS ON THE PHOTOPHYSICAL PROPERTIES OF 2-(2'-HYDROXYPHENYL)-BENZOXAZOLE AND THEIR ROLE IN THE EXCITED-STATE INTRAMOLECULAR PROTON TRANSFER.....	40
Abstract.....	40
Introduction .....	40
Results and Discussion .....	44
Effect on absorption and emission .....	44
Effect on dual emission .....	50
Effect on the Stokes shift .....	52
Effect on $\Phi_f$ .....	54
Conclusion.....	55
Supplemental Data and Experimental Information .....	57
Measured spectroscopic data as a function of solvent polarity .....	57
Measured spectroscopic data as a function of functional group Hammett parameter ( $\sigma_p$ ).....	59
Quantum yield measurements .....	62

Synthetic Procedures .....	63
References .....	74
CHAPTER 4. DEMONSTRATION OF BAIRD'S RULE COMPLEMENTARITY IN THE SINGLET STATE WITH IMPLICATIONS FOR EXCITED-STATE INTRAMOLECULAR PROTON TRANSFER .....	
Abstract.....	79
Introduction .....	80
Results and Discussion .....	85
Conclusion.....	96
Experimental.....	97
Computational Details.....	97
Calculated Coordinates .....	101
References .....	105
CHAPTER 5. A MOLECULAR DOUBLE-MUTANT CYCLE TO UNTANGLE THE CONTRIBUTIONS OF AROMATICITY AND ELECTRONIC EFFECTS ON EXCITED-STATE INTRAMOLECULAR FLUORESCENCE .....	
Abstract.....	109
Introduction .....	109
Results and Discussion .....	114
Design of the linear free energy analysis .....	114
Effect of Aromaticity in ESIPT .....	118
Effect of Acidity in ESIPT .....	119
The confounding effects of Aromaticity and phenol Acidity on ESIPT Fluorescence....	121
Conclusion.....	122
Experimental Details .....	124
Computational Details.....	124
Computed Coordinates.....	125
References .....	133
CHAPTER 6. GENERAL CONCLUSIONS.....	136

## LIST OF FIGURES

	Page
Figure 1.1 (A) Common fluorescent scaffolds used in the development of chromophores. (B) Molecules that can undergo ESIPT due to their 6-membered conjugated hydrogen bond. ....	1
Figure 1.2 (A) Schematic of the ESIPT fluorescent process. (B) Sample emission spectra of HBO. Enol emission persists in protic solvents whereas keto emission is favored in aprotic solvents.....	2
Figure 2.1 (A) X-ray crystal structure of WT-transthyretin (WT-TTR) with bound Tafamidis (PDB 3tct). <sup>25</sup> (B) Zoom-in of the binding pocket of WT-TTR and Tafamidis in PDB 3tct showing close-contact residues. (C) Grafting of the ESIPT scaffold onto TTR binding molecules. ....	14
Figure 2.2 Emission traces of <b>3</b> in varying solvents. E* emission occurs 410–450 nm whereas K* emission is seen at 510 nm. Phosphate buffer consists 10 mM sodium phosphate (pH 7.6), 100 mM KCl, and 1 mM EDTA. ....	16
Figure 2.3 Proposed binding models of TTR mutants to ESIPT fluorophores. (A) An A108G TTR■ homotetramer displays an interface that can accommodate the phenolic moiety necessary for ESIPT. (B) A mixed WT-A108G heterotetramer interface (TTR□/ TTR■) designed to bind <b>3</b> and <b>5</b> . Images were prepared using the structure editing tools available in UCSF Chimera <sup>28</sup> on the original protein structure (PDB: 3TCT).....	16
Figure 2.4 Emission traces of (A) <b>5</b> and (B) <b>3</b> at 2.5 μM in buffer with 5.0 μM TTR (total protein concentration). Buffer = 10 nM sodium phosphate (pH 7.6), 100 nM KCl, 1 mM EDTA. ....	19
Figure 2.5 (A) <b>9</b> bound to TTR (PDB: 5TZL) <sup>26</sup> in a reversed orientation from that of Tafamidis (see Figure 1.1). (B) Proposed binding of <b>10</b> to the TTR□/ TTR■ mixed interface where TTR■ is on top. (C & D) The hydrophobic binding pocket with and without the A108G mutation. ....	22
Figure 2.6 Emission traces of (A) <b>11</b> and (B) <b>12</b> at 2.5 μM in buffer with 5.0 μM TTR (total protein concentration) with the exception of the trace in buffer, which was at a concentration of 25 μM. Buffer = 10 nM sodium phosphate (pH 7.6), 100 nM KCl, 1 mM EDTA. ....	24
Figure 2.7 Emission profiles of <b>3</b> in 5.0 μM WT, Mix, A108G and buffer solutions. ....	31
Figure 2.8 Emission profiles of <b>4</b> in 5.0 μM WT, Mix, A108G and buffer solutions. ....	31

Figure 2.9 Emission profiles of <b>5</b> in 5.0 $\mu\text{M}$ WT, Mix, A108G and buffer solutions. ....	32
Figure 2.10 Emission profiles of <b>6</b> in 5.0 $\mu\text{M}$ WT, Mix, A108G and buffer solutions. ....	32
Figure 2.11 Emission profiles of <b>7</b> in 5.0 $\mu\text{M}$ WT, Mix, A108G and buffer solutions. ....	32
Figure 2.12 Emission profiles of <b>8</b> in 5.0 $\mu\text{M}$ WT, Mix, A108G and buffer solutions. ....	33
Figure 2.13 Binding of <b>3</b> into 5 $\mu\text{M}$ A108G solution. Inset: Absorbances at four wavelengths. ....	34
Figure 2.14 Binding of <b>5</b> into 5 $\mu\text{M}$ A108G solution. Inset: Absorbances at four wavelengths. ....	34
Figure 2.15 Absorbances of <b>5</b> in buffer solution at two wavelengths. ....	35
Figure 3.1 The ESIPT photochemical cycle of HBO. <b>E</b> absorbs a photon and is excited to <b>E*</b> which can either radiatively relax to achieve enol emission or it can undergo ESIPT to <b>K*</b> . <b>K*</b> can then either radiatively relax to achieve keto emission or it can undergo TICT which subsequently non-radiatively relaxes back to <b>K</b> . ....	41
Figure 3.2 ESIPT HBO derivatives studied. $R_{1,2,3,4}$ represents the location of each of the 6 substituent groups utilized. ....	44
Figure 3.3 Functional group dependence at the $R_2$ position on the absorption, enol emission, and keto emission max in dioxane as a function of the para Hammett parameters ( $\sigma$ ). ....	49
Figure 3.4 Representative dual emission of HBO derivatives. (A) An $\text{NMe}_2$ substituent at the $R_2$ position induces more keto emission in more polar solvents. (B) The functional group at the $R_2$ position influences the normalized Keto:Enol ratio. Normalized ratios are such that a value of 1.0 indicates all keto emission and a value of 0.0 indicates all enol emission. ....	52
Figure 3.5 Effect on the Stokes shift of HBO analogs. (A) A qualitative schematic of the ESIPT potential energy surface using only measured absorption and emission values. The electronic or solvent coordinate can tune the keto emission and therefore the relative energies of <b>K</b> and <b>K*</b> . (B) Functional group dependence on the keto Stokes shift of $R_2$ derivatized HBO where EWG appear influence the Stokes shift more. ....	53

- Figure 3.6 Plots of the absorption ( $\bullet$ ), enol emission ( $\blacktriangle$ ), and keto emission ( $\blacksquare$ ) as a function of solvent polarity. Plots are organized by functional group (left to right, H, NO<sub>2</sub>, CN, Cl, Me, OMe, NMe<sub>2</sub>) and substituent location (top to bottom, R<sub>1</sub>, R<sub>2</sub>, R<sub>3</sub>, R<sub>4</sub>). ..... 57
- Figure 3.7 Plots of the normalized ratio of keto and enol emission as a function of solvent polarity. Plots are organized the same way as Figure 3.6. .... 57
- Figure 3.8 Plots of the Stokes shift of enol emission ( $\bullet$ ) and keto emission ( $\blacksquare$ ) as a function of solvent polarity. Plots are organized the same way as Figure 3.6..... 58
- Figure 3.9 Plots of quantum yield as a function of solvent polarity. Measurements were taken in triplicate in degassed solvent. Error bars are shown as  $\pm$  the standard error. Plots are organized the same way as Figure 3.6. .... 58
- Figure 3.10 Plots of the absorption ( $\bullet$ ), enol emission ( $\blacktriangle$ ), and keto emission ( $\blacksquare$ ) as a function of functional group  $\sigma_p$ . Plots are broken up by solvent (left to right, Dioxane, Dichloromethane, Methanol, Acetonitrile) and substituent location (top to bottom, R<sub>1</sub>, R<sub>2</sub>, R<sub>3</sub>, R<sub>4</sub>)..... 59
- Figure 3.11 Plots normalized ratio of keto and enol emission as a function of functional group  $\sigma_p$ . Plots are organized the same way as Figure 3.10 ..... 60
- Figure 3.12 Plots Stokes shift of enol emission ( $\bullet$ ) and keto emission ( $\blacktriangle$ ) as a function of functional group  $\sigma_p$ . Plots are organized the same way as Figure 3.10..... 61
- Figure 3.13 Plots of quantum yield as a function of functional group  $\sigma_p$ . Measurements were taken in triplicate in degassed solvent. Error bars are shown as  $\pm$  the standard error. Plots are organized the same way as Figure 3.10..... 62
- Figure 4.1 Excited-State Intramolecular Proton Transfer (ESIPT). Isomerization to the keto form closes the energy gap, red-shifts emission and creates a large Stokes shift. ... 81
- Figure 4.2 Absorbance and emission traces of HBO (solid) and Nap (dashed) in toluene. .... 82
- Figure 4.3 Excited-state intramolecular proton transfer (ESIPT). Isomerization to the keto form closes the energy gap, red-shifts emission and creates a large Stokes shift. ... 83
- Figure 4.4 Isotropic shielding contour plots 1 Å above the molecular (horizontal) plane for the the S<sub>0</sub> and S<sub>1</sub> states of benzene (left) and naphthalene (right).  $\sigma_{\text{iso}}(\mathbf{r})$  values were obtained using state-optimized  $\pi$ -space CASSCF(6,6)-GIAO/6-311+G\* and CASSCF(10,10)-GIAO/6-311+G\* wavefunctions for benzene and naphthalene respectively,  $\sigma_{\text{iso}}(\mathbf{r})$  in ppm, axes in Å. .... 87



- Figure 4.5 Isotropic shielding contour plots in the vertical plane slicing through the C-C bonds for the  $S_0$  and  $S_1$  states of benzene (left) and naphthalene (right). Same wavefunctions as for Figure 4.4,  $\sigma_{\text{iso}}(\mathbf{r})$  in ppm, axes in Å. .... 88
- Figure 4.6 Isotropic shielding contour plots in the molecular (horizontal) plane for the  $S_0$  and  $S_1$  states of benzene (left) and naphthalene (right). Same wavefunctions as for Figure 4.4,  $\sigma_{\text{iso}}(\mathbf{r})$  in ppm, axes in Å. .... 89
- Figure 4.7 Isotropic shielding difference plots between  $S_1$ - $S_0$  for benzene (left) and naphthalene (right) in three orientations described by Scheme 4.1: (A) same as for Figure 4.4; (B) same as for Figure 4.5; (C) same as for Figure 4.6. Same wavefunctions as for Figure 4.4,  $\sigma_{\text{iso}}(\mathbf{r})$  in ppm, axes in Å. .... 90
- Figure 4.8 Computed TD-DFT potential energy diagram for HBO and NAP (at the TD-DFT B3LYP/6-311+G(d,p) level). all vertical transitions are reported in nm with experimentally determined values from Table 4.1 provided in parentheses. Adiabatic energy differences reported in kcal mol<sup>-1</sup>. .... 91
- Figure 4.9 (A) Isomerization of Naphthalene ES IPT chromophores. Upon isomerization, the number of Clar sextets for **NAP** and **NAP-2** remains the same. (B) Overlaid absorption and emission profiles of naphthalene ES IPT chromophores. .... 95
- Figure 5.1(A) Schematic of the ES IPT photochemical process of HBO. Previous studies have implicated the importance of both the R substituent and the aromaticity of ring **a** in the ES IPT spectral properties. (B) Stabilization of phenolate via  $\pi$  electron delocalization to break aromaticity. .... 111
- Figure 5.2 (A) Diagram of a DMC analysis. Quantification of the interaction between  $i$  &  $j$  is accomplished by subtracting the sum of the individual mutants from the double mutant. (B) Envisioned molecular DMC where electron density is varied laterally and aromaticity is varied horizontally in the diagram. See below for a more detailed discussion. .... 114
- Figure 5.3 Double Mutant Cycle summary. The electron density (pKa) variants go left to right where the aromaticity variants go top to bottom. Full data can be found in X. Computational details and an explanation of the aromatic indices can be found in the experimental section. .... 117
- Figure 5.4 Normalized absorption and emission traces of **9-12** in toluene. (A) and (B) compare directly molecules that have the same electron density (*i.e.* same OH pKa) while varying the aromaticity of ring **a**. .... 119

- Figure 5.5 Normalized absorption and emission traces of **9-12** in toluene. (A) and (B) compare directly molecules that have the same aromaticity while varying the electron density of ring *a*. ..... 120
- Figure 5.6 Experimental Stokes shifts of HBO analogs in the proposed DMC analysis where the  $pK_a$  mutants run right to left and the aromaticity mutants run top to bottom. .... 121
- Figure 5.7 (A) Resonance stabilization of the non-aromatic isomer by delocalization of the nitrogen lone pair into the 5' electron withdrawing group. (B) An example of a RAHB where phenol aromaticity (*a*) and OH acidity dictates imine/enamine equilibrium. (C) Examples of AMHB where either a gain in ring aromaticity or relief in ring (anti)aromaticity strengthens hydrogen bonding. .... 123

## LIST OF TABLES

	Page
Table 3.1 Spectral properties of R <sub>1</sub> HBO derivatives .....	45
Table 3.2 Spectral properties of R <sub>2</sub> HBO derivatives .....	46
Table 3.3 Spectral properties of R <sub>3</sub> HBO derivatives .....	47
Table 3.4 Spectral properties of R <sub>4</sub> HBO derivatives .....	48
Table 4.1 Spectral data of ESIPT fluorophores in Toluene .....	83
Table 4.2 Spectroscopic properties of 2-(hydroxynaphthyl)-benzoxazole family.....	93
Table 1.3 TD-DFT functional screen of HBO S <sub>0</sub> – S <sub>1</sub> excitation. ....	101
Table 5.1 Aromatic index and electron density values for the DMC molecules .....	116

## LIST OF SCHEMES

Scheme 2.1 Benzoxazole candidates tested to selectively bind TTR to enhance ESIPT fluorescence.....	18
Scheme 2.2 Synthetic route towards starting aldehyde for the synthesis of <b>11</b> and <b>12</b> . (a) 1.1 eq POCl <sub>3</sub> , 1.3 eq. DMF, in Acetonitrile. (b) (1) Zn, THF, (2) Conc. HCl. ....	29
Scheme 2.3 Synthetic route towards starting 2-amino phenol for the synthesis of <b>12</b> . (a) AcOH/HNO <sub>3</sub> , -15° C (b) SnCl <sub>2</sub> , EtOH, N <sub>2</sub> , Conc. HCl.....	29
Scheme 4.1 Planes of contour plots in Figure 4.4-Figure 4.6.....	86
Scheme 4.2 Possible resonance forms of phenanthrene using Clar's Sextets .....	94
Scheme 5.1 Molecules used to evaluate the role of electron density and aromaticity of <i>a</i> on ESIPT. Electron density mutants goes left to right and aromaticity mutants run top to bottom.....	117

## ACKNOWLEDGMENTS

First and foremost, I would like to thank my advisor, Dr. Brett VanVeller, for all of your continued support over the last five years. You've taught me the importance of failing fast, thinking big, and the value of simply reading a (text)book. I appreciate your willingness (whether it was truly voluntary or not, I prefer not know) to let me push boundaries, even if it was outside of the confines of the group's collective expertise, and to run with a question or idea, even if it wasn't asked for. Your support and understanding as a mentor and colleague through the several life-altering events I've endured over the last five years made this PhD achievable. For all of this, and more – Thank you.

In addition, I would like to thank all of the members of the VanVeller group, present and past. All of the coffee runs, nights out, meme sharing, board games playing, potlucks consumed have all made the graduate school journey a pleasurable experience that I'd have no other way. Oh, the science and collaboration hasn't been bad, either.

Next, I would like to thank my POS committee – in no particular order, Dr. Art Winter, Dr. Levi Stanley, Dr. Vincenzo Venditti, and Dr. Monica Lamm. Your collective expertise has helped shaped the work I've accomplished during my graduate studies, whether it is included in this dissertation or not.

I would also like to thank the *MANY* collaborators, published and unpublished, that I have had the pleasure to work with. Again, in no particular order, Scott Carnahan, Amrit Vankatesh, Dr. Aaron Rossini, Kira Rahn, Dr. Robbyn Anand, Logan Fischer, Dr. Sarah Cady, Dr. Kamel Harrata, Dr. Andrew Severin, Dr. Maryam Sayadi, Dr. Cecelia Monteiro, Dr. Evan Powers, Dr. Gail Bartlett, and Dr. Peter Karadakov. It would be naïve of me to believe that I could be here today without the help from all of you.

This would not be a proper acknowledgement if I don't take the time to recognize and thank my parents. To my mom and dad – thank you for everything but especially for always pushing me to achieve my goals, even if I had my doubts.

Lastly, but certainly not the least, an immense amount of thanks needs to go out to my biggest fan and sturdiest rock, my wife, Hannah. Thank you for agreeing to move to Iowa with me, although you didn't have to. Thank you for supporting me in pursuing more schooling as opposed to seeking a *real* job like many of our friends. Thank you for lending your ear for me to express my excitement and many frustrations that came with graduate school. Thank you for your unwavering belief in me when the goings got rough. Thank you (and our dog, Zoey) for tolerating the late nights and long weekends away in the lab. Thank you for putting more than your fair share in taking care our daughter, Graelynn, (all while working from home!) in the final months of this degree so that I can finish on a good note. Thank you for letting me chase my dreams while many of yours may have been put on hold. Your sacrifices and patience do not go unappreciated and this degree is as much yours as it is mine. I love you.

## ABSTRACT

This dissertation presents my work towards the better understanding of the Excited-State Intramolecular Proton Transfer (ESIPT) photochemical process. ESIPT fluorescence is unique in a sense that it is environmentally sensitive and red-shifts a chromophore's emission by upwards of 100 nm. This photochemical process has been studied and applied extensively but several key features remain unaccounted for in the literature. For instance an ESIPT dye's sensitivity to a specific protein environment has not been explored which could inform probe development for a variety of applications. Additionally, the functional group tolerance and tunability, as well as governing factors in dictating the excited-state isomerization remain unmapped. First chapter of this dissertation is a brief overview of ESIPT fluorescence. The last chapter summarizes the previous four.

The second chapter is a study on the ESIPT properties of a fluorescent probe that binds specifically to a protein target. By engineering the binding site of a protein, it was demonstrated the emission wavelength of an ESIPT chromophore could be controlled by protein binding. This study highlighted the degree of sensitivity ESIPT dyes can provide by their dual emissive and ratiometric properties. The work highlighted in the chapter is a critical early step for the development of ESIPT chromophores for fluorescent-based medical diagnostics.

The third chapter characterizes the functional group tolerance of a class of ESIPT dyes. This study examined the photophysical properties of 25 unique monosubstituted ESIPT dyes in four different solvents. It was found that by functionalization at the 5' position of HBO dyes can influence most aspects of ESIPT fluorescent. This includes tuning the absorption and emission properties, degree of dual emission, Stokes shift, and the fluorescence brightness. This study also exposed limitations to the general *rules of ESIPT* such as its solvent dependence.

The fourth chapter is an exploration on the role aromaticity plays in ESIPT. Using a combined experimental and theoretical approach, we demonstrate that aromaticity is a key driving force in excited-state isomerization by means of Baird's rule. We showed that the degree of ground state aromaticity a molecule has, the more (anti)aromatic it becomes in the excited state and thus favors excited-state isomerization. This principle was then applied to example the puzzling photophysical behavior of naphthalene based ESIPT chromophores.

The fifth chapter presents a novel experimental method that is designed to disentangle the effects of a ring's aromaticity and its acidity, which is a measure of electron density, on an experimental parameter. We measured the spectral properties of a series of ESIPT dyes, of which, controlled for varying ring aromaticity and electron density. In applying this method to ESIPT fluorescence, it was concluded that, although both important in determining an ESIPT dye's photophysics, aromaticity and ring electron density function independently of one another.



## CHAPTER 1. GENERAL INTRODUCTION

### Introduction

Small molecule chromophores are essential for the continued advances in chemical biology. Although chromophore development is a large research focus for many, a majority of dyes are derived from a core set of scaffolds (Figure 1.1A).<sup>1,2</sup> These scaffolds are stitched together to assemble fluorescent probes that are employed to study the cytosolic localization of biological therapeutics<sup>3</sup> and cell membrane potential in neurons,<sup>4</sup> to name a few. What could be argued as the smallest scaffold, that doesn't nearly garner the attention it deserves, is a six-membered conjugated hydrogen bond. This relatively small functionality enables a fluorescent dye to undergo Excited-State Intramolecular Proton Transfer (ESIPT).<sup>5-7</sup> There are several classes of molecules that can undergo ESIPT (Figure 1.1B). However, the most common seems to be the chromophore, 2-(2'-Hydroxyphenyl)benzoxazole (HBO), and its thiazole (HBT) and imidazole (HBI) analogs.<sup>8</sup>

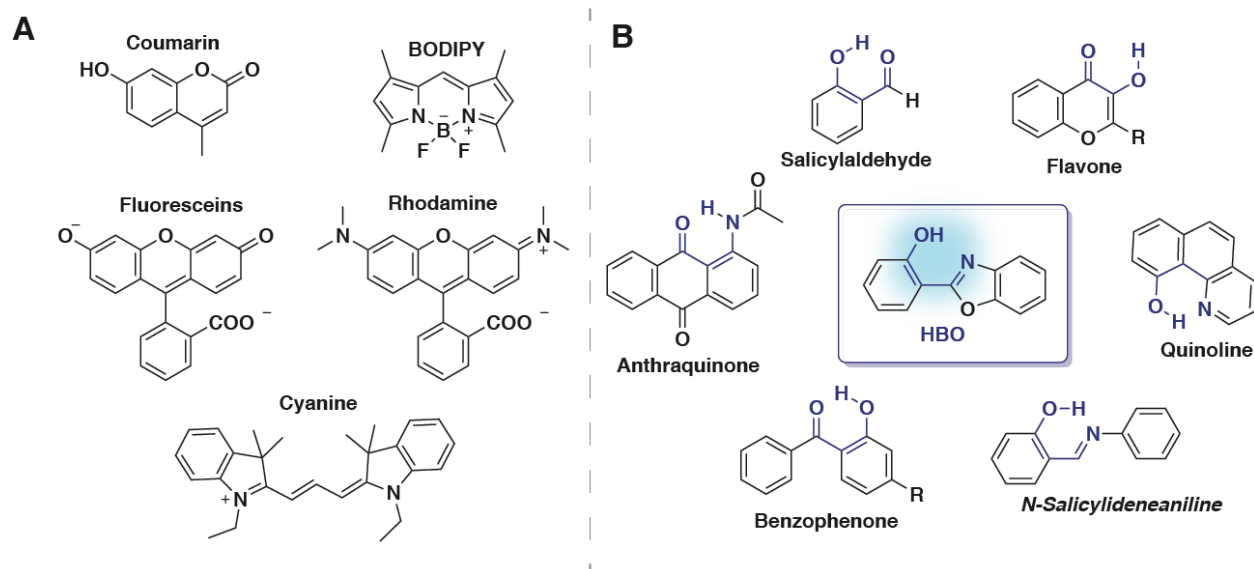


Figure 1.1 (A) Common fluorescent scaffolds used in the development of chromophores. (B) Molecules that can undergo ESIPT due to their 6-membered conjugated hydrogen bond.

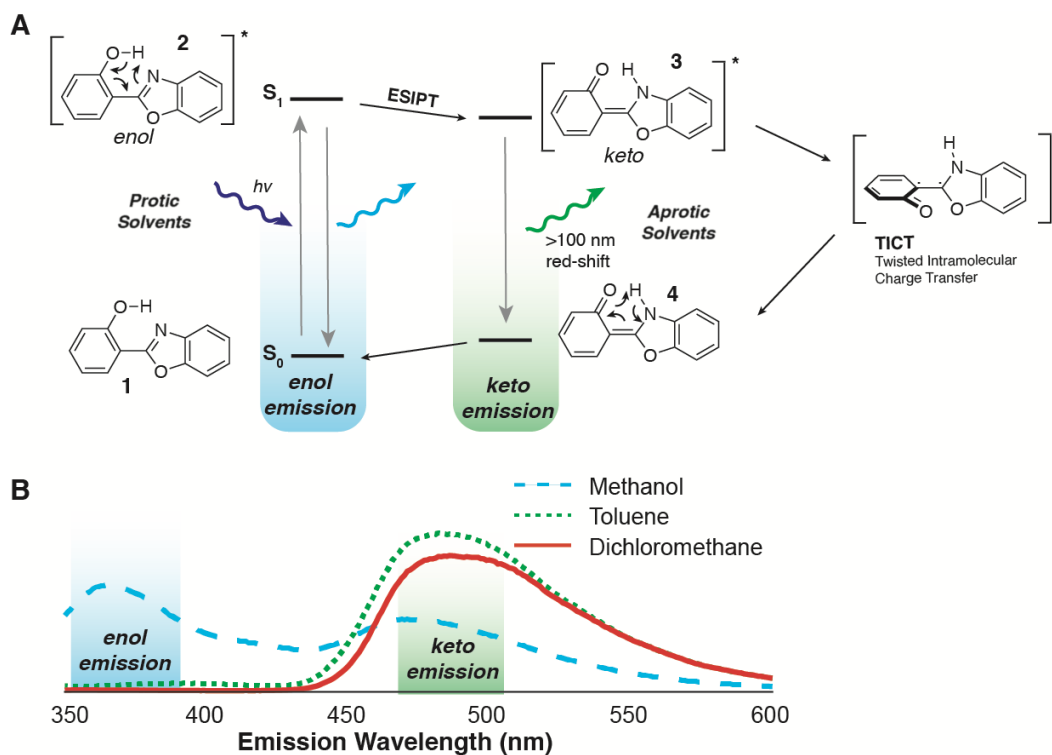


Figure 1.2 (A) Schematic of the ESIPT fluorescent process. (B) Sample emission spectra of HBO. Enol emission persists in protic solvents whereas keto emission is favored in aprotic solvents

To better understand the photochemical properties of HBO, consider **1** (Figure 1.2A). Upon the absorption of a photon, **1** will be excited from the singlet ground state (S<sub>0</sub>) into its lowest lying electronic excited state (S<sub>1</sub>), **2**. Once there, **2** can either relax back to the ground state, **1**, and emit a photon of light (commonly referred to as *enol* emission), or it can undergo ESIPT to **3**. This excited state isomerization is very rapid (picosecond timescale) and energetically favorable. **3** will then relax down to the ground state, **4**, emitting a photon of light at a red-shifted wavelength (commonly referred to as *keto* emission). **4** will then rapidly isomerize back to **1** in typical keto-enol tautomerization. Because the energy difference between **3** and **4** is lower than the difference between **1** and **2**, the light emitted from the keto form is typically red-shifted by approximately 100 nm! Considering the emission of the 2-

phenylbenoxazole without the proton donor OH group in the solid state (360 nm),<sup>9</sup> the simple addition of a hydroxyl group induces greater than a 200 nm Stokes shift.

ESIPT fluorescence is unique in that it is environmentally sensitive.<sup>10</sup> Once the molecule absorbs a photon of light and becomes excited to **2**, in protic solvents *enol* emission is favored due to the intermolecular hydrogen bonding to the solvent which will disfavor ESIPT. Conversely, in aprotic solvents, *keto* emission is favored (Figure 1.2B). The dual emission propensity of ESIPT dyes enables ratiometric outputs which increase measurement sensitivity. Additionally, albeit less characterized, HBO can undergo a twisted internal charge transfer (TICT) quenching mechanism when the two aryl systems rotate to become orthogonal to one another (Figure 1.2).<sup>11-13</sup> This nonradiative relaxation pathway enables another degree of environmental sensitivity. In bulk solution, this pathway, although not likely dominate, will nevertheless decrease ESIPT probe brightness. However, in the solid state or rigid environment, such as viscous solvents or a protein binding site, this pathway is inhibited and therefore increases fluorescent brightness.

To add yet another layer of environmental sensitivity to ESIPT is to discuss it with respect to a competing internal charge transfer (ITC) mechanism.<sup>14-16</sup> ITC often occurs in a standard *push-pull* chromophore where an electron donor group is in direct conjugation with an electron acceptor group and is manifested in a bathochromic shift in more polar solvents.<sup>10</sup> Within HBO, the phenol hydroxyl group can act as the donor and the nitrogen within the benzoxazole acts as the acceptor. While ITC of the bare HBO chromophore is minimal, the interplay between ESIPT and ITC is studied by substituent effect around the ring. Typically, an electron donor in the 4' position of HBO (para to the benzoxazole) induces ITC in the enol emission channel thus shutting down ESIPT.<sup>17</sup> It was discovered that a very strong dicyanovinyl

withdrawing group in the 6 position on the benzoxazole (para to the nitrogen) induces ITC *after* ESIPT.<sup>18</sup> While this confounding feature of HBO adds yet another layer of environmental sensitivity, applications to capitalize on ITC in HBO are slow to emerge.

The use of HBO chromophores is not novel. Many variations of HBO and its analogs are employed as analyte detectors for the sensing of small molecules, such as hydrogen sulfide,<sup>19</sup> or biological macromolecules, such as phosphatase MKP-6.<sup>20</sup> Many other examples of ESIPT in molecular sensing have been reviewed elsewhere.<sup>6, 10</sup>

Despite the continued and relatively frequent use of HBO ESIPT chromophores, its chemical properties are still poorly understood. For example, aside from a limited amount of standalone studies,<sup>8, 21, 22</sup> the functional group tolerance of HBO on ESIPT fluorescence still lacks direction. Further, although accepted in the mechanism, the molecular driving force for excited-state isomerization is not known despite a dearomatization process, which traditionally would be a highly unfavorable chemical step.<sup>23, 24</sup> Even the use of HBO in macromolecular sensing relies on weak, nonspecific interactions that ultimately limit the effectiveness of its ratiometric emission profiles.<sup>25, 26</sup> Demonstrating that HBO can *turn-on* keto emission and *turn-off* enol emission upon binding specifically to a target would only showcase the enhanced sensitivity ESIPT dyes provide as fluorescent probes.<sup>27</sup>

Yes, HBO ESIPT dyes have been studied for decades. It was, however, these gaps in knowledge that lead me down this rabbit hole that was poked and prodded and wrestled and wrangled and eventually forged into something that I will claim as my PhD dissertation. It is my goal (and to a greater degree, hope) that the work described herein will provide an overall better understanding into the molecular mechanism of ESIPT and trickle down into the improvement of this class of dyes for their more frequent use in the chemical sciences. Fluorescein was

discovered in 1871 by the German chemist, Adolf von Baeyer.<sup>28</sup> After nearly a century and a half, chemical modifications are still being made to its core to fine tune its photophysical properties<sup>29-31</sup> – maybe HBO simply needs more of *that* kind of love.

Please do note that the work described in this dissertation is not reflective of my entire graduate studies. Instead, I elected to piece this dissertation together to compile a more-or-less complete story from start to finish. During the last five years, in addition to the work on ESIPT fluorescence discussed here, I have conducted research, in a very collaborative manner, on a plethora of other topics. A non-exhaustive list includes the synthesis of thioamides in peptide backbones,<sup>32</sup> the altered hydrogen bonding properties of thioamides, using thioamides to stabilize peptide secondary structure, using thioamides to inhibit protein-protein interactions, hydrogen bonding at protein-protein interactions,<sup>33</sup> aromaticity of polyaromatic hydrocarbons,<sup>34</sup> resonance assisted hydrogen bonding,<sup>35</sup> benzothiadiazole (and derivatives) photochemistry,<sup>36-38</sup> electrochemistry using borinic acids,<sup>39</sup> and some <sup>17</sup>O NMR related things that I cannot speak more on other than that it involved isotopically labeling samples with what essentially amounts to a \$500,000 bottle of water.<sup>40, 41</sup>

### **Thesis Organization**

The following dissertation is comprised of six chapters. The first chapter, to no surprise, consists of a general introduction to ESIPT fluorescence and a concise overview of prior work done pertaining to HBO ESIPT chromophores. This chapter is not intended to be a thorough review but instead enough to establish the importance of the subsequent work to the reader.

Chapter II describes the development of a designed protein binding-pocket to control ESIPT fluorescence. In this study, we show that specific binding to a protein of an ESIPT chromophore induces a change in emission to a more red-shifted wavelength which is indicative of excited state isomerization induced by the desolvated environment of the protein binding-

pocket. As a result, the environmental sensitivity of an ESIPT dye is able to discern as subtle of a difference between an alanine and glycine at a protein-protein. This second chapter is modified based on data that was originally published in *Organic and Biomolecular Chemistry* in 2019.

Chapter III describes the study of functional group tolerance on HBO ESIPT photophysical properties in a Hammett-like analysis. In this study, we examine 25 unique monosubstituted HBO dyes and measured their spectral properties in four different solvents. To our knowledge, this is the most comprehensive study of electronic and solvent effects on ESIPT fluorescent properties. From this study, we elucidated the important and versatile role that substitution at the 5' position on the phenyl ring plays in tuning the spectral properties. By varying the substituent at the 5' position, the dual emission ratio, Stokes shift of the keto emission, and the quantum yield of fluorescence can be tuned. A lack of 5' substituted HBO dyes in the literature suggests that this privileged location on the HBO core has gone underappreciated. This chapter is modified from a manuscript in preparation.

Chapter IV describes an experimental and theoretical analysis into the role that aromaticity plays in ESIPT. In comparing HBO to a naphthalene analog of HBO, we elucidated aromaticity as a key driving force in ESIPT by means of Baird's rule - a molecule that is ground state aromatic becomes (anti)aromatic in its lowest lying excited state. To our knowledge, this was the first experimental demonstration of Baird's rule on the singlet surface. Within this study, we discovered a complementarity to Baird's rule where if a molecule is *more* ground state aromatic, it'll be *more* excited state (anti)aromatic. This relationship was used to explain the puzzling spectroscopic behaviors of naphthalene HBO isomers. This chapter is modified from a manuscript published in *Physical Chemistry Chemical Physics* in 2019.

Chapter V describes the development of an experimental method, inspired by a double mutant cycle, that enables the contributions of a molecule's aromaticity and electron density on a given experimental parameter. This method was applied to study the interplay between phenol aromaticity and acidity (an experimental manifestation of ring electron density) in ESIPT fluorescence. By systematically altering the phenol ring's aromaticity and electron density, as a function of phenol  $pK_a$ , we found that aromaticity and electron density of the phenol ring function independently in influencing HBO ESIPT emission. Although an interesting observation in ESIPT using a novel analysis, this method is still in its infancy and needs further use in other chemical systems to validate its efficiency.

Chapter VI simply provides general conclusions to the prior 5 chapters.

### References

1. Lavis, L. D.; Raines, R. T., Bright building blocks for chemical biology. *ACS Chem Biol* **2014**, *9* (4), 855-66.
2. Lavis, L. D.; Raines, R. T., Bright Ideas for Chemical Biology. *ACS Chemical Biology* **2008**, *3* (3), 142-155.
3. Peraro, L.; Deprey, K. L.; Moser, M. K.; Zou, Z.; Ball, H. L.; Levine, B.; Kritzer, J. A., Cell Penetration Profiling Using the Chloroalkane Penetration Assay. *Journal of the American Chemical Society* **2018**, *140* (36), 11360-11369.
4. Miller, E. W., Small molecule fluorescent voltage indicators for studying membrane potential. *Current Opinion in Chemical Biology* **2016**, *33*, 74-80.
5. Zhou, P.; Han, K., Unraveling the Detailed Mechanism of Excited-State Proton Transfer. *Acc Chem Res* **2018**, *51* (7), 1681-1690.
6. Sedgwick, A. C.; Wu, L.; Han, H. H.; Bull, S. D.; He, X. P.; James, T. D.; Sessler, J. L.; Tang, B. Z.; Tian, H.; Yoon, J., Excited-state intramolecular proton-transfer (ESIPT) based fluorescence sensors and imaging agents. *Chem Soc Rev* **2018**, *47* (23), 8842-8880.
7. Zhao, J.; Ji, S.; Chen, Y.; Guo, H.; Yang, P., Excited state intramolecular proton transfer (ESIPT): from principal photophysics to the development of new chromophores and applications in fluorescent molecular probes and luminescent materials. *Phys Chem Chem Phys* **2012**, *14* (25), 8803-17.

8. Azarias, C.; Budzak, S.; Laurent, A. D.; Ulrich, G.; Jacquemin, D., Tuning ESIPT fluorophores into dual emitters. *Chem Sci* **2016**, *7* (6), 3763-3774.
9. Carayon, C.; Fery-Forgues, S., 2-Phenylbenzoxazole derivatives: a family of robust emitters of solid-state fluorescence. *Photochemical & Photobiological Sciences* **2017**, *16* (7), 1020-1035.
10. Klymchenko, A. S., Solvatochromic and Fluorogenic Dyes as Environment-Sensitive Probes: Design and Biological Applications. *Acc Chem Res* **2017**, *50* (2), 366-375.
11. Grabowski, Z. R.; Rotkiewicz, K.; Rettig, W., Structural Changes Accompanying Intramolecular Electron Transfer: Focus on Twisted Intramolecular Charge-Transfer States and Structures. *Chemical Reviews* **2003**, *103* (10), 3899-4032.
12. Pijeu, S.; Foster, D.; Hohenstein, E. G., Excited-State Dynamics of 2-(2'-Hydroxyphenyl)benzothiazole: Ultrafast Proton Transfer and Internal Conversion. *The Journal of Physical Chemistry A* **2017**, *121* (24), 4595-4605.
13. Kim, S.; Seo, J.; Park, S. Y., Torsion-induced fluorescence quenching in excited-state intramolecular proton transfer (ESIPT) dyes. *Journal of Photochemistry and Photobiology A: Chemistry* **2007**, *191* (1), 19-24.
14. Hsieh, C.-C.; Jiang, C.-M.; Chou, P.-T., Recent Experimental Advances on Excited-State Intramolecular Proton Coupled Electron Transfer Reaction. *Accounts of Chemical Research* **2010**, *43* (10), 1364-1374.
15. Demchenko, A. P.; Tang, K.-C.; Chou, P.-T., Excited-state proton coupled charge transfer modulated by molecular structure and media polarization. *Chemical Society Reviews* **2013**, *42* (3), 1379-1408.
16. Hammes-Schiffer, S.; Stuchebrukhov, A. A., Theory of Coupled Electron and Proton Transfer Reactions. *Chemical Reviews* **2010**, *110* (12), 6939-6960.
17. Wiethaus, G.; Toldo, J. M.; da Silveira Santos, F.; da Costa Duarte, R.; Gonçalves, P. F. B.; Rodembusch, F. S., Experimental and theoretical investigation of long-wavelength fluorescence emission in push-pull benzazoles: intramolecular proton transfer or charge transfer in the excited state? *Phys Chem Chem Phys* **2019**, *21* (8), 4408-4420.
18. Seo, J.; Kim, S.; Park, S. Y., Strong solvatochromic fluorescence from the intramolecular charge-transfer state created by excited-state intramolecular proton transfer. *J Am Chem Soc* **2004**, *126* (36), 11154-5.
19. Brito da Silva, C.; Gil, E. S.; da Silveira Santos, F.; Morás, A. M.; Steffens, L.; Bruno Gonçalves, P. F.; Moura, D. J.; Lüdtkke, D. S.; Rodembusch, F. S., Proton-Transfer-Based Azides with Fluorescence Off-On Response for Detection of Hydrogen Sulfide: An Experimental, Theoretical, and Bioimaging Study. *The Journal of Organic Chemistry* **2018**, *83* (24), 15210-15224.



20. Kim, T.-I.; Kang, H. J.; Han, G.; Chung, S. J.; Kim, Y., A highly selective fluorescent ESIPT probe for the dual specificity phosphatase MKP-6. *Chemical Communications* **2009**, (39), 5895-5897.
21. Alarcos, N.; Gutierrez, M.; Liras, M.; Sánchez, F.; Douhal, A., An abnormally slow proton transfer reaction in a simple HBO derivative due to ultrafast intramolecular-charge transfer events. *Physical Chemistry Chemical Physics* **2015**, *17* (25), 16257-16269.
22. Alarcos, N.; Gutiérrez, M.; Liras, M.; Sánchez, F.; Moreno, M.; Douhal, A., Direct observation of breaking of the intramolecular H-bond, and slowing down of the proton motion and tuning its mechanism in an HBO derivative. *Physical Chemistry Chemical Physics* **2015**, *17* (22), 14569-14581.
23. Lampkin, B. J.; Nguyen, Y. H.; Karadakov, P. B.; VanVeller, B., Demonstration of Baird's rule complementarity in the singlet state with implications for excited-state intramolecular proton transfer. *Phys Chem Chem Phys* **2019**, *21* (22), 11608-11614.
24. Wu, C.-H.; Karas, L. J.; Ottosson, H.; Wu, J. I.-C., Excited-state proton transfer relieves antiaromaticity in molecules. **2019**, (116), 20303-20308.
25. Jiang, N.; Yang, C.; Dong, X.; Sun, X.; Zhang, D.; Liu, C., An ESIPT fluorescent probe sensitive to protein  $\alpha$ -helix structures. *Organic & Biomolecular Chemistry* **2014**, *12* (28), 5250-5259.
26. Enander, K.; Choulier, L.; Olsson, A. L.; Yushchenko, D. A.; Kanmert, D.; Klymchenko, A. S.; Demchenko, A. P.; Mély, Y.; Altschuh, D., A peptide-based, ratiometric biosensor construct for direct fluorescence detection of a protein analyte. *Bioconjug Chem* **2008**, *19* (9), 1864-70.
27. Lampkin, B. J.; Monteiro, C.; Powers, E. T.; Bouc, P. M.; Kelly, J. W.; VanVeller, B., A designed protein binding-pocket to control excited-state intramolecular proton transfer fluorescence. *Org Biomol Chem* **2019**, *17* (5), 1076-1080.
28. Lavis, L. D., Teaching Old Dyes New Tricks: Biological Probes Built from Fluoresceins and Rhodamines. *Annual Review of Biochemistry* **2017**, *86* (1), 825-843.
29. Deo, C.; Abdelfattah, A. S.; Bhargava, H. K.; Berro, A. J.; Falco, N.; Moeyaert, B.; Chupanova, M.; Lavis, L. D.; Schreiter, E. R., Bright and tunable far-red chemigenetic indicators. *bioRxiv* **2020**, 2020.01.08.898783.
30. Zheng, Q.; Ayala, A. X.; Chung, I.; Weigel, A. V.; Ranjan, A.; Falco, N.; Grimm, J. B.; Tkachuk, A. N.; Wu, C.; Lippincott-Schwartz, J.; Singer, R. H.; Lavis, L. D., Rational Design of Fluorogenic and Spontaneously Blinking Labels for Super-Resolution Imaging. *ACS Central Science* **2019**, *5* (9), 1602-1613.

31. Grimm, J. B.; English, B. P.; Chen, J.; Slaughter, J. P.; Zhang, Z.; Revyakin, A.; Patel, R.; Macklin, J. J.; Normanno, D.; Singer, R. H.; Lionnet, T.; Lavis, L. D., A general method to improve fluorophores for live-cell and single-molecule microscopy. *Nat Methods* **2015**, *12* (3), 244-50, 3 p following 250.
32. Camacho, L. A.; Lampkin, B. J.; VanVeller, B., A Bottom-Up Approach To Preserve Thioamide Residue Stereochemistry during Fmoc Solid-Phase Peptide Synthesis. *Organic Letters* **2019**, *21* (17), 7015-7018.
33. Lampkin, B. J.; VanVeller, B., Hydrogen Bond and Geometry Effects of Thioamide Backbone Modifications. *Submitted* **2020**.
34. Lampkin, B. J.; Karadakov, P. B.; VanVeller, B., Detailed Visualization of Aromaticity Using Isotropic Magnetic Shielding. *Submitted* **2020**.
35. Nguyen, Y. H.; Lampkin, B. J.; Venkatesh, A.; Ellern, A.; Rossini, A. J.; VanVeller, B., Open-Resonance-Assisted Hydrogen Bonds and Competing Quasiaromaticity. *J Org Chem* **2018**, *83* (17), 9850-9857.
36. Norris, S.; Warner, C. C.; Thooft, A. M.; Demirci, S. K.; Lampkin, B. J.; Miner, K.; Ellern, A.; VanVeller, B., Blue-Light Photocleavable Protecting Groups Based on Benzothiadiazole Scaffolds. *Organic Letters* **2020**, *22* (1), 270-273.
37. Warner, C. C.; Thooft, A. M.; Norris, S. R.; Lampkin, B. J.; Demirci, S. K.; VanVeller, B., The Malleable Excited States of Benzothiadiazole Dyes and Investigation of their Potential for Photochemical Control. *ChemistrySelect* **2020**, *5* (23), 7016-7020.
38. Norris, S. R.; Warner, C. C.; Lampkin, B. J.; Bouc, P.; VanVeller, B., Synthesis and Spectral Properties of Push–Pull Dyes Based on Isobenzofuran Scaffolds. *Organic Letters* **2019**, *21* (10), 3817-3821.
39. Robole, Z. M.; Rahn, K. L.; Lampkin, B. J.; Anand, R. K.; VanVeller, B., Tuning the Electrochemical Redox Potentials of Catechol with Boronic Acid Derivatives. *The Journal of Organic Chemistry* **2019**, *84* (4), 2346-2350.
40. Wijesekara, A. V.; Venkatesh, A.; Lampkin, B. J.; VanVeller, B.; Lubach, J. W.; Nagapudi, K.; Hung, I.; Gor'kov, P. L.; Gan, Z.; Rossini, A. J., Fast Acquisition of Proton-Detected HETCOR Solid-State NMR Spectra of Quadrupolar Nuclei and Rapid Measurement of NH Bond Lengths by Frequency Selective HMQC and RESPDOR Pulse Sequences. *Chemistry – A European Journal* **2020**, *26* (35), 7881-7888.
41. Carnahan, S. L.; Lampkin, B. J.; Naik, P.; Hanrahan, M. P.; Slowing, I. I.; VanVeller, B.; Wu, G.; Rossini, A. J., Probing O–H Bonding through Proton Detected 1H–17O Double Resonance Solid-State NMR Spectroscopy. *Journal of the American Chemical Society* **2019**, *141* (1), 441-450.

## CHAPTER 2. A DESIGNED PROTEIN BINDING-POCKET TO CONTROL EXCITED-STATE INTRAMOLECULAR PROTON TRANSFER FLUORESCENCE

Bryan J. Lampkin,<sup>a</sup> Cecilia Monteiro,<sup>b</sup> Evan T. Powers,<sup>b</sup> Paige M. Bouc,<sup>a</sup> Jeffery W. Kelly,<sup>b</sup>

Brett VanVeller,<sup>\*a</sup>

<sup>a</sup> Department of Chemistry, Iowa State University, Ames, Iowa 50011, USA

<sup>b</sup> Department of Chemistry, Skaggs Institute for Chemical Biology, The Scripps Research Institute, La Jolla, California 92037, USA

Modified from a manuscript published in *Organic and Biomolecular Chemistry*, **2019**,  
17, 1076-1080

Copyright © 2019 Royal Society of Chemistry

### Abstract

Excited-state intramolecular proton transfer involves a photochemical isomerization and creates the opportunity for the emission of two distinct wavelengths of light from a single fluorophore. The selectivity between these two wavelengths of emission is dependent on the environment around the fluorophore and suggests the possibility for ratiometric monitoring of protein microenvironments. Unfortunately, non-specific binding of ESIPT fluorophores does not often lead to dramatic changes in the ratio between the two wavelengths of emission. A protein binding pocket was designed to selectively discriminate between the two channels of emission available to an ESIPT fluorophore. This work is significant because it demonstrates that specific interactions between the protein and the fluorophore are essential to realize strong ratiometric differences between the two possible wavelengths of emission. The design strategies proposed here lead to an ESIPT fluorophore that can discern subtle differences in the interface between two proteins

## Introduction

The environment around a molecule can have a pronounced effect on its excited state and is frequently used in nature to control and manipulate photophysical outcomes. One example is the first step of vision, where the photoisomerization of retinal is governed by the microenvironment of opsin proteins.<sup>1,2</sup> Another example is the fluorophore of green fluorescent protein that is only emissive when packaged inside of the folded protein.<sup>3,4</sup> Because photochemistry is a zero-sum competition of the rates of different excited state processes, the manipulation of those rates by the environment can select which pathway is dominant. In particular, a photo-reaction known as excited-state intramolecular proton transfer (ESIPT) has attracted considerable attention because the ESIPT process affords the potential for two different wavelengths of light from the same molecule depending on local environmental conditions (Fig. 1).<sup>5-8</sup> We sought to design a protein binding pocket that could predictably and selectively distinguish between different excited-state pathways of the ESIPT process. The result of this work is a fluorescent probe that exhibits a change fluorescence signal by detecting subtle changes in a protein–protein interface.

Several characteristics of the ESIPT process make it attractive as a tool in fluorescence detection:

(i) The excited-state isomerization from 1-E\* to 1-K\* is ultra- fast ( $\sim$ ps)—faster than fluorescence from the enol tautomer ( $\sim$ ns)—leading to a predominance of keto fluorescence.<sup>8</sup> Because the energy gap between the keto forms ( $S_1' \rightarrow S_0'$ ) is smaller than for the enol forms ( $S_1 \rightarrow S_0$ ), keto fluorescence typically leads to a  $>100$  nm red-shift relative to enol fluorescence and the excitation wavelength. The ESIPT process therefore produces remarkably large Stokes shifts relative to “normal” fluorophores (e.g. fluorescein, rhodamine, BODIPY, etc.).

(ii) The ESIPT process is also sensitive to environmental factors. Enol emission tends to dominate in polar-protic solvents, presumably due to hydrogen bonding that disrupts the intramolecular isomerization from 1-E\* to 1-K\*. Alternatively, non-polar solvents or local desolvation from polar-protic solvents allows the excited-state isomerization to proceed—effectively turning on keto emission. The environmental dependence of the excited state isomerization process allows for a dual-emission readout. This multichannel output adds ratiometric characteristics to ESIPT capable dyes which enhance assay sensitivity and are self-calibrating.<sup>9</sup>

The ratiometric difference between enol and keto emission was originally demonstrated by Sytnik and Kasha<sup>10</sup> to interrogate the local desolvation effects upon nonspecific binding to human serum albumin. More recent studies have expanded on this work in various albumin proteins.<sup>11-15</sup> ESIPT fluorophores have also been incorporated into non-natural amino acids to detect peptide/nucleic acid interactions,<sup>16, 17</sup> protein secondary structure,<sup>18, 19</sup> and detection of  $\alpha$ -synuclein aggregation.<sup>20, 21</sup>

A limitation of the above studies was that only relatively subtle changes in the enol and keto fluorescence ratios were observed. This general lack of sensitivity arose from a common theme of ESIPT schemes reported to date: (i) The assay relied on non-specific binding of the ESIPT chromophore to the target of interest. (ii) When the ESIPT reporter was conjugated to a molecule that provides selectivity for the intended target, this construct meant that the environmentally sensitive ESIPT fluorophore did not directly interact with the target. Thus, any environmental changes experienced by the ESIPT fluorophore were largely an outer-sphere effect. Furthermore, conjugating a chromophore onto a specific binding ligand can often lead to a decrease in binding affinity, selectivity and sensitivity to the target.<sup>22</sup> The goal of this study was

to design a protein that could bind an ESIPT fluorophore and selectively alter the enol and keto fluorescence signals through the specific interactions that take place between the small molecule and protein binding partner.

We elected to use the well-studied tetrameric transthyretin (TTR) protein (Figure 2.1A).<sup>23,24</sup> To facilitate the discussion, we will employ a symbol convention to distinguish between the two kinds of TTR proteins under consideration.

TTR□ denotes the WT-TTR protein subunit.

TTR■ denotes the A108G mutant TTR protein subunit.

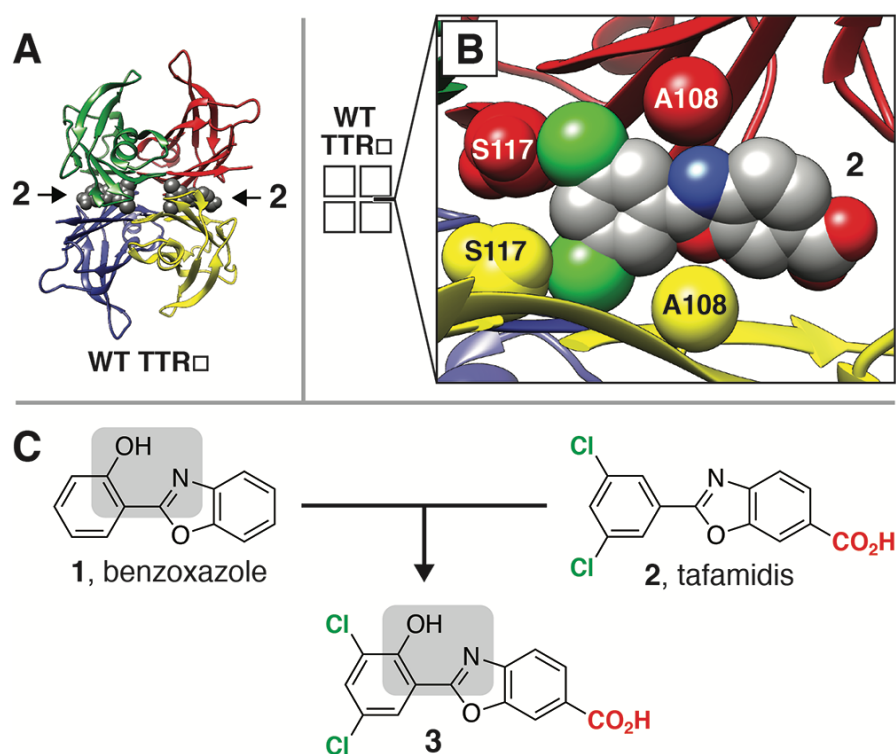


Figure 2.1 (A) X-ray crystal structure of WT-transthyretin (WT-TTR) with bound Tafamidis (PDB 3tct).<sup>25</sup> (B) Zoom-in of the binding pocket of WT-TTR and Tafamidis in PDB 3tct showing close-contact residues. (C) Grafting of the ESIPT scaffold onto TTR binding molecules.

TTR was chosen as a model system for the following reasons:

(1) WT TTR $\square$  displays excellent affinity for derivatives of benzoxazole (**1**) which are common scaffolds in ESIPT fluorophores.<sup>26, 27</sup> An example of this is the drug, Tafamidis (**2**, Vyndamax<sup>™</sup>, Pfizer Inc.),<sup>25</sup> which binds at the binding pocket formed by the dimer–dimer interface between WT TTR $\square$  homotetramers (Figure 2.1B). Theoretically, **2** can function as an ESIPT fluorophore when an –OH group is installed at the 2' position to give **3** (Figure 2.1C). In methanol, **3** displays an enol emission at 450 nm (Figure 2.2, blue trace). Alternatively, a red-shifted keto emission at 520 nm appears in the nonpolar solvent dichloromethane (Figure 2.2, green trace). This red-shift in emission in nonpolar solvents is characteristic of the ESIPT process. In fact, the dual emission of **3** in 1,4-Dioxane (Figure 2.2, red trace) confirms that ESIPT fluorescence is attained. It is interesting to point out that the enol emission in 1,4-dioxane (em. ~ 420 nm) is blue-shifted significantly from the enol emission in methanol (em. ~ 450 nm) which is indicative of a competing internal charge transfer (ICT) photochemical pathway. A small, positive solvatochromatic effect can be observed in the enol emission wavelength between methanol and phosphate buffer—likely due to differences in the protic state of the carboxylic acid in **3** between these two solvents (Figure 2.2, purple trace).

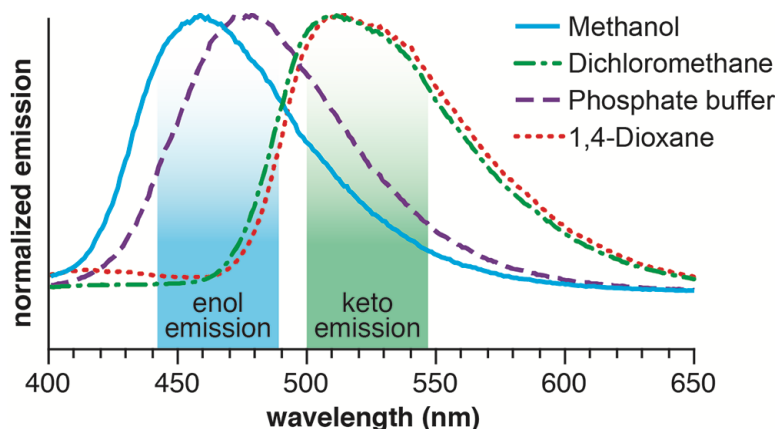


Figure 2.2 Emission traces of **3** in varying solvents. E\* emission occurs 410–450 nm whereas K\* emission is seen at 510 nm. Phosphate buffer consists 10 mM sodium phosphate (pH 7.6), 100 mM KCl, and 1 mM EDTA.

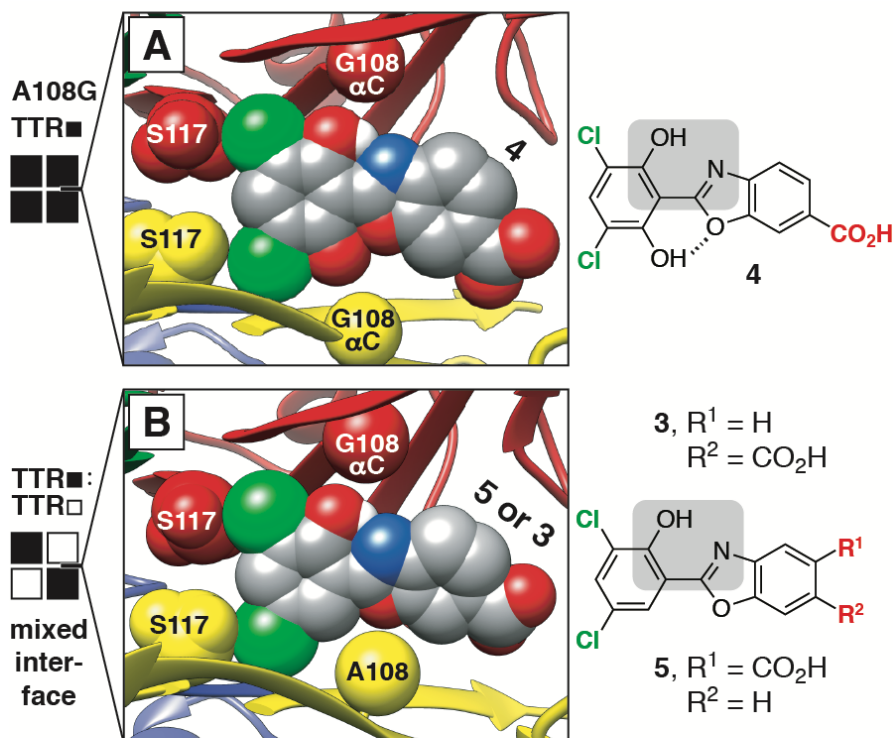


Figure 2.3 Proposed binding models of TTR mutants to ES IPT fluorophores. (A) An A108G TTR■ homotetramer displays an interface that can accommodate the phenolic moiety necessary for ES IPT. (B) A mixed WT-A108G heterotetramer interface (TTR□/ TTR■) designed to bind **3** and **5**. Images were prepared using the structure editing tools available in UCSF Chimera<sup>28</sup> on the original protein structure (PDB: 3TCT).



(2) Analysis of the binding interaction of **2** and WT TTR in Figure 2.1B, reveals that the -OH group at the 2'-position in **3** would clash with the A108 residue. This steric clash would prevent binding, but also indicates the necessary mutation that needs to be made to WT TTR in order to allow binding of an ESIPT fluorophore based on **3**. Therefore, we hypothesized that an A108G mutation would remove the steric imposition of the A108 side chain to create room for the -OH group in **3**.

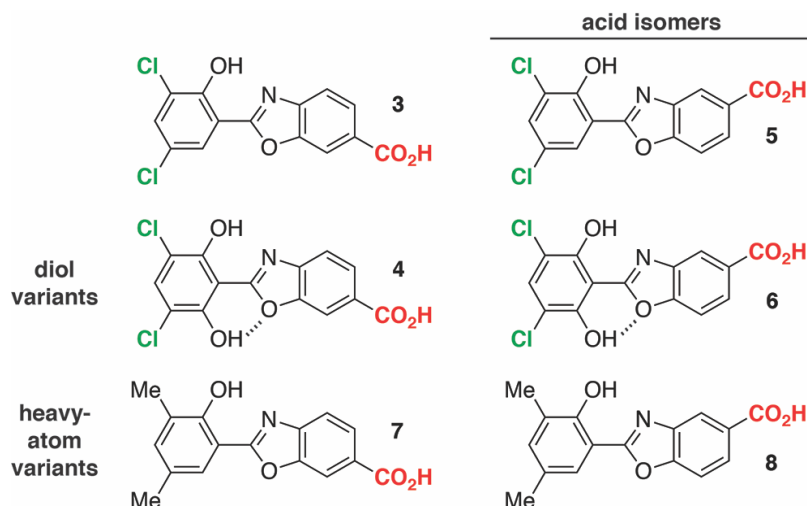
(3) Because of the symmetry of the TTR homotetramer interface, however, an A108G mutation will alter both the 'top' and 'bottom' interfaces of the binding pocket (Figure 2.3A). Thus, we designed the more symmetric **4** to bind both the 'top' and 'bottom' A108G TTR interfaces. We therefore predicted that, in free solution, **4** would be restricted to enol fluorescence. Upon specific binding to the hydrophobic binding pocket of the A108G mutant TTR, however, keto emission would be enabled.

Compound **4** also presented another advantage compared to **3**. The two OH groups in **4** have been shown to decrease rotational disorder across the biaryl due to hydrogen bonding from the OH to both the N and O of the benzoxazole.<sup>29</sup> The result was an overall increase emission intensity, Stokes' shift, and sensitivity.

## Results and Discussion

We tested our design hypothesis described above against WT TTR and A108G TTR homotetramers and evaluated the slate of benzoxazole derivatives (**3–8**) listed in Scheme 2.1. The design rationale for **3** and **4** has already been discussed above. Compounds **7** and **8** were designed to improve the emission intensity through substitution of the Cl groups with isosteric<sup>30</sup> Me groups—because halogen atoms can increase the efficiency of non-radiative processes (i.e.

intersystem crossing, “heavy-atom effect”<sup>31</sup>). Finally, **5**, **6** and **8** are isomeric in the position of the carboxylic acid.



Scheme 2.1 Benzoxazole candidates tested to selectively bind TTR to enhance ESIPT fluorescence.

Compounds **3–8** were tested at 10.0, 5.0, 2.5  $\mu\text{M}$  concentrations against 5.0  $\mu\text{M}$  solutions of WT TTR□ and A108G mutant TTR■. According to our design hypothesis, we predicted **4** would bind A108G TTR■ to enable keto emission. Unfortunately, this was not the case, as **4** displayed little change in emission characteristics in the presence of the TTR proteins (Figure 2.8). Gratifyingly, however, **5** showed selectivity for the A108G TTR■ mutant interface (Figure 2.4A) in preference to WT TTR□. Both in buffer and in the presence of WT TTR□, **5** displayed the expected signal for enol emission at 450 nm indicating that it was excluded into bulk solution. In the presence of A108G, however, **5** exhibits pronounced keto emission at 520 nm and the original 450 nm band diminishes. These data indicate that the turn-on of keto emission is likely not due to nonspecific binding to TTR, but instead indicates specific binding in the designed A108G pocket wherein the protein increases the efficiency of emission via the keto versus the enol channel.

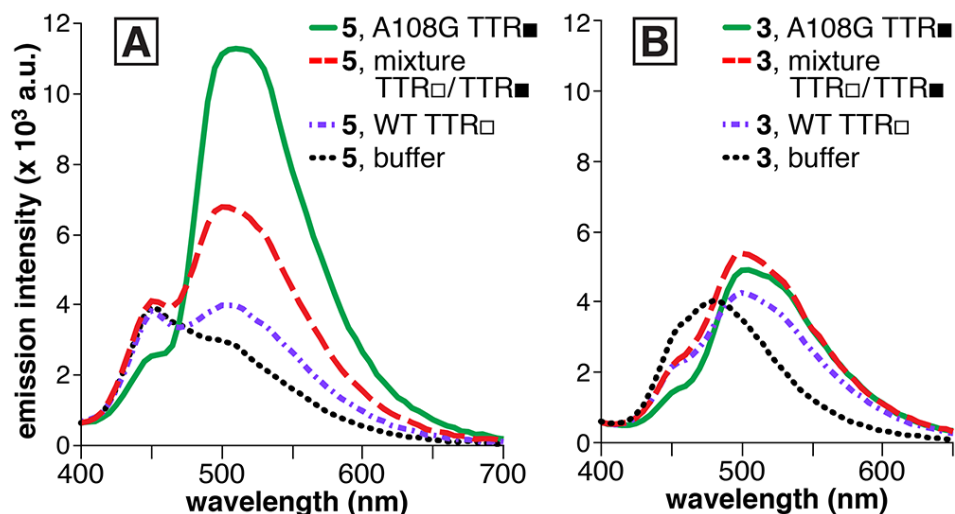


Figure 2.4 Emission traces of (A) **5** and (B) **3** at 2.5  $\mu\text{M}$  in buffer with 5.0  $\mu\text{M}$  TTR (total protein concentration). Buffer = 10 nM sodium phosphate (pH 7.6), 100 nM KCl, 1 mM EDTA.

Unfortunately, all other derivatives (**3**, **4**, **6–8**, Scheme 2.1) did not exhibit a change in emission between buffer, WT TTR $\square$  and A108G TTR $\blacksquare$  tetramers (Figure 2.7-1.10, in fact **4**, **6–8** did not exhibit emission in free solution). It is important to recognize, however, that a lack of a change in the emission signal does not inform on the ability of a given molecule to bind the TTR binding pocket. It is possible that an ES IPT fluorophore, may bind the TTR pocket with high affinity, but the protein is unable to increase the efficiency of keto emission (see below).

The failure of **4** and **6** was surprising given their symmetrical design was anticipated to bind the symmetrical pocket of A108G TTR $\blacksquare$ . The behavior of **5** and **3** was equally surprising: (i) with **5** displaying selective binding of the symmetric binding pocket of A108G TTR $\blacksquare$ , (ii) while **3** displayed no binding preference for TTR (Figure 2.4B). Inspired by the unsymmetrical nature of **5** and **3**, however, we were curious if these compounds might display greater affinity for an unsymmetrical binding pocket (Figure 2.3B)—where a higher affinity was anticipated to lead to an even greater turn-on in keto emission.

To create an asymmetric binding pocket within TTR, we capitalized on the well-characterized dissociative equilibrium of TTR between its tetrameric and monomeric forms. Mixed TTR tetramers can be generated by mixing an equimolar concentration of WT TTR□ homotetramers and A108G TTR■ homotetramers to give a statistical distribution of mixed interfaces (1 : 2 : 1 TTR□/TTR□ : TTR□/TTR■ : TTR■/TTR■).<sup>32</sup> Thus, an asymmetric interface designed to bind **5** or **3** could be realized (**Error! Reference source not found.B**). In a similar manner as for **4** described above (Fig. 5B), **5** and **3** were anticipated to produce enol emission in bulk solution but elicit keto emission upon specific binding to the asymmetric TTR□/TTR■ interface. Following this logic, asymmetric TTR□/TTR■ interfaces were generated by allowing a 5.0 μM solution of WT TTR□ and A108G TTR■ to equilibrate at 25 °C for seven days. Probes **5** and **3** were then administered (Figure 2.4).

Intriguingly, the keto emission for **5** diminished in the TTR□/TTR■ mixture (Figure 2.4A). This observation is consistent with a lower affinity for the TTR□/TTR■ mixed interface relative to the A108G TTR■ homo-tetramer. Of course, the TTR□/TTR■ mixture still contains a statistical population (25%) of TTR■/TTR■ homo-interfaces within the mixed tetramers. Thus, binding of **5** to this smaller fraction of A108G TTR■ homo-interfaces likely contributes to the observed keto emission signal.

Alternatively, **3** did not display any notable selectivity or change in enol versus keto emission intensity across any of the TTR tetramers (Figure 2.4B). This result is unexpected given the structural similarities of **3** and **5** (differing only in the position of the carboxylic acid). For example, Tafamidis (**1**) can bind the WT TTR□ binding pocket with C<sub>2</sub> symmetry (i.e. The CO<sub>2</sub>H group can orient towards either the 'top' or 'bottom' interface, PDB 3TCT). Thus, it is

surprising that the subtle regioisomerism of the CO<sub>2</sub>H between **3** and **5** can lead to significant differences across the TTR tetramers in Figure 2.4.

The contrasting behavior of **3** and **5** is even more surprising because titration curves measuring absorbance vs. concentration of **3** and **5** in the presence of TTR have similar forms. While it was not possible to derive binding constants with confidence using this method (since absorbance is not very sensitive at concentrations low enough to obtain accurate K<sub>d</sub> measurements, given that the K<sub>d</sub>s are expected to be in the low-to-mid nanomolar range), this information does indicate that **3** and **5** have commensurate binding affinities with A108G TTR<sup>■</sup>. Thus, if both **3** and **5** bind with similar affinity but display different emissive behavior, it suggests that specific interactions between the protein and the fluorophore are essential to realize strong ratiometric differences between the two possible wavelengths of emission. Removal of the alanine side chain to create the A108G binding pocket (**Error! Reference source not found.**) likely creates a 'looser' fit for **3** and **5**. Thus, it is reasonable to conclude that the contrasting behavior of **3** and **5** stems from differences in the bond lengths and geometry of the oxazole that pose the CO<sub>2</sub>H group differently for each molecule in the binding pocket. Finally, the position of the electron-withdrawing CO<sub>2</sub>H may alter the efficiency of emissive pathways once bound.

In an effort to design ESIPT capable probes that better target the TTR<sup>□</sup>/TTR<sup>■</sup> mixed interface, we examined another TTR binding benzoxazole, **9**. The binding mode of **9** can be seen in Figure 2.5A.<sup>26</sup> Relative to Tafamidis, **9**'s binding orientation is reversed in the T<sub>4</sub> binding pocket of TTR. The benzoxazole group now binds to the interior of the pocket leaving the 2-phenyl group oriented towards the outside. Two structural aspects of **9** are critical for this alternative orientation. First, the reduced pK<sub>a</sub> of the 4'-hydroxyl group allows it to form charged interactions with the K15 residues (the same lysine residues that formed a salt bridge with the

carboxylate in **1**).<sup>27</sup> Secondly, the chlorine in the 4 position docks inside of a hydrophobic pocket that is formed by the A108, L110, S117, and T119 residues (Figure 2.5C). We rationalized that the built in asymmetry of **9** would enable for the selective binding of our asymmetric mixed TTR interfaces (Figure 2.5B).

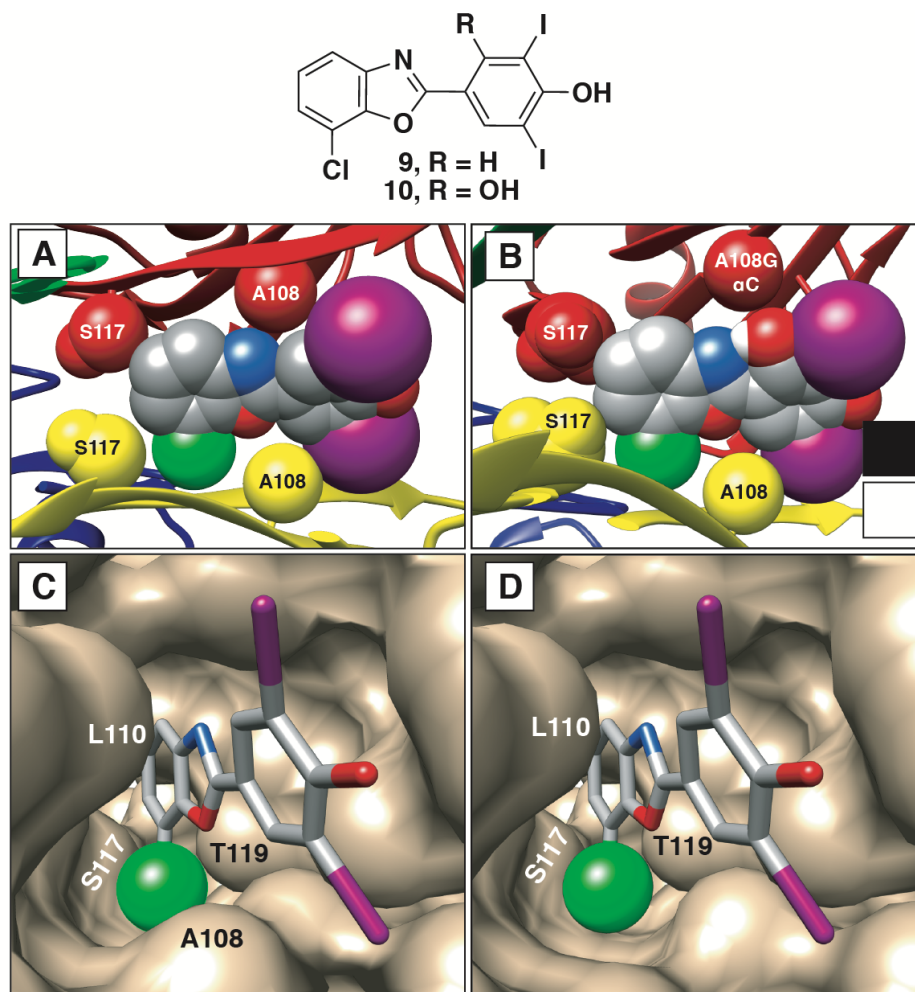


Figure 2.5 (A) **9** bound to TTR (PDB: 5TZL)<sup>26</sup> in a reversed orientation from that of Tafamidis (see Figure 1.1). (B) Proposed binding of **10** to the TTR□/ TTR■ mixed interface where TTR■ is on top. (C & D) The hydrophobic binding pocket with and without the A108G mutation.

The mixed interface is ideally set up to accompany **10** as its lone binding partner.

Because A108 appears important for the binding of **9**, the WT TTR□ side of the interface would provide the hydrophobic pocket needed to accompany the 4-substituent. Additionally, the

A108G TTR $\blacksquare$  interface that makes up the other side of the dimer would allow the 2'-hydroxy functional group to fit and undergo ESIPT inside of the binding pocket as we witnessed earlier with **5**. This is in contrast to **10** binding TTR $\square$ /TTR $\square$  homodimer where the space necessary for the 2'-hydroxy group would be occupied by A108 on either monomer and therefore restricting binding. Furthermore, we postulate that **10** binding to TTR $\blacksquare$ /TTR $\blacksquare$  homodimers will have a lower binding affinity due to the lack of an enclosed hydrophobic pocket (Figure 2.5D).

To this end, **11** and **12** were synthesized and their photochemical properties were measured in each of the three TTR dimer interfaces. Probe **11** was designed without the 4 substituent on the benzoxazole to evaluate its importance in targeting mixed TTR $\square$ /TTR $\blacksquare$  interfaces in relation to probe **12**. Figure 2.6 shows the results of **11** and **12** in the same fluorescence assay as before. Unfortunately, the desired effect of *turn-on* ESIPT upon binding to mixed interfaces was not seen. In fact, no *turn-on* ESIPT fluorescence was observed when mixed with protein solution regardless of the dimer interface makeup (Figure 2.6). This would suggest that **11** and **12** do not bind as expected to TTR *and* undergo ESIPT fluorescence as a result of the change in microenvironment. Binding constants were not attempted to be measured so it is possible that these probes are binding but are unable to undergo ESIPT or are nonemissive in general. The dimethyl moiety on **11** and **12** might have actually inhibited binding. The iodines in **9** were proposed to influence the binding orientation of **9** by decreasing the *pKa* of the 4' phenol and binding in a halogen binding pocket, both of which are likely limited with isomeric methyl substitutions. The use of halogens, such as Cl, which was shown to be effective in the first generation of probes, could be used instead to capitalize on this binding mode.

Despite the lack of ESIPT signal upon protein binding, **11** and **12** in buffer display ESIPT fluorescence albeit to a varying extent. While this behavior is difficult to explain, it is possible

that at a 10x more concentrated solution of probe, aggregation induced emission (AIE) could occur. An interesting observation is that emission of **12** results in a much lower keto emission band than **11** despite the added methyl is considered only a weakly electron donating group. Ultimately this showcases the unknown effects that substituents have on ESIPT properties of these 2-(2'-hydroxyphenyl)-benzoxazole chromophores.

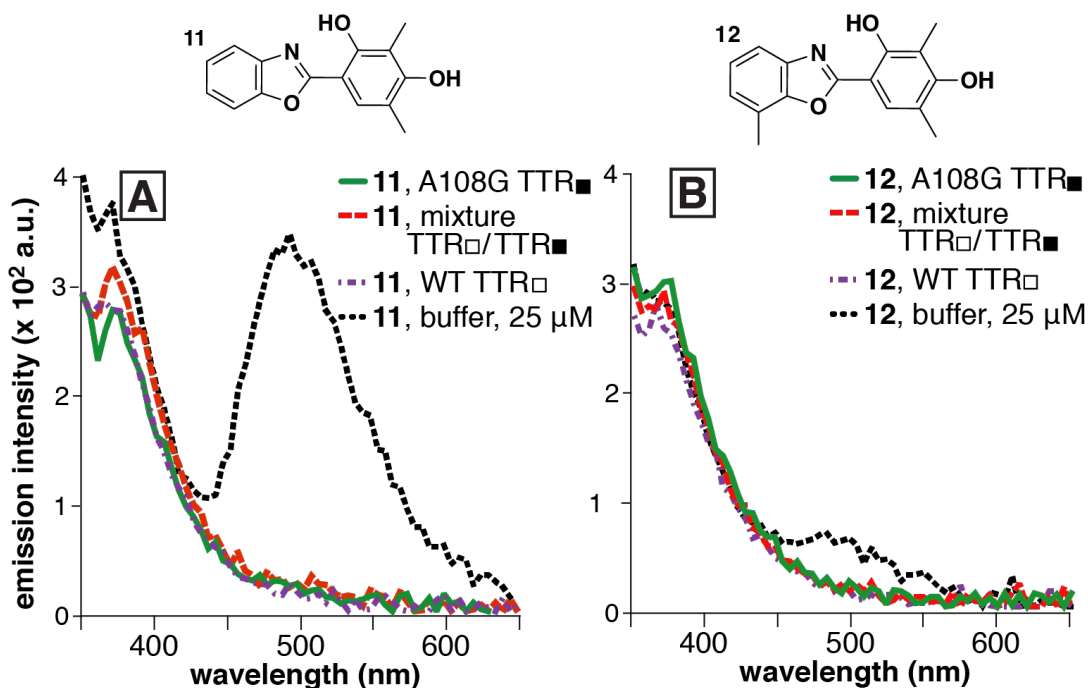


Figure 2.6 Emission traces of (A) **11** and (B) **12** at 2.5  $\mu\text{M}$  in buffer with 5.0  $\mu\text{M}$  TTR (total protein concentration) with the exception of the trace in buffer, which was at a concentration of 25  $\mu\text{M}$ . Buffer = 10 nM sodium phosphate (pH 7.6), 100 nM KCl, 1 mM EDTA.

### Conclusion

This work describes the first demonstration of a rationally designed protein receptor that selectively binds and alters the photochemical pathways of ESIPT fluorophores. More broadly, this work demonstrates that specific interactions between the protein and the fluorophore are

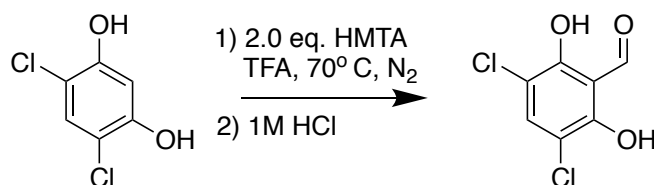


essential to realize strong ratiometric differences between the two possible wavelengths of emission in ESIPT fluorophores.

The ESIPT process has the potential to allow for two wavelengths to be read out from a single molecule in a ratiometric fashion, but previous systems have primarily observed only subtle changes in the wavelength ratio due to nonspecific binding. The system we describe here exploits the environmental dependence of the ESIPT process where bulk water disrupts the efficiency of proton transfer in the excited state. The protein receptor was designed to selectively bind and desolvate an ESIPT fluorophore within a hydrophobic pocket. The result is a dramatic difference and inversion of the proportion of enol and keto emission. Finally, we note that benzoxazoles and benzothiazoles are privileged scaffolds in medicinal chemistry<sup>33</sup> as they are found in numerous therapeutics displaying anticancer, antimicrobial, antiviral and anti-inflammatory properties, among others.<sup>34-36</sup> Thus, we envision benzoxazoles may be utilized in diagnostic assays based on ESIPT fluorescence.<sup>37</sup> We therefore anticipate this report to lay the groundwork towards the development of future ESIPT fluorescence based bioimaging technologies and monitoring of protein-protein interactions.

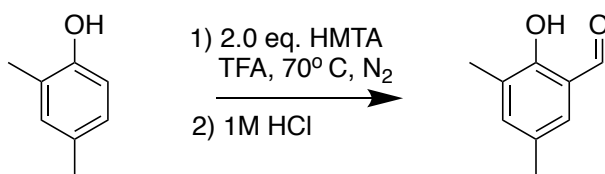
## Experimental

### Synthetic Procedures

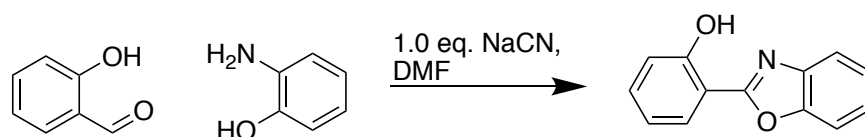


**Synthesis of 3,5-dichloro-2,6-dihydroxybenzaldehyde:** 4,6-Dichlororesorcinol (1.71 g, 9.57 mmol) was added to a solution of hexamethylenetetramine (2.67 g, 19.1 mmol) in neat

trifluoroacetic acid (50.0 mL) under N<sub>2</sub> and heated to 70° C for 12 h. Upon disappearance of starting material, by TLC, 1M HCl (50.0 mL) was added and stirred at 70° C for an additional 5 hours. The reaction was allowed to cool to room temperature and the precipitate was filtered and dried to yield 3,5-dichloro-1,6-dihydroxy benzaldehyde (1.31 g, 65% yield) as a yellow solid. The product was used without further purification. Physical and spectroscopic data were in agreement with literature reports.<sup>38</sup>



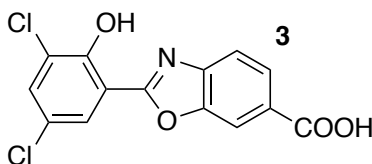
**Synthesis of 3,5-dimethyl-2-hydroxybenzaldehyde:** 2,4-Dimethylphenol (1.00 mL, 8.28 mmol) was added to a solution of hexamethylenetetramine (2.32 g, 16.52 mmol) in neat trifluoroacetic acid (50.0 mL) under N<sub>2</sub> and heated to 70° C for 12 h. Upon disappearance of starting material, by TLC, 1M HCl (50.0 mL) was added and the reaction stirred for an additional 3 hours at 100° C. Upon completion, the reaction was cooled to room temperature and was extracted with dichloromethane (3x20 mL). The resulting organic fractions were combined, washed with brine, dried over sodium sulfate, and concentrated *in vacuo*. The crude oil was purified via silica gel chromatography (1:9 Ethyl Acetate/Hexanes) to yield 3,5-salicylaldehyde (607 mg, 49%yield) as a yellow liquid. Physical and spectroscopic data were in agreement with literature reports.<sup>39</sup>



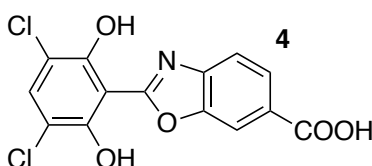
**General procedure for the synthesis of 2-(2-hydroxyphenyl)benzoxazole derivatives:**

To a solution of Salicylaldehyde derivative (1.0 eq.) in DMF (0.1 M) was added 2-Amino Phenol

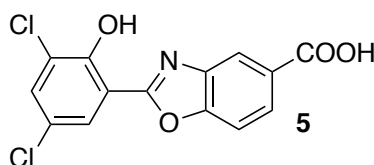
derivative (1.0 eq.) and was stirred at room temperature. Upon disappearance of starting material, sodium cyanide (1.0 eq.) was added and the reaction was stirred for an additional 18 hours exposed to air. Upon reaction completion, the solution was quenched with 0.1M HCl (10x current volume) and the resulting precipitate was collected via vacuum filtration, dried and used without further purification.



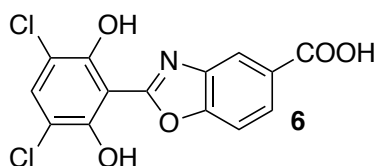
**(3):** 1.55 mmol scale to yield 2-(3,5-dichloro-2-hydroxyphenyl)benzoxazole-6-carboxylic acid (349 mg, 70% yield).  $^1\text{H}$  NMR (400 MHz,  $\text{d}_6\text{-DMSO}$ )  $\delta$  13.3 (s, 1H), 11.78 (s, 1H), 8.32 (dd,  $J=0.36, 1.32$  Hz, 1H), 8.09 (dd,  $J=1.48, 8.4$  Hz, 1H), 8.00 (d,  $J=2.52$  Hz, 1H), 7.98 (dd,  $J=0.36, 8.32$  Hz, 1H), 7.91 (d,  $J=2.56$  Hz, 1H).  $^{13}\text{C}$  (125 MHz,  $\text{d}_6\text{-DMSO}$ )  $\delta$  166.55, 162.76, 152.59, 148.75, 142.58, 133.44, 128.99, 126.91, 125.75, 123.70, 122.59, 119.39, 112.66, 112.26. HRMS: Calc'd 321.9679, Found 321.9682.



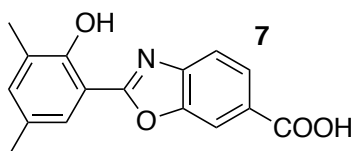
**(4):** 1.47 mmol scale. The collected precipate was further purified via silica gel chromatography (1:19 Methanol/Dichloromethane) to yield 2-(3,5-dichloro-2,6-dihydroxyphenyl)benzoxazole-6-carboxylic acid as a dark orange solid (135 mg, 27% yield).  $^1\text{H}$  NMR (600 MHz,  $\text{d}_6\text{-DMSO}$ )  $\delta$  11.37 (s, 2H), 8.31 (d,  $J=1.38$  Hz, 1H), 8.09 (dd  $J=1.50, 8.34$  Hz, 1H), 7.97 (d,  $J=8.34$  Hz, 1H), 7.78 (s, 1H).  $^{13}\text{C}$  (125 MHz,  $\text{d}_6\text{-DMSO}$ )  $\delta$  167.17, 163.13, 153.07, 149.40, 142.65, 122.40, 128.93, 127.03, 119.53, 112.59, 112.55, 104.62. HRMS: Calc'd 337.9629, Found 337.9635.



**(5):** 1.55 mmol scale to yield 2-(3,5-dichloro-2-hydroxyphenyl)benzoxazole-5-carboxylic acid as a pale yellow solid (250 mg, 50% yield).  $^1\text{H}$  NMR (600 MHz,  $\text{d}_6\text{-DMSO}$ )  $\delta$  11.70 (s, 1H), 8.34 (s, 1H), 8.09 (d,  $J=7.86$  Hz, 1H), 7.91 (m, 2H), 7.82 (d,  $J=2.28$  Hz, 1H).  $^{13}\text{C}$  (125 MHz,  $\text{d}_6\text{-DMSO}$ )  $\delta$  167.02, 162.12, 152.88, 151.97, 139.55, 133.64, 129.04, 128.38, 125.90, 125.10, 122.95, 121.19, 12.88, 111.77. HRMS: Calc'd 321.9679, Found 321.9686.

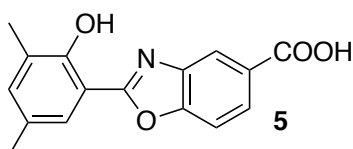


**(6):** 1.47 mmol scale to yield 2-(3,5-dichloro-2,6-dihydroxyphenyl)benzoxazole-5-carboxylic acid as a light orange solid (361 mg, 72% yield).  $^1\text{H}$  NMR (600 MHz,  $\text{d}_6\text{-DMSO}$ )  $\delta$  11.32 (s, 2H), 8.38 (s, 1H), 8.10 (dd,  $J=0.72, 8.52$  Hz, 1H), 7.94 (d,  $J=8.52$  Hz, 1H), 7.74 (s, 1H).  $^{13}\text{C}$  (125 MHz,  $\text{d}_6\text{-DMSO}$ )  $\delta$  167.23, 162.06, 152.98, 152.34, 139.19, 122.20, 128.65, 127.82, 120.98, 112.52, 111.66, 104.54. HRMS: Calc'd 337.9629, Found 337.9630.

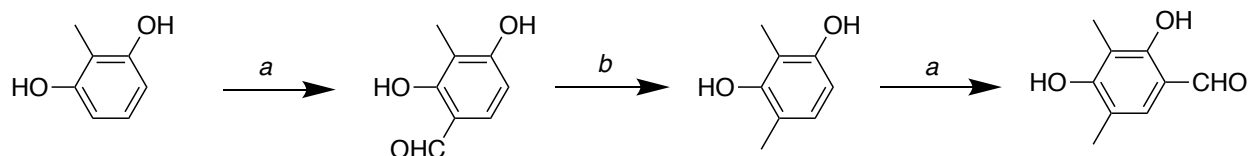


**(7):** 1.05 mmol scale to yield 2-(3,5-dimethyl-2-hydroxyphenyl)benzoxazole-6-carboxylic acid as a pale orange solid (213 mg, 71% yield)  $^1\text{H}$  NMR (400 MHz,  $\text{d}_6\text{-DMSO}$ )  $\delta$  11.09 (s, 1H), 8.20 (dd,  $J=0.48, 1.44$  Hz, 1H), 8.00 (dd,  $J=1.48, 8.32$  Hz, 1H), 7.83 (dd,  $J=0.44, 8.28$  Hz, 1H), 7.56 (d,  $J=2.04$  Hz, 1H), 7.16 (d,  $J=2.08$  Hz, 1H), 2.25 (s, 3H), 2.19 (s, 3H).  $^{13}\text{C}$  (125 MHz,  $\text{d}_6\text{-DMSO}$ )  $\delta$  166.65, 164.89, 154.41, 148.32, 142.90, 136.34, 128.27, 128.22,

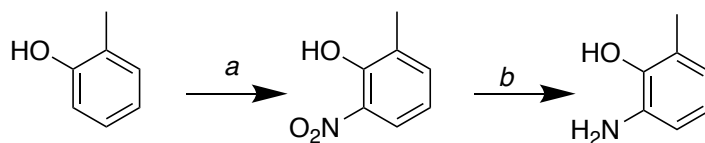
126.62, 125.67, 124.43, 118.63, 111.83, 108.41, 19.91, 15.53. HRMS: Calc'd 284.0917, Found 284.0909.



**(8):** 0.88 mmol scale to yield 2-(3,5-dimethyl-2-hydroxyphenyl)benzoxazole-5-carboxylic acid as a yellow solid (107 mg, 43% yield)  $^1\text{H}$  NMR (400 MHz,  $\text{d}_6\text{-DMSO}$ )  $\delta$  13.12 (s, 1H), 11.01 (s, 1H), 8.22 (d,  $J=1.24$  Hz, 1H), 8.00 (dd,  $J=1.64, 8.56$  Hz, 1H), 7.81 (d,  $J=8.56$ , 1H), 7.50 (s, 1H), 7.12 (s, 1H), 2.23 (s, 3H), 2.17 (s, 3H).  $^{13}\text{C}$  (125 MHz,  $\text{d}_6\text{-DMSO}$ )  $\delta$  166.69, 163.85, 154.21, 151.25, 139.44, 136.04, 128.16, 128.15, 127.13, 125.58, 124.26, 120.09, 110.83, 108.37, 19.91, 15.51. HRMS: Calc'd 284.0917, Found 284.0917.



Scheme 2.2 Synthetic route towards starting aldehyde for the synthesis of **11** and **12**. (a) 1.1 eq  $\text{POCl}_3$ , 1.3 eq. DMF, in Acetonitrile. (b) (1) Zn, THF, (2) Conc. HCl.



Scheme 2.3 Synthetic route towards starting 2-amino phenol for the synthesis of **12**. (a)  $\text{AcOH}/\text{HNO}_3$ ,  $-15^\circ\text{C}$  (b)  $\text{SnCl}_2$ , EtOH,  $\text{N}_2$ , Conc. HCl.

### Expression and Purification of Wild-Type TTR and A108G-TTR

Wild-type TTR and A108G-TTR were prepared as previously described.<sup>40, 41</sup> Briefly, both plasmids (pMMHa) were transformed into competent BL21 cells. Two 1L-flasks of LB medium with ampicillin (100  $\mu$ g/mL) were inoculated with fresh 40 mL overnight cultures. Cells were grown at 37°C with vigorous shaking until reaching an OD<sub>600nm</sub> of 0.6. At this point, the cells were induced with 1 mM IPTG and left at the same conditions. Six hours post-induction, cells were harvested and resuspended in 10 mM sodium phosphate buffer (pH 7.6), and lysed by one cycle of freeze (-80°C)-thaw, followed by 5 cycles of 3 minutes sonication/3 minutes rest at 4°C. Cell debris was removed by centrifugation. Both variants were purified first using ammonium sulfate precipitation. The supernatant was treated with 40% ammonium sulfate, equilibrated for 30 minutes and again collected following centrifugation. The semi-purified 40% supernatants were then precipitated with a 90% ammonium sulfate treatment. The proteins were then dialyzed overnight into 25 mM Tris pH 8.0, 1 mM EDTA with 3000 MW dialysis tubing (Snakeskin from Pierce Biomedical). Both variants were purified on a Source15Q anion exchange column (Amersham Biosciences) eluting with a 200-350 mM NaCl gradient at room temperature, followed by further purification using a gel filtration column (Superdex 75). Proteins were eluted using 10 mM sodium phosphate (pH 7.6), 100 nM KCl, 1 mM EDTA. Both proteins' purity and mass were confirmed by LC-MS analysis (wild-type TTR: 13892; A108G-TTR: 13878). – Done by Dr. Cecilia Monteiro

### Fluorescence binding assay

Stock solutions of **3-8** were prepared by diluting solutions of **3-8** in DMSO 10-, 20-, and 40-fold in buffer. Each well of a 96-well plate contained 90  $\mu$ L of 5.55  $\mu$ M protein solution that was diluted to 100  $\mu$ L (5.0  $\mu$ M) with the stock solution of each probe. Each sample was excited at

335 nm at 9.0 mm slit width and the fluorescence was measured from 360-650 nm at 5 nm intervals. Emission traces were cut off at 400 nm for clarity as emission from Tryptophan and light scattering from the sample plate are apparent at 350 nm. All experiments were done in triplicate.

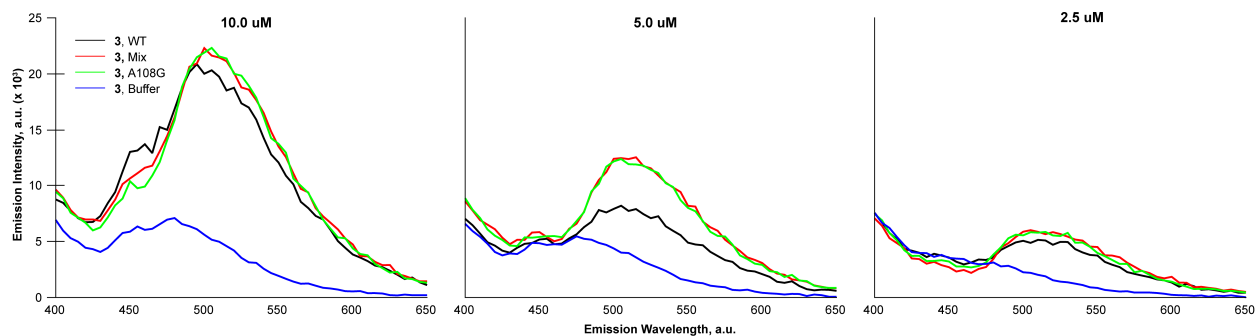


Figure 2.7 Emission profiles of **3** in 5.0  $\mu\text{M}$  WT, Mix, A108G and buffer solutions.

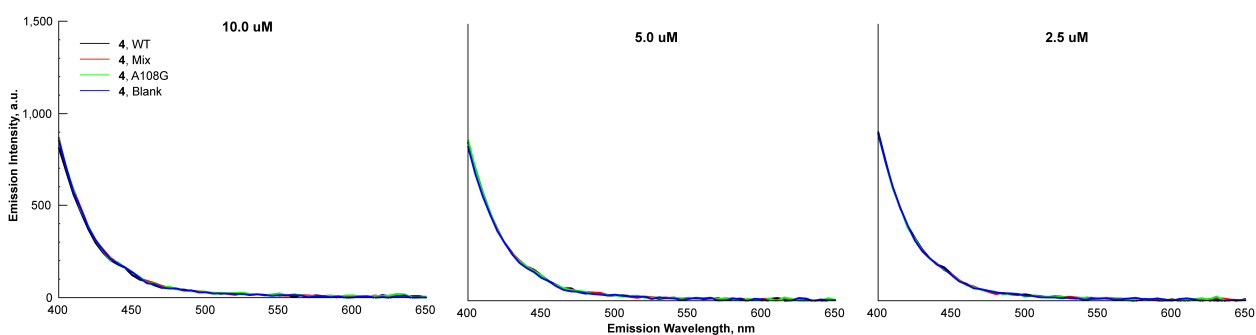


Figure 2.8 Emission profiles of **4** in 5.0  $\mu\text{M}$  WT, Mix, A108G and buffer solutions.

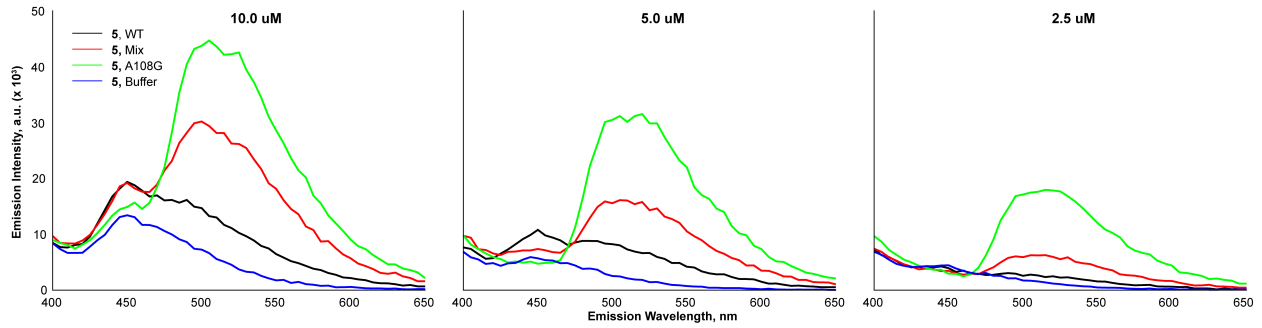


Figure 2.9 Emission profiles of **5** in 5.0  $\mu\text{M}$  WT, Mix, A108G and buffer solutions.

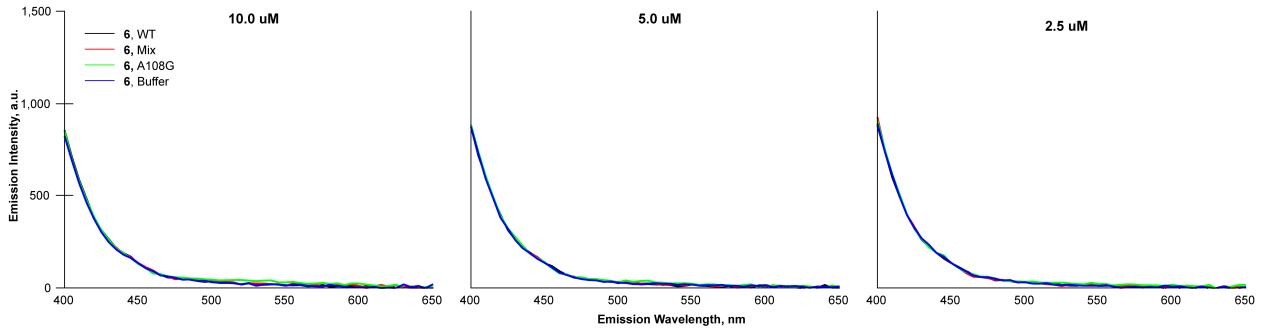


Figure 2.10 Emission profiles of **6** in 5.0  $\mu\text{M}$  WT, Mix, A108G and buffer solutions.

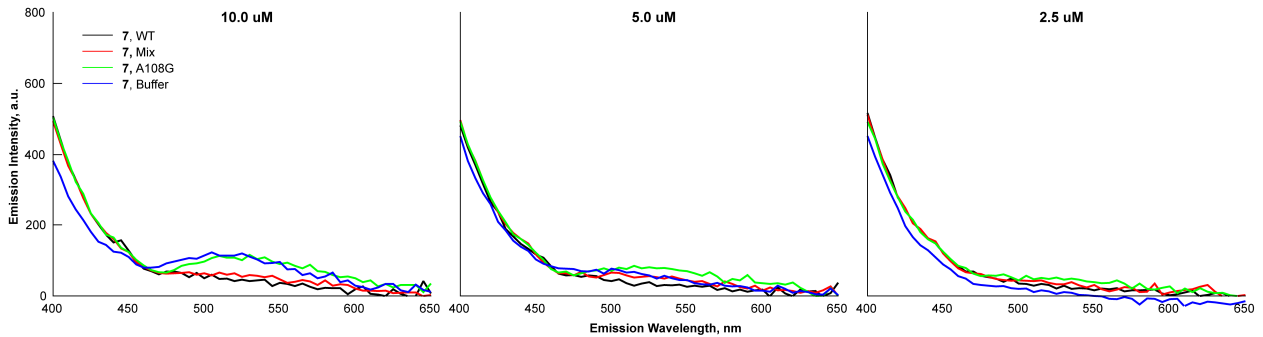


Figure 2.11 Emission profiles of **7** in 5.0  $\mu\text{M}$  WT, Mix, A108G and buffer solutions.



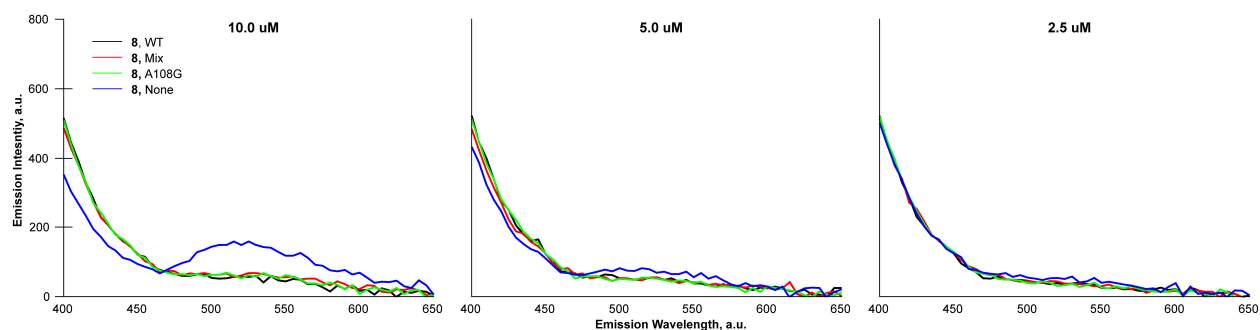


Figure 2.12 Emission profiles of **8** in 5.0  $\mu\text{M}$  WT, Mix, A108G and buffer solutions.

### Binding Studies of **3** and **5** in A108G Protein

Procedure: 1.0 mL of 5.0  $\mu\text{M}$  solution of A108G protein was titrated with sub 1.0  $\mu\text{L}$  injections of stock solutions in DMSO of either **3** or **5**, to which the total added DMSO did not exceed 2% of the total solution volume. 1:1 binding isotherms were fit using the Thordson fitting program. Despite the two binding sites of Transthyretin, Tafamidis binds with negative cooperativity and only one binding isotherm was observed in our studies. Therefore, we found a 1:1 binding isotherm valid for this model. The  $K_a$  of **3** into A108G was found to be 9793  $\text{M}^{-1}$  (Figure 2.13) and the  $K_a$  of **5** into A108G was found to be 11338  $\text{M}^{-1}$  (Figure 2.14). To verify that variations in absorptions were due to binding and not dilution, **5** was titrated into buffered solution and the change in absorption was found to be linear (Figure 2.15). Thus, we believe observed isotherms are due to binding.

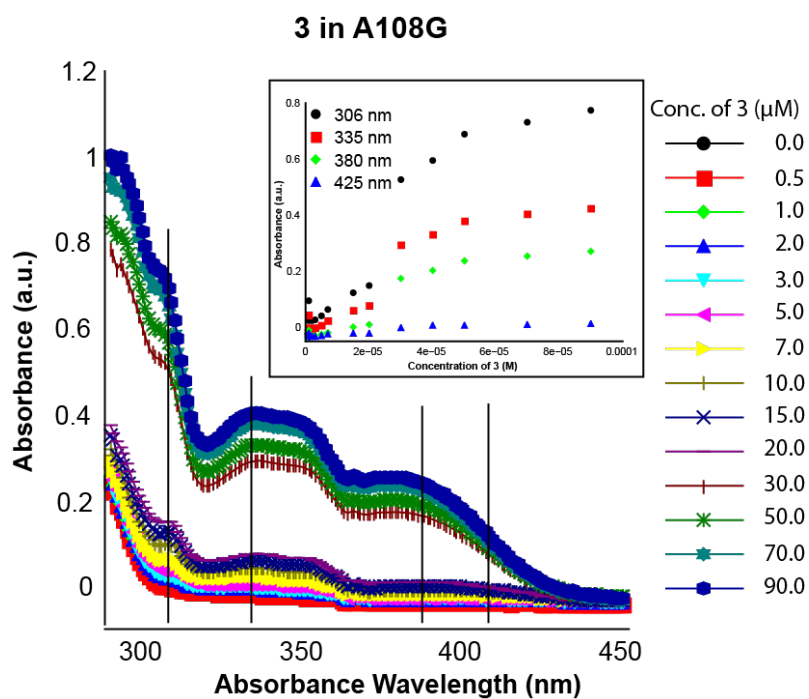


Figure 2.13 Binding of **3** into 5  $\mu\text{M}$  A108G solution. Inset: Absorbances at four wavelengths.

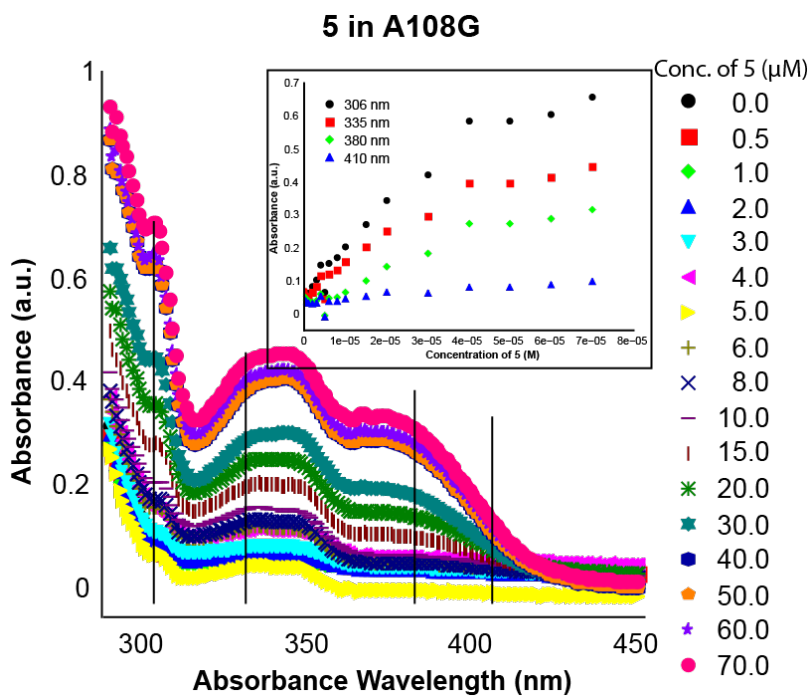


Figure 2.14 Binding of **5** into 5  $\mu\text{M}$  A108G solution. Inset: Absorbances at four wavelengths.

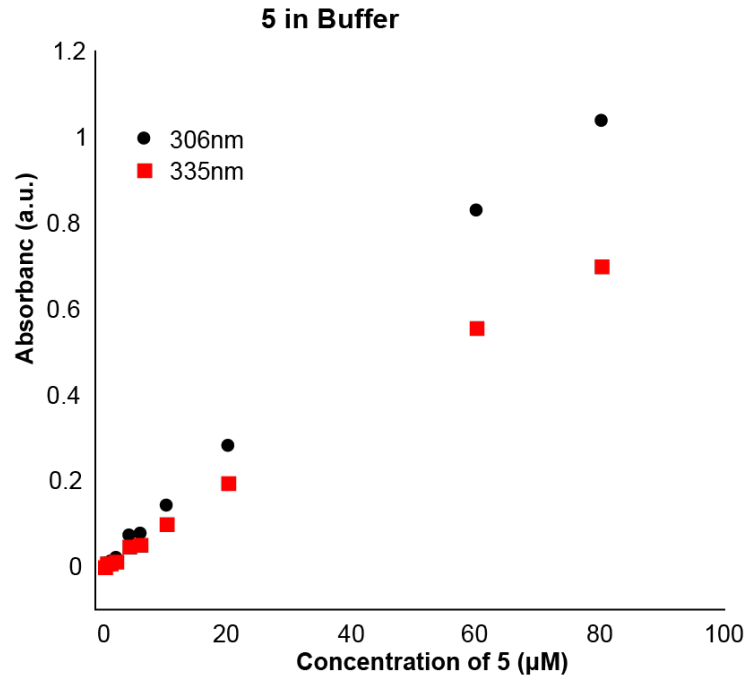


Figure 2.15 Absorbances of 5 in buffer solution at two wavelengths.

## References

1. Wald, G., Molecular basis of visual excitation. *Science* **1968**, *162* (3850), 230-9.
2. Meech, S. R., Excited state reactions in fluorescent proteins. *Chemical Society Reviews* **2009**, *38* (10), 2922-2934.
3. Ward, W. W.; Bokman, S. H., Reversible denaturation of Aequorea green-fluorescent protein: physical separation and characterization of the renatured protein. *Biochemistry* **1982**, *21* (19), 4535-40.
4. Hofmann, L.; Palczewski, K., Advances in understanding the molecular basis of the first steps in color vision. *Prog Retin Eye Res* **2015**, *49*, 46-66.
5. Zhao, J.; Ji, S.; Chen, Y.; Guo, H.; Yang, P., Excited state intramolecular proton transfer (ESIPT): from principal photophysics to the development of new chromophores and applications in fluorescent molecular probes and luminescent materials. *Physical Chemistry Chemical Physics* **2012**, *14* (25), 8803-8817.
6. Azarias, C.; Budzák, Š.; Laurent, A. D.; Ulrich, G.; Jacquemin, D., Tuning ESIPT fluorophores into dual emitters. *Chemical Science* **2016**, *7* (6), 3763-3774.
7. Klymchenko, A. S., Solvatochromic and Fluorogenic Dyes as Environment-Sensitive Probes: Design and Biological Applications. *Acc Chem Res* **2017**, *50* (2), 366-375.
8. Zhou, P.; Han, K., Unraveling the Detailed Mechanism of Excited-State Proton Transfer. *Acc Chem Res* **2018**, *51* (7), 1681-1690.
9. Singh, K.; Rotaru, A. M.; Beharry, A. A., Fluorescent Chemosensors as Future Tools for Cancer Biology. *ACS Chem Biol* **2018**, *13* (7), 1785-1798.
10. Sytnik, A.; Kasha, M., Excited-State Intramolecular Proton Transfer as a Fluorescence Probe for Protein Binding-Site Static Polarity. *Proceedings of the National Academy of Sciences of the United States of America* **1994**, *91* (18), 8627-8630.
11. Maity, S. S.; Samanta, S.; Sardar, P. S.; Pal, A.; Dasgupta, S.; Ghosh, S., Fluorescence, anisotropy and docking studies of proteins through excited state intramolecular proton transfer probe molecules. *Chemical Physics* **2008**, *354* (1), 162-173.
12. Sardar, P. S.; Samanta, S.; Maity, S. S.; Dasgupta, S.; Ghosh, S., Energy transfer photophysics from serum albumins to sequestered 3-hydroxy-2-naphthoic acid, an excited state intramolecular proton-transfer probe. *J Phys Chem B* **2008**, *112* (11), 3451-61.
13. Ray, D.; Paul, B. K.; Guchhait, N., Effect of biological confinement on the photophysics and dynamics of a proton-transfer phototautomer: an exploration of excitation and emission wavelength-dependent photophysics of the protein-bound drug. *Physical Chemistry Chemical Physics* **2012**, *14* (35), 12182-12192.

14. Paul, B. K.; Guchhait, N., Photophysics of a proton transfer phototautomer within biological confinement of a protein: Spectroscopic and molecular docking studies. *Journal of Luminescence* **2014**, *153*, 430-438.
15. Popova, M.; Soboleva, T.; Ayad, S.; Benninghoff, A. D.; Berreau, L. M., Visible-Light-Activated Quinolone Carbon-Monoxide-Releasing Molecule: Prodrug and Albumin-Assisted Delivery Enables Anticancer and Potent Anti-Inflammatory Effects. *J Am Chem Soc* **2018**, *140* (30), 9721-9729.
16. Strizhak, A. V.; Postupalenko, V. Y.; Shvadchak, V. V.; Morellet, N.; Guittet, E.; Pivovarenko, V. G.; Klymchenko, A. S.; Mély, Y., Two-color fluorescent l-amino acid mimic of tryptophan for probing peptide-nucleic acid complexes. *Bioconjug Chem* **2012**, *23* (12), 2434-43.
17. Sholokh, M.; Zamotaiev, O. M.; Das, R.; Postupalenko, V. Y.; Richert, L.; Dujardin, D.; Zaporozhets, O. A.; Pivovarenko, V. G.; Klymchenko, A. S.; Mély, Y., Fluorescent amino acid undergoing excited state intramolecular proton transfer for site-specific probing and imaging of peptide interactions. *J Phys Chem B* **2015**, *119* (6), 2585-95.
18. Enander, K.; Choulier, L.; Olsson, A. L.; Yushchenko, D. A.; Kanmert, D.; Klymchenko, A. S.; Demchenko, A. P.; Mély, Y.; Altschuh, D., A peptide-based, ratiometric biosensor construct for direct fluorescence detection of a protein analyte. *Bioconjug Chem* **2008**, *19* (9), 1864-70.
19. Jiang, N.; Yang, C.; Dong, X.; Sun, X.; Zhang, D.; Liu, C., An ESIPT fluorescent probe sensitive to protein  $\alpha$ -helix structures. *Organic & Biomolecular Chemistry* **2014**, *12* (28), 5250-5259.
20. Shvadchak, V. V.; Falomir-Lockhart, L. J.; Yushchenko, D. A.; Jovin, T. M., Specificity and kinetics of alpha-synuclein binding to model membranes determined with fluorescent excited state intramolecular proton transfer (ESIPT) probe. *J Biol Chem* **2011**, *286* (15), 13023-32.
21. Fauerbach, J. A.; Yushchenko, D. A.; Shahmoradian, S. H.; Chiu, W.; Jovin, T. M.; Jares-Erijman, E. A., Supramolecular non-amyloid intermediates in the early stages of  $\alpha$ -synuclein aggregation. *Biophys J* **2012**, *102* (5), 1127-36.
22. Lavis, L. D.; Raines, R. T., Bright building blocks for chemical biology. *ACS Chem Biol* **2014**, *9* (4), 855-66.
23. Foss, T. R.; Wiseman, R. L.; Kelly, J. W., The pathway by which the tetrameric protein transthyretin dissociates. *Biochemistry* **2005**, *44* (47), 15525-33.
24. Hurshman Babbes, A. R.; Powers, E. T.; Kelly, J. W., Quantification of the thermodynamically linked quaternary and tertiary structural stabilities of transthyretin and its disease-associated variants: the relationship between stability and amyloidosis. *Biochemistry* **2008**, *47* (26), 6969-84.

25. Bulawa, C. E.; Connelly, S.; Devit, M.; Wang, L.; Weigel, C.; Fleming, J. A.; Packman, J.; Powers, E. T.; Wiseman, R. L.; Foss, T. R.; Wilson, I. A.; Kelly, J. W.; Labaudinière, R., Tafamidis, a potent and selective transthyretin kinetic stabilizer that inhibits the amyloid cascade. *Proc Natl Acad Sci U S A* **2012**, *109* (24), 9629-34.
26. Connelly, S.; Mortenson, D. E.; Choi, S.; Wilson, I. A.; Powers, E. T.; Kelly, J. W.; Johnson, S. M., Semi-quantitative models for identifying potent and selective transthyretin amyloidogenesis inhibitors. *Bioorg Med Chem Lett* **2017**, *27* (15), 3441-3449.
27. Johnson, S. M.; Connelly, S.; Wilson, I. A.; Kelly, J. W., Biochemical and Structural Evaluation of Highly Selective 2-Arylbenzoxazole-Based Transthyretin Amyloidogenesis Inhibitors. *Journal of Medicinal Chemistry* **2008**, *51* (2), 260-270.
28. Pettersen, E. F.; Goddard, T. D.; Huang, C. C.; Couch, G. S.; Greenblatt, D. M.; Meng, E. C.; Ferrin, T. E., UCSF Chimera--a visualization system for exploratory research and analysis. *J Comput Chem* **2004**, *25* (13), 1605-12.
29. Chen, W.-H.; Pang, Y., Excited-state intramolecular proton transfer in 2-(2',6'-dihydroxyphenyl)benzoxazole: effect of dual hydrogen bonding on the optical properties. *Tetrahedron Letters* **2010**, *51* (14), 1914-1918.
30. González-Lafuente, L.; Egea, J.; León, R.; Martínez-Sanz, F. J.; Monjas, L.; Perez, C.; Merino, C.; García-De Diego, A. M.; Rodríguez-Franco, M. I.; García, A. G.; Villarroya, M.; López, M. G.; de Los Ríos, C., Benzothiazepine CGP37157 and its isosteric 2'-methyl analogue provide neuroprotection and block cell calcium entry. *ACS Chem Neurosci* **2012**, *3* (7), 519-29.
31. Kamkaew, A.; Lim, S. H.; Lee, H. B.; Kiew, L. V.; Chung, L. Y.; Burgess, K., BODIPY dyes in photodynamic therapy. *Chemical Society Reviews* **2013**, *42* (1), 77-88.
32. Rappley, I.; Monteiro, C.; Novais, M.; Baranczak, A.; Solis, G.; Wiseman, R. L.; Helmke, S.; Maurer, M. S.; Coelho, T.; Powers, E. T.; Kelly, J. W., Quantification of transthyretin kinetic stability in human plasma using subunit exchange. *Biochemistry* **2014**, *53* (12), 1993-2006.
33. Zhao, H.; Dietrich, J., Privileged scaffolds in lead generation. *Expert Opin Drug Discov* **2015**, *10* (7), 781-90.
34. Kaur, I.; Jazdyk, M.; Stein, N. N.; Prusevich, P.; Miller, G. P., Design, Synthesis, and Characterization of a Persistent Nonacene Derivative. *Journal of the American Chemical Society* **2010**, *132* (4), 1261-1263.
35. Singh, M.; Singh, S. K., Benzothiazoles: how relevant in cancer drug design strategy? *Anticancer Agents Med Chem* **2014**, *14* (1), 127-46.
36. Rajasekhar, S.; Maiti, B.; Chanda, K., A Decade Update on Benzoxazoles, a Privileged Scaffold in -Synthetic Organic Chemistry. *Synlett* **2017**, *28* (05), 521-541.

37. Mancini, D. T.; Sen, K.; Barbatti, M.; Thiel, W.; Ramalho, T. C., Excited-State Proton Transfer Can Tune the Color of Protein Fluorescent Markers. *Chemphyschem* **2015**, *16* (16), 3444-9.
38. Skonieczny, K.; Charalambidis, G.; Tasiar, M.; Krzeszewski, M.; Kalkan-Burat, A.; Coutsolelos, A. G.; Gryko, D. T., General and Efficient Protocol for Formylation of Aromatic and Heterocyclic Phenols. *Synthesis* **2012**, *44* (23), 3683-3687.
39. Dhankher, P.; Sheppard, T. D., A Convenient Synthesis of Tri- and Tetramethylbenzaldehydes from Readily Available Phenols. *Synlett* **2014**, *25* (03), 381-384.
40. Lashuel, H. A.; Wurth, C.; Woo, L.; Kelly, J. W., The Most Pathogenic Transthyretin Variant, L55P, Forms Amyloid Fibrils under Acidic Conditions and Protofilaments under Physiological Conditions. *Biochemistry* **1999**, *38* (41), 13560-13573.
41. Wiseman, R. L.; Green, N. S.; Kelly, J. W., Kinetic Stabilization of an Oligomeric Protein under Physiological Conditions Demonstrated by a Lack of Subunit Exchange: Implications for Transthyretin Amyloidosis. *Biochemistry* **2005**, *44* (25), 9265-9274.

### CHAPTER 3. SUBSTITUENT EFFECTS ON THE PHOTOPHYSICAL PROPERTIES OF 2-(2'-HYDROXYPHENYL)-BENZOXAZOLE AND THEIR ROLE IN THE EXCITED-STATE INTRAMOLECULAR PROTON TRANSFER

Bryan J. Lampkin, Daniel Arriaga, Caroline C. Warner, Brett VanVeller\*

Department of Chemistry, Iowa State University, Ames, Iowa 50011, USA

Modified from a manuscript to be submitted

#### Abstract

Organic chromophores that can undergo ESIPT fluorescence have ability to be dual emissive and are solvent dependent thus rendering them environmentally sensitive. Despite the increase in use of ESIPT-capable probes, general design principles with respect to functional group substitution to either enhance their photophysical properties or their probe sensitivity are lacking. Herein we present a systematic study of the photophysical properties of 25 unique monosubstituted 2-(2'-hydroxyphenyl)-benzoxazole (HBO) dyes across four different solvents. We anticipate that the results presented here will better inform future HBO ESIPT probe development.

#### Introduction

Environmentally sensitive chromophores are important tools for the study of molecular events which perturb the surrounding microenvironment.<sup>1</sup> For example, environmentally sensitive dyes have been employed to investigate protein-protein interactions,<sup>2</sup> analyte detection,<sup>3</sup> and solvent properties such as polarity<sup>4</sup> or pH.<sup>5</sup> Further, they enable direct analysis of a biological sample while avoiding any processing steps, such as washing steps necessary for cell studies.<sup>6-8</sup> One popular mechanism of environmentally sensitive fluorescence is the Excited-State Intramolecular Proton Transfer (ESIPT) fluorescence<sup>1, 9-12</sup> of which the 2-(2'-hydroxyphenyl)-benzoxazole (HBO) and their thiazole (HBT) and imidazole (HBI) analogs are the most common.



ESIPT is an adiabatic photochemical process that occurs when a chromophore, **E**, containing an intramolecular hydrogen bond absorbs a photon of light and gets excited to **E\***. From there, **E\*** can radiatively relax back to **E** or can subsequently isomerize to form a more stable tautomer, **K\***, in the excited state (Figure 3.1).<sup>9, 10</sup> This tautomer then will relax back to the ground state releasing a photon of light that is more red-shifted relative to the emission without the excited-state isomerization. The structural reorganization of the dye that results from this isomerization leads to a large Stokes shift observed of the emitted photon. Having a mechanism at which both a red-shifted emission and a large Stokes shift occurs is desirable in organic dyes and therefore makes ESIPT dyes attractive fluorescent probe candidates.

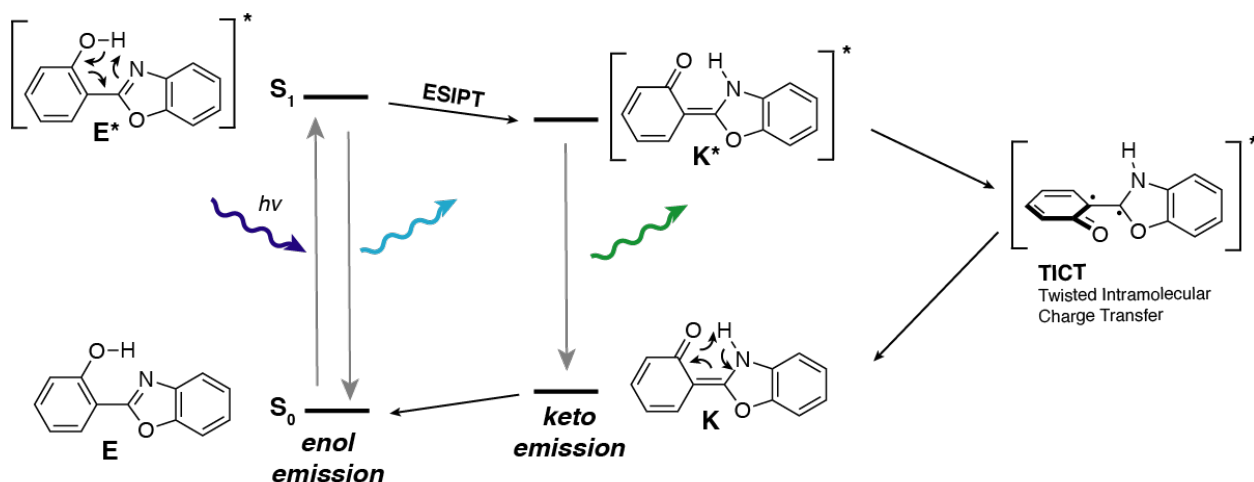


Figure 3.1 The ESIPT photochemical cycle of HBO. **E** absorbs a photon and is excited to **E\*** which can either radiatively relax to achieve enol emission or it can undergo ESIPT to **K\***. **K\*** can then either radiatively relax to achieve keto emission or it can undergo TICT which subsequently non-radiatively relaxes back to **K**.

In addition to the red-shifted emission and large Stokes shift properties, ESIPT dyes are also considered to be environmentally sensitive.<sup>1</sup> In protic solvents, excited-state isomerization is impeded and “normal” fluorescence persists. Alternatively, in aprotic solvents or a desolvated

environment, intramolecular proton transfer becomes favorable and occurs very rapidly (~ps). Thus, the dual emissive property of ESIPT probes enable the reporting of the composition of their microenvironment, such as binding to a protein. The two-channel output of ESIPT dyes allows for a ratiometric output which improves measurement sensitivity and is self-calibrating. Along those same lines, the dual emission of ESIPT dyes are being capitalized in efforts to engineer white-light emitting chromophores.<sup>13, 14</sup> Additionally, there is evidence that a quenching mechanism of HBO ESIPT fluorescence occurs in the form of a twisted internal charge transfer (TICT) event where the dye non-radiatively decays by twisting such that the two aryl systems are orthogonal to one another.<sup>15-18</sup> This also allows ESIPT dyes to report on the relative rigidity of their microenvironment (e.g. solvent viscosity or host binding affinity). HBO type dyes are also effective ESIPT fluorescence in the solid-state,<sup>19, 20</sup> which is attributed to the inhibition of the TICT quenching mechanism. Thus, HBO ESIPT fluorescence provides two separate channels of environmental sensitivity – solvent polarity and rigidity.

The multi-faceted responsiveness of HBO chromophores makes them perplexing fluorescent molecules. Despite the intensive research into their photophysical properties and their increased use as fluorescent probes,<sup>21-26</sup> design principles to best capture this responsiveness have been slow to emerge. Several standalone studies of functionalized HBO derivatives,<sup>27-30</sup> albeit small in sample size, allow for extrapolated *rules of thumb* in designing ESIPT properties. A systematic study into the effects of substitution on ESIPT dyes would greatly enhance our understanding of these design principles. In an effort to address this void, Jacquemin and coworkers performed a computational analysis of functionalized HBO molecules with an emphasis on elucidating energetic criteria that allow for dual emission.<sup>31</sup> Their study verified the general observations that electron withdrawing groups on the benzoxazole of HBO and electron

donating groups, irrespective of location, favor enol emission, as well as provided an energetic window to achieve dual emission. Their results allow for the comparison to experiment and thus additional optimizing ESIPT design rules.

In the present study, we performed a systematic analysis of mono-substituted HBO dyes and characterized their photophysical properties. Four different locations on the HBO scaffold were evaluated and the substituent was selected such that there was a representative sampling of electron donor and withdrawing groups as indicated by the Hammett parameters ( $\sigma_p$ ). In addition to exploring substituent effects, we also examined the effect of solvent polarity on the ESIPT properties of HBO. All fluorescent measurements were taken in dioxane, dichloromethane, acetonitrile and methanol to achieve a large range of polarity and solvent proticity. In all, we surveyed *seven* molecules for each of the *four* R position on the HBO core in *four* different solvents (Figure 3.2). As a result, a plethora of information was obtained. In the following sections we will limit discussions to general observations of electronic and solvent effects on the following properties:

- Absorption and emission wavelengths
- Dual emissive properties
- Stokes shifts for both the enol and keto emission channels
- Quantum yields of fluorescence ( $\Phi_f$ )

Most of the focus on the effect to the substituent will be in dioxane. We will discuss in more detail any observations along the electronic or solvent coordinate that we find worthy of elaboration in their appropriate sections.

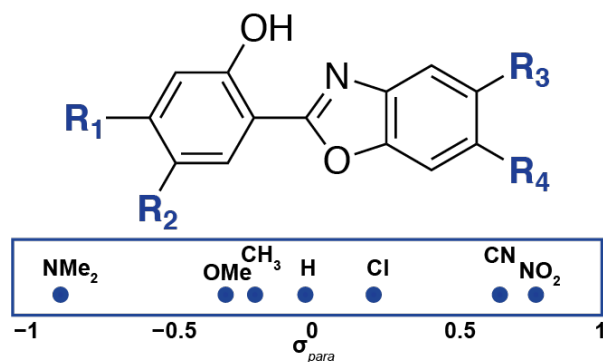


Figure 3.2 ESIPT HBO derivatives studied.  $R_{1,2,3,4}$  represents the location of each of the 6 substituent groups utilized.

## Results and Discussion

### Effect on absorption and emission

Generally speaking, the substituent, regardless of position, does not play a drastic effect in the absorption or emission properties of either the enol or keto channels. Only at the  $R_2$  position does more electron donation increase the absorption and emission wavelengths as it does in traditional chromophores. This has the largest effect in dioxane when a keto emission range of ~600 nm to ~470 nm for  $\text{NMe}_2$  and  $\text{NO}_2$  groups, respectively (Figure 3.3 and Table 3.2). The emission range for the  $R_2$  position is ~570nm to 470nm in methanol and thus this appears to be only slightly solvent dependent. Although the introduction of an EDG in the  $R_2$  position red-shifts its spectroscopic parameters, it also has a general inverse effect on the relative dual emission abilities and thus inhibits keto emission to a degree (see below).

Table 3.1 Spectral properties of R<sub>1</sub> HBO derivatives

R	Solvent	Absorption (nm)	Enol Emission (nm)	Keto Emission (nm)	Normalized Ratio <sup>a</sup>	$\Phi_{fl}^b$		
H 0.0	Dioxane, 0.164	320	357	494	0.8643	0.014	±	0.002
	Dichloromethane, 0.309	320	-	488	0.9903	0.029	±	0.006
	Acetonitrile, 0.46	318	354	486	0.7712	0.018	±	0.001
	Methanol, 0.762	319	430	-	0.0092	0.119	±	0.020
1 NO <sub>2</sub> 0.778	Dioxane, 0.164	359	407	554	0.9004	0.047	±	0.004
	Dichloromethane, 0.309	363	415	585	0.6499	0.011	±	0.002
	Acetonitrile, 0.46	359	404	454	0.3499	0.006	±	0.001
	Methanol, 0.762	358	408	454	0.4881	0.002	±	0.000
1 CN 0.66	Dioxane, 0.164	328	417	493	0.7716	0.017	±	0.005
	Dichloromethane, 0.309	321	422	489	0.7912	0.013	±	0.003
	Acetonitrile, 0.46	327	431	486	0.7985	0.018	±	0.006
	Methanol, 0.762	327	448	-	0.0155	0.085	±	0.043
1 Cl 0.227	Dioxane, 0.164	322	415	477	0.8989	0.059	±	0.006
	Dichloromethane, 0.309	322	415	471	0.8996	0.075	±	0.009
	Acetonitrile, 0.46	320	-	472	0.9434	0.046	±	0.012
	Methanol, 0.762	361	422	-	0.0018	0.124	±	0.006
1 Me -0.17	Dioxane, 0.164	320	430	491	0.8442	0.017	±	0.001
	Dichloromethane, 0.309	322	426	479	0.7021	0.024	±	0.011
	Acetonitrile, 0.46	319	432	475	0.6560	0.016	±	0.001
	Methanol, 0.762	321	430	-	0.0118	0.122	±	0.009
1 OMe -0.268	Dioxane, 0.164	321	409	471	0.5505	0.018	±	0.002
	Dichloromethane, 0.309	321	409	463	0.5331	0.020	±	0.005
	Acetonitrile, 0.46	319	410	-	0.0252	0.041	±	0.008
	Methanol, 0.762	319	409	-	0.0067	0.088	±	0.018
1 NMe <sub>2</sub> -0.83	Dioxane, 0.164	360	393	-	0.0054	0.129	±	0.001
	Dichloromethane, 0.309	360	401	-	0.0045	0.144	±	0.010
	Acetonitrile, 0.46	358	401	-	0.0034	0.238	±	0.022
	Methanol, 0.762	358	394	-	0.0033	0.079	±	0.027

<sup>a</sup> Normalized ratio calculated as  $I_{\text{keto emission}} / (I_{\text{keto emission}} + I_{\text{enol emission}})$ . <sup>b</sup> Quantum yield determined in triplicate in degassed solvent. See experimental details for more information.

Table 3.2 Spectral properties of R<sub>2</sub> HBO derivatives

R	Solvent	Absorption (nm)	Enol Emission (nm)	Keto Emission (nm)	Normalized Ratio <sup>a</sup>	$\Phi_{fl}^b$	
2	Dioxane, 0.164	331	406	474	0.8000	0.010 ± 0.000	
2	NO <sub>2</sub> 0.778	Dichloromethane, 0.309	331	387	484	0.6562	0.008 ± 0.001
2		Acetonitrile, 0.46	329	404	466	0.5499	0.003 ± 0.000
2		Methanol, 0.762	330	402	488	0.5465	0.005 ± 0.001
2		Dioxane, 0.164	320	425	474	0.8325	0.143 ± 0.015
2	CN 0.66	Dichloromethane, 0.309	320	-	472	0.9895	0.189 ± 0.009
2		Acetonitrile, 0.46	320	411	470	0.9518	0.134 ± 0.028
2		Methanol, 0.762	355	420	-	0.0027	0.078 ± 0.016
2		Dioxane, 0.164	330	437	495	0.7610	0.036 ± 0.006
2	Cl 0.227	Dichloromethane, 0.309	327	414	489	0.8325	0.064 ± 0.006
2		Acetonitrile, 0.46	328	446	-	0.0192	0.033 ± 0.001
2		Methanol, 0.762	326	431	490	0.9254	0.097 ± 0.037
2		Dioxane, 0.164	328	445	501	0.7337	0.012 ± 0.001
2	Me -0.17	Dichloromethane, 0.309	327	445	501	0.7337	0.027 ± 0.001
2		Acetonitrile, 0.46	326	450	-	0.0167	0.010 ± 0.001
2		Methanol, 0.762	325	450	495	0.6502	0.086 ± 0.006
2		Dioxane, 0.164	346	475	512	0.5463	0.029 ± 0.008
2	OMe -0.268	Dichloromethane, 0.309	347	479	496	0.4093	0.056 ± 0.004
2		Acetonitrile, 0.46	345	487	515	0.4011	0.022 ± 0.001
2		Methanol, 0.762	347	480	-	0.0501	0.117 ± 0.006
2		Dioxane, 0.164	387	479	591	0.4110	0.022 ± 0.005
2	NMe <sub>2</sub> -0.83	Dichloromethane, 0.309	387	465	562	0.6165	0.093 ± 0.044
2		Acetonitrile, 0.46	384	-	559	0.9866	0.015 ± 0.005
2		Methanol, 0.762	388	497	569	0.5471	0.036 ± 0.012

<sup>a</sup> Normalized ratio calculated as  $I_{\text{keto emission}} / (I_{\text{keto emission}} + I_{\text{enol emission}})$ . <sup>b</sup> Quantum yield determined in triplicate in degassed solvent. See experimental details for more information.

Table 3.3 Spectral properties of R<sub>3</sub> HBO derivatives

R	Solvent	Absorption (nm)	Enol Emission (nm)	Keto Emission (nm)	Normalized Ratio <sup>a</sup>	$\Phi_{fl}$ <sup>b</sup>			
3	Dioxane, 0.164	328	423	440	0.5439	0.007	±	0.002	
3	NO <sub>2</sub> 0.778	Dichloromethane, 0.309	328	371	482	0.5912	0.009	±	0.003
3		Acetonitrile, 0.46	325	393	475	0.6151	0.005	±	0.002
3		Methanol, 0.762	328	367	452	0.6017	0.005	±	0.001
3		Dioxane, 0.164	324	369	487	0.4960	0.004	±	0.002
3	CN 0.66	Dichloromethane, 0.309	323	436	478	0.6131	0.014	±	0.006
3		Acetonitrile, 0.46	320	370	490	0.4267	0.002	±	0.001
3		Methanol, 0.762	322	377	455	0.4946	0.005	±	0.001
3		Dioxane, 0.164	323	389	487	0.5786	0.016	±	0.005
3	Cl 0.227	Dichloromethane, 0.309	323	400	486	0.6491	0.013	±	0.006
3		Acetonitrile, 0.46	322	369	467	0.7937	0.019	±	0.010
3		Methanol, 0.762	322	373	442	0.7589	0.033	±	0.009
3		Dioxane, 0.164	322	376	484	0.5897	0.043	±	0.002
3	Me -0.17	Dichloromethane, 0.309	323	419	476	0.6113	0.047	±	0.008
3		Acetonitrile, 0.46	321	430	459	0.4948	0.056	±	0.015
3		Methanol, 0.762	323	431	451	0.4719	0.070	±	0.023
3		Dioxane, 0.164	328	421	491	0.8087	0.006	±	0.001
3	OMe -0.268	Dichloromethane, 0.309	328	419	479	0.7952	0.007	±	0.003
3		Acetonitrile, 0.46	325	416	471	0.5664	0.006	±	0.002
3		Methanol, 0.762	325	433	482	0.2916	0.013	±	0.005
3		Dioxane, 0.164	328	472	-	0.0043	0.006	±	0.001
3	NMe <sub>2</sub> -0.83	Dichloromethane, 0.309	328	481	-	0.0069	0.007	±	0.003
3		Acetonitrile, 0.46	325	518	-	0.0070	0.006	±	0.002
3		Methanol, 0.762	325	511	-	0.0169	0.013	±	0.005

<sup>a</sup> Normalized ratio calculated as  $I_{\text{keto emission}} / (I_{\text{keto emission}} + I_{\text{enol emission}})$ . <sup>b</sup> Quantum yield determined in triplicate in degassed solvent. See experimental details for more information.

Table 3.4 Spectral properties of R<sub>4</sub> HBO derivatives

R	Solvent	Absorption (nm)	Enol Emission (nm)	Keto Emission (nm)	Normalized Ratio <sup>a</sup>	Φ <sub>fl</sub> <sup>b</sup>		
4	Dioxane, 0.164	327	430	460	0.4882	0.013	±	0.002
4	NO <sub>2</sub> 0.778	Dichloromethane, 0.309	326	431	450	0.5388	0.041	± 0.036
4		Acetonitrile, 0.46	327	362	464	0.9699	0.048	± 0.017
4		Methanol, 0.762	326	362	462	0.9421	0.031	± 0.009
4		Dioxane, 0.164	329	371	506	0.6378	0.014	± 0.001
4	CN 0.66	Dichloromethane, 0.309	330	372	503	0.8233	0.011	± 0.006
4		Acetonitrile, 0.46	327	375	498	0.5012	0.013	± 0.006
4		Methanol, 0.762	325	386	470	0.7199	0.016	± 0.004
4		Dioxane, 0.164	323	379	485	0.5276	0.016	± 0.005
4	Cl 0.227	Dichloromethane, 0.309	323	404	485	0.6945	0.010	± 0.008
4		Acetonitrile, 0.46	322	381	473	0.6901	0.019	± 0.010
4		Methanol, 0.762	322	372	441	0.6697	0.033	± 0.009
4		Dioxane, 0.164	322	-	486	0.8623	0.016	± 0.005
4	Me -0.17	Dichloromethane, 0.309	322	-	481	0.9363	0.023	± 0.005
4		Acetonitrile, 0.46	320	425	482	0.8058	0.015	± 0.004
4		Methanol, 0.762	321	365	449	0.7018	0.076	± 0.020
4		Dioxane, 0.164	328	368	485	0.7230	0.006	± 0.001
4	OMe -0.268	Dichloromethane, 0.309	328	370	475	0.8181	0.007	± 0.003
4		Acetonitrile, 0.46	325	370	485	0.7079	0.006	± 0.002
4		Methanol, 0.762	325	370	424	0.7634	0.013	± 0.005
4		Dioxane, 0.164	324	426	-	0.0075	0.330	± 0.068
4	NMe <sub>2</sub> -0.83	Dichloromethane, 0.309	323	437	-	0.0062	0.140	± 0.029
4		Acetonitrile, 0.46	322	461	-	0.0003	0.139	± 0.076
4		Methanol, 0.762	324	464	-	0.0002	0.077	± 0.035

<sup>a</sup> Normalized ratio calculated as I<sub>keto emission</sub>/(I<sub>keto emission</sub> + I<sub>enol emission</sub>). <sup>b</sup> Quantum yield determined in triplicate in degassed solvent. See experimental details for more information.



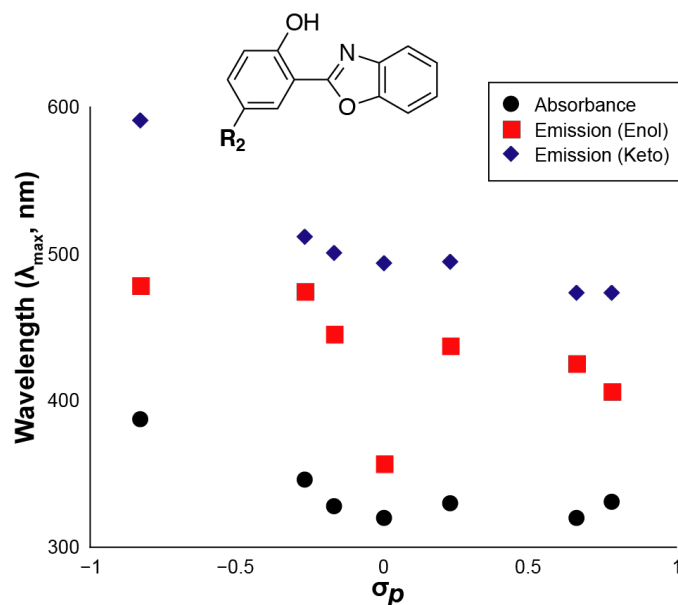


Figure 3.3 Functional group dependence at the R2 position on the absorption, enol emission, and keto emission max in dioxane as a function of the para Hammett parameters ( $\sigma_p$ ).

A common intellectual musing of ESIPT chromophores is the interplay between excited-state proton transfer and internal charge transfer (ICT).<sup>32-34</sup> Spectroscopic signatures of an ICT event are a red-shift in the absorption or emission as a function of solvent polarity and therefore making ICT fluorescence solvatochromatic.<sup>4</sup> Typically, charge transfer occurs in the excited-state enol form which manifests itself in the enol emission. However, strong electron accepting groups, such as a dicyanovinyl group in the R<sub>4</sub> position induces a large solvatochromic response in the keto emission channel.<sup>35</sup> This was rationalized by resonance delocalization between the keto-form nitrogen and *para* EWG. Interestingly, none of the EWG in the R<sub>4</sub> position displayed solvatochromic behavior to a comparable degree to that of the dicyanovinyl withdrawing group suggesting that only very strong EWG are capable of inducing solvatochromic behavior in ESIPT dyes. It is worth mentioning that a very small solvatochromic effect was observed, in a

separate study, by a disubstituted HBO chromophore where a strong donor, NMe<sub>2</sub> was placed in the R<sub>1</sub> position and a strong acceptor, NO<sub>2</sub>, was placed in the R<sub>4</sub> position.<sup>28</sup>

Only the NMe<sub>2</sub> substitution in the R<sub>3</sub> position shows modest solvatochromic behavior in the enol emission channel (Table 3.3). Prior work on a similar HBO derivative with an NH<sub>2</sub> group in the R<sub>3</sub> position also observed this behavior.<sup>30</sup> Additionally, they showed that only keto emission was observed in *n*-heptane and that enol emission occurred in all other solvents. We rationalize that because NMe<sub>2</sub> is a stronger EDG than NH<sub>2</sub>, this particular HBO derivative is even less sensitive to solvent polarity and the electron donating nature of the NMe<sub>2</sub> shuts down ESIPT altogether.

### Effect on dual emission

To evaluate the effect the substituent or solvent had on the dual emission of the analyzed HBO chromophores, we looked at the emission intensities of peaks characterized to either the enol or keto forms. Additionally, to standardize the relative peak heights, we introduced a ratio parameter such that a value of 1.0 indicates fully keto emission, a value of 0.0 indicates fully enol emission, and a value of 0.5 indicates a 1:1 peak height ratio.

Surprisingly, the ratio of keto to enol emission was not observed to be as solvent dependent as expected (Figure 3.7).<sup>36, 37</sup> Yes, this solvent dependency was observed in some cases – particularly the base HBO molecule and OMe substituent in the R<sub>1-3</sub> position. However, this was not widely observed. For instance, at the R<sub>3</sub> position, the NO<sub>2</sub>, CN, Cl, and Me substituents showed consistently dual emission where only the methyl showed moderately lower keto emission in acetonitrile and methanol (Table 3.3 and Figure 3.7). Additionally, the NMe<sub>2</sub> substituent at the R<sub>2</sub> position *increased* keto emission as the solvent became more polar such that only keto emission was observed in methanol. Increasing keto emission in more polar solvents,

while not expected, is not unprecedented as ESIPT has been observed in 2-phenylphenol derivatives with electron donating groups para to the phenol in polar protic solvents.<sup>38</sup>

The substituent effect on the dual emission of HBO derivatives is much more pronounced. Classically, excited-state proton transfer can be viewed as an increase in phenol acidity and benzoxazole basicity upon photo excitation.<sup>31, 39</sup> This is manifested in electron density difference plots that show only a very slight increase in electron density on the phenol oxygen but a large increase in benzoxazole nitrogen electron density upon excitation. It goes to reason that there should be a substituent effect in the dual emission properties of HBO.

In dioxane, at least, the R<sub>1</sub> and R<sub>2</sub> positions favored keto emission as the substituent became more electron withdrawing. On the other hand, at the R<sub>3</sub> and R<sub>4</sub> positions, enol emission becomes more dominate as the substituent becomes more electron withdrawing with the exception of the NMe<sub>2</sub> group where emission is all enol (Table 3.2 and Figure 3.11). Dioxane, as the least nonpolar solvent that was tested, should induce the most keto emission in all of the dyes. Yet, the results presented here suggest that ESIPT enol:keto ratios can be electronically tuned. In fact, the aforementioned computational study on the substituent effects of HBO dyes estimated that for dual emission to occur, the keto excited-state isomer should be anywhere from 0.0-0.2 kcal/mol lower in energy than the excited state enol which can conceivably be accomplished by electronic substitution.<sup>31</sup> Admittedly, their study only examined the substituent effect in cyclohexane, which should induce a larger keto emission response than dioxane.

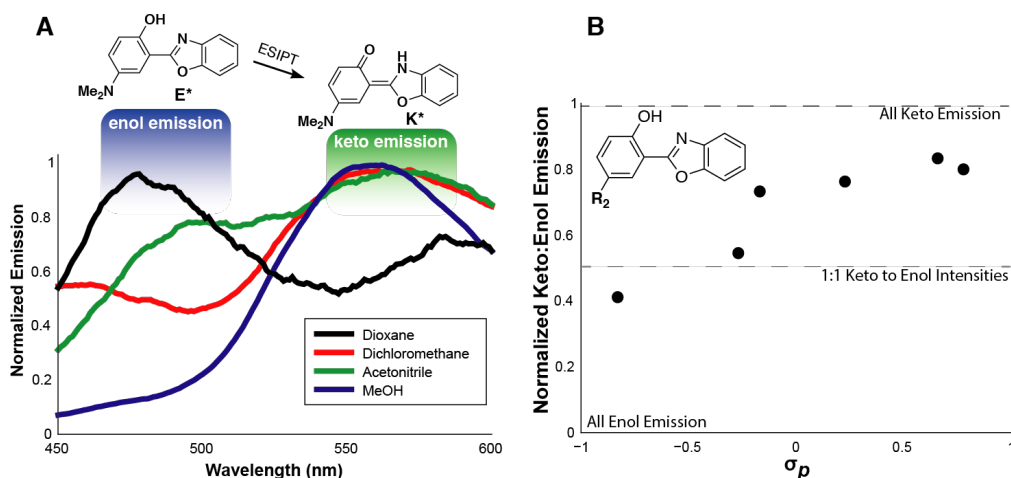


Figure 3.4 Representative dual emission of HBO derivatives. (A) An NMe<sub>2</sub> substituent at the R<sub>2</sub> position induces more keto emission in more polar solvents. (B) The functional group at the R<sub>2</sub> position influences the normalized Keto:Enol ratio. Normalized ratios are such that a value of 1.0 indicates all keto emission and a value of 0.0 indicates all enol emission.

### Effect on the Stokes shift

ESIPT dyes typically exhibit a large Stokes shift, or the difference between the emission and absorption peaks, that results from the large reorganization from the excited-state proton transfer. Even the enol emission Stokes shift appears large when compared to other common chromophores such as Rhodamines, Cyanines, and BODIPY compounds.<sup>40</sup> We have proposed using an ESIPT dye's Stokes shift as a proxy for evaluating the relative stabilization gained in the excited state by isomerizing to the keto form (Figure 3.4A).<sup>41</sup> This assumption does only look at the energy differences (absorptions and emissions) between the ground and excited-states of the enol and keto structures, respectively. Therefore, a large Stokes shift could be a result of both stabilization in the excited-state by isomerization to the keto form and destabilization of **K** in the ground state as a nonaromatic isomer.

There aren't any noticeable solvent effects on the Stokes shift on the evaluated HBO dyes for either the enol or keto emission (Figure 3.8). With respect to substituent effects, both the R<sub>2</sub> and R<sub>3</sub> positions show some sort of dependency. Generally, at the R<sub>2</sub> position, the more

withdrawing the substituent, the Stokes shift decreases for both the enol and keto emissions, although to a greater extent for keto emission and this is consistent across all four solvents (**Error! Reference source not found.**B and Figure 3.12). In dioxane, the NMe<sub>2</sub> substituent has a remarkable Stokes shift of ~200nm in the keto channel! It appears that either **K\*** is stabilized or **K** is destabilized with a more electron donating group thus rendering a larger wavelength Stokes shift. The destabilization of **K** with EDGs is justified as the resultant nitrogen of the benzoxazole is in direct conjugation with the R<sub>2</sub> substituent where instead an EWG would be stabilizing. Interestingly,

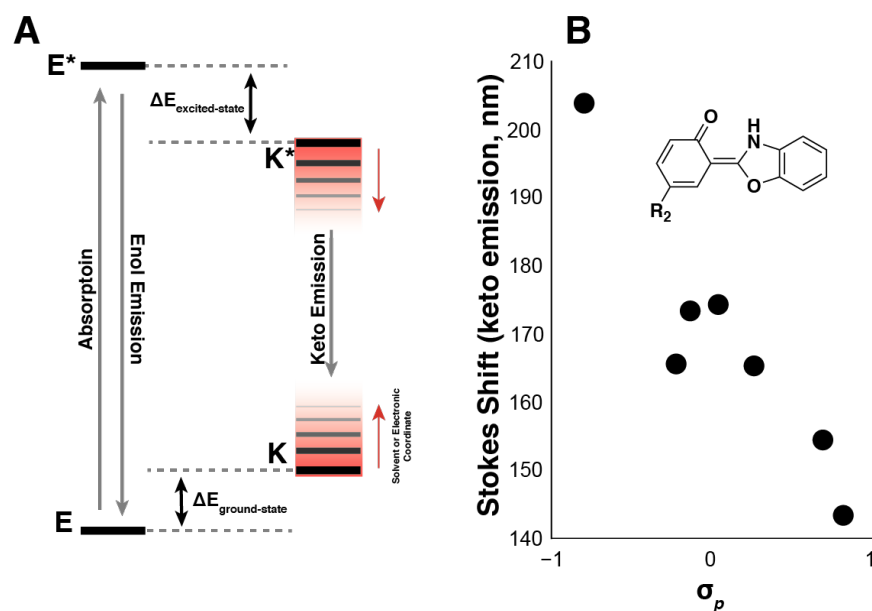


Figure 3.5 Effect on the Stokes shift of HBO analogs. (A) A qualitative schematic of the ESIPIT potential energy surface using only measured absorption and emission values. The electronic or solvent coordinate can tune the keto emission and therefore the relative energies of **K** and **K\***. (B) Functional group dependence on the keto Stokes shift of R<sub>2</sub> derivatized HBO where EWG appear influence the Stokes shift more.

this trend is stronger for EWG likely due to this resonance stabilization. The stabilization of **K\*** with an R<sub>2</sub> EDG, however, is difficult to rationalize as are many other excited-state properties using intuitive organic chemistry concepts. Thus, an electron withdrawing R<sub>2</sub> substituent must

stabilize **K** to a greater extent than it stabilizes **K\*** and therefore increasing the energy difference between the two. This same  $R_2$  substituent effect has also been observed in 2-(2'-hydroxyphenyl)-imidazo[1,2- $\alpha$ ]pyridine (IMPY) ESIPT chromophores.<sup>19</sup> The calculated difference in the IMPY derivatives HOMO/LUMO energy levels did in fact increase with a more EWG where the HOMO energy was stabilized more by an EWG than the LUMO. potential energy surface using only measured absorption and emission values. The electronic or solvent coordinate can tune the keto emission and therefore the relative energies of **K** and **K\***.

It is interesting to notice the reciprocal behavior of the functional group dependence at the  $R_2$  position on the dual emission and Stokes shift of HBO derivatives. As the  $R_2$  position becomes more electron withdrawing, the keto emission ratio increases suggesting a dependency on the excited-state acidity of the phenol. Alternatively, as just discussed, the Stokes shift increases with a more electron donating  $R_2$  group. Taken together, this suggests that the acidity of the phenol (a more EWG in the  $R_2$  position) dictates the *propensity* of excited-state isomerization whereas the Stokes shift is governed by the stabilization of the keto isomer in both the ground and excited states.

### Effect on $\Phi_f$

What could be argued as the largest disadvantage to HBO ESIPT dyes is their relatively low  $\Phi_f$  when compared to other, more widely used organic dyes.<sup>42</sup> Although, this is hardly surprising as fluorescence is a zero-sum competition of photochemical rates and environmentally sensitive dyes have built in non-radiative relaxation pathways that have competitive rates to fluorescence. Nevertheless, characterizing the  $\Phi_f$  of HBO dyes allows one to evaluate the solvent and substituent effect on the competition between radiative and non-radiative rates. All  $\Phi_f$  measurements were taken in triplicate in degassed solvents.

Most of the evaluated dyes had  $\Phi_{fl}$  that were less than 5% with a few exceptions observed. For instance, fluorescence in methanol was consistently brighter than the other solvents likely because there is a degree of charge transfer character in the ESIPT that is stabilized by the polar solvent (Figure 3.9 and Figure 3.13). Along the same lines, NMe<sub>2</sub> also displays the largest  $\Phi_{fl}$ , particularly in the R<sub>2</sub> and R<sub>4</sub> positions, which is again likely due to the increased charge transfer nature induced by this substituent. Charge transfer arguments aside, the CN group in the R<sub>2</sub> position is the brightest HBO derivative with a  $\Phi_{fl}$  of ~15% in dioxane. We did not observe an increase in fluorescence intensity as a function of keto to enol ratio which would have been expected on the basis of the TICT charge transfer quenching mechanism as discussed above (i.e. dyes with more keto emission would be less bright).

### Conclusion

In this study, we characterized the photophysical properties of 25 monosubstituted HBO derivatives in four different solvents resulting in 100 unique samples. Properties evaluated include absorption and emissions in both the enol and keto channels, the dual emission properties, the Stokes shifts of both the enol and keto channels, and the quantum yield of fluorescence. While much of the plethora of data generated proved difficult to rationalize, a few clear trends arose from this study.

Largely, we identified that the R<sub>2</sub> position is the most sensitive position on the HBO core to substituent effects on ESIPT photochemical properties. We showed that the absorption and emission in both the enol and keto channels can be red-shifted with stronger electron donating groups. Along the same lines, the Stokes shift can also be increased with stronger electron donating groups. The ratio of keto and enol emission is increased to favored keto emission with more electron withdrawing groups in the R<sub>2</sub> position. Additionally, we note that a CN

substitution at the R<sub>2</sub> position provides some of the highest  $\Phi_f$  that also involves keto emission. Intriguingly, to our knowledge, this position has not been widely exploited in ESIPT probes.

Importantly, we propose that the acidity of the phenol influences the propensity to ESIPT whereas the stability of the keto isomer (both **K** and **K\***) influences the Stokes shift. This was based on the increase in keto emission ratio as the substituent in the R<sub>2</sub> position became more electron withdrawing but the Stokes shift increased as that substituent was more electron donating. The excited state isomerization needs to be a downhill process to a more stable keto form for ESIPT to occur. While substituent effects likely play some role in ESIPT, recent studies have suggested that the isomerization process is an aromaticity driven. Clearly, investigation into the interplay between phenol acidity and phenol aromaticity in ESIPT fluorescence would be intriguing. Also, it is worth noting that while ESIPT properties can be tuned by substituent effect, more drastic variation in ESIPT spectroscopic properties will likely arise from a change in the ESIPT core (HBO to a 3H-indole compound or imidazo[1,2-a]pyridines) as computationally predicted<sup>31</sup> and experimentally observed.<sup>43</sup>

We anticipate that this study will provide the framework in the further development of HBO chromophores as fluorescent probes. Their large Stokes shifts and two channel emission as well as their two degrees of environmental sensitivity (solvent and rigidity) makes them noteworthy candidates for fluorogenic biological probes. We conclude by mentioning that benzoxazoles are considered to be privileged scaffolds in medicinal chemistry.<sup>44</sup> That said, existing benzoxazole ligands, such as Thioflavin T<sup>45</sup> or Tafamidis,<sup>26, 46, 47</sup> can be repurposed into HBO ESIPT chromophores for a variety of biological sensing applications.



## Supplemental Data and Experimental Information

## Measured spectroscopic data as a function of solvent polarity

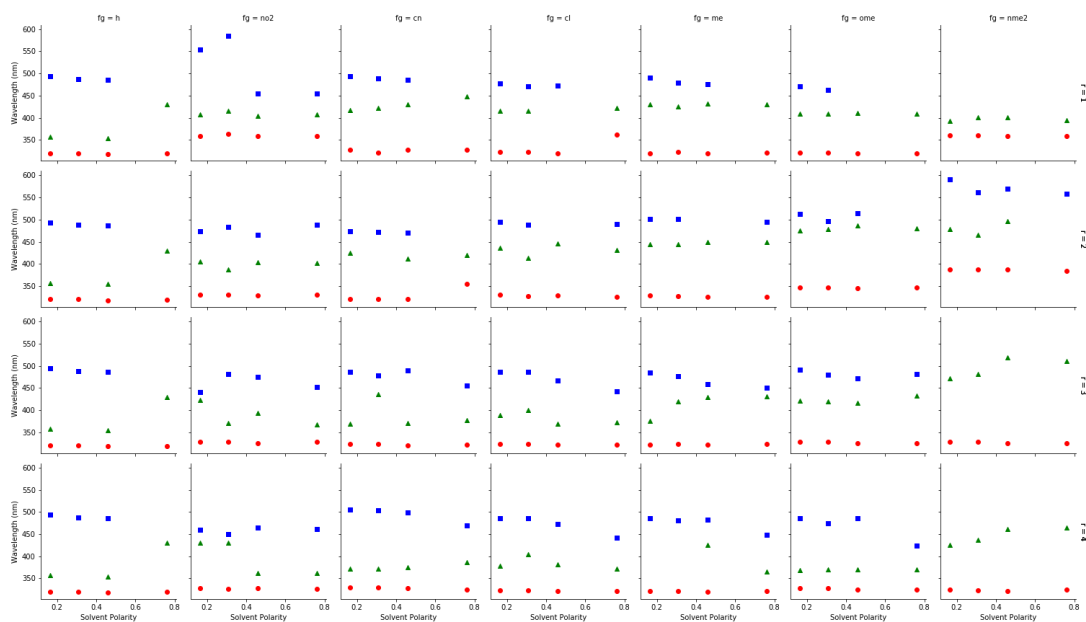


Figure 3.6 Plots of the absorption ( $\bullet$ ), enol emission ( $\blacktriangle$ ), and keto emission ( $\blacksquare$ ) as a function of solvent polarity. Plots are organized by functional group (left to right, H, NO<sub>2</sub>, CN, Cl, Me, OMe, NMe<sub>2</sub>) and substituent location (top to bottom, R<sub>1</sub>, R<sub>2</sub>, R<sub>3</sub>, R<sub>4</sub>).

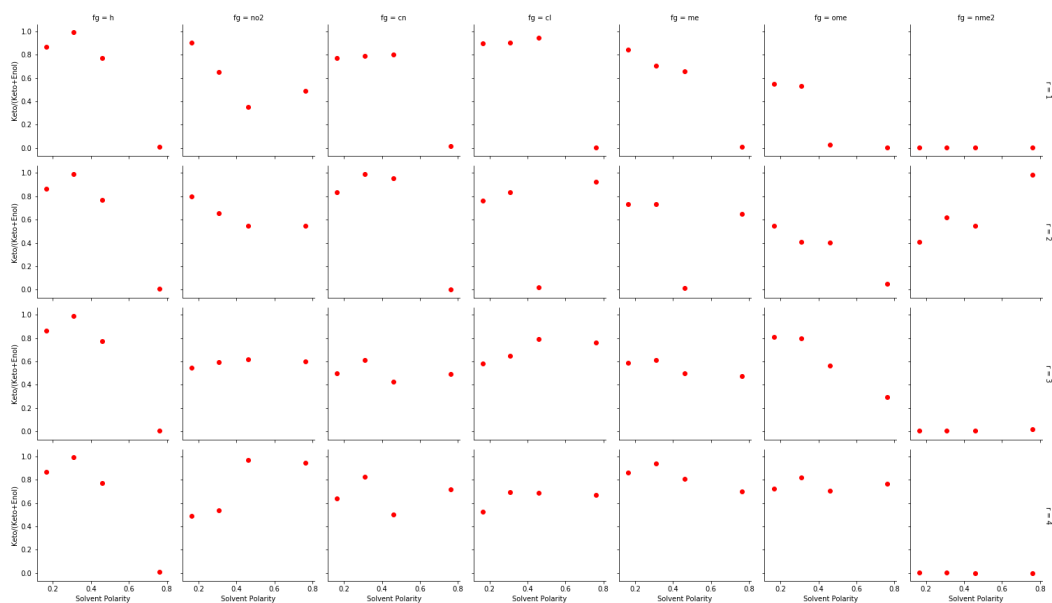


Figure 3.7 Plots of the normalized ratio of keto and enol emission as a function of solvent polarity. Plots are organized the same way as Figure 3.6.

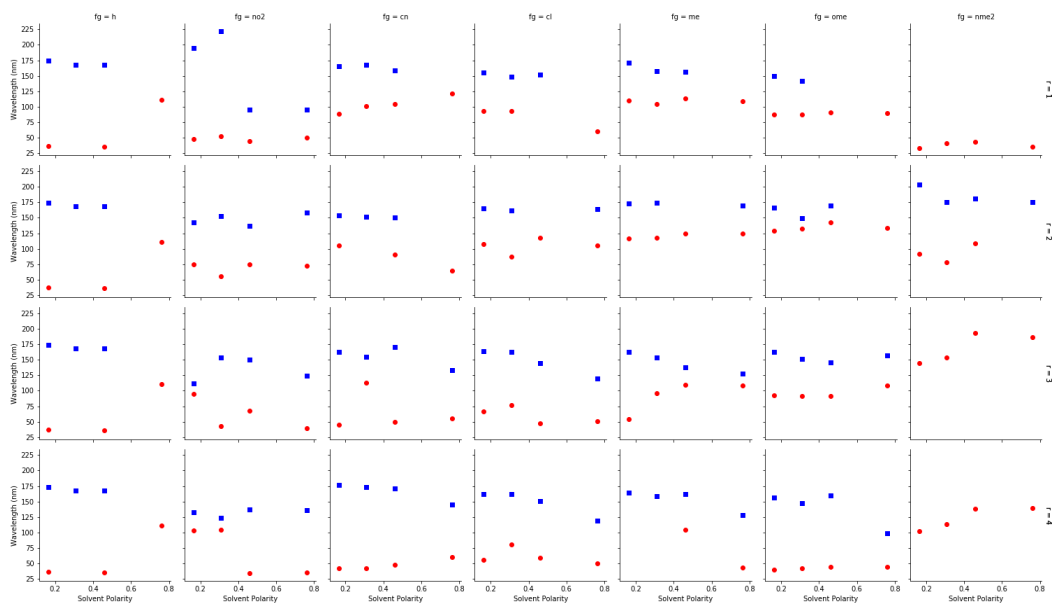


Figure 3.8 Plots of the Stokes shift of enol emission (•) and keto emission (■) as a function of solvent polarity. Plots are organized the same way as Figure 3.6

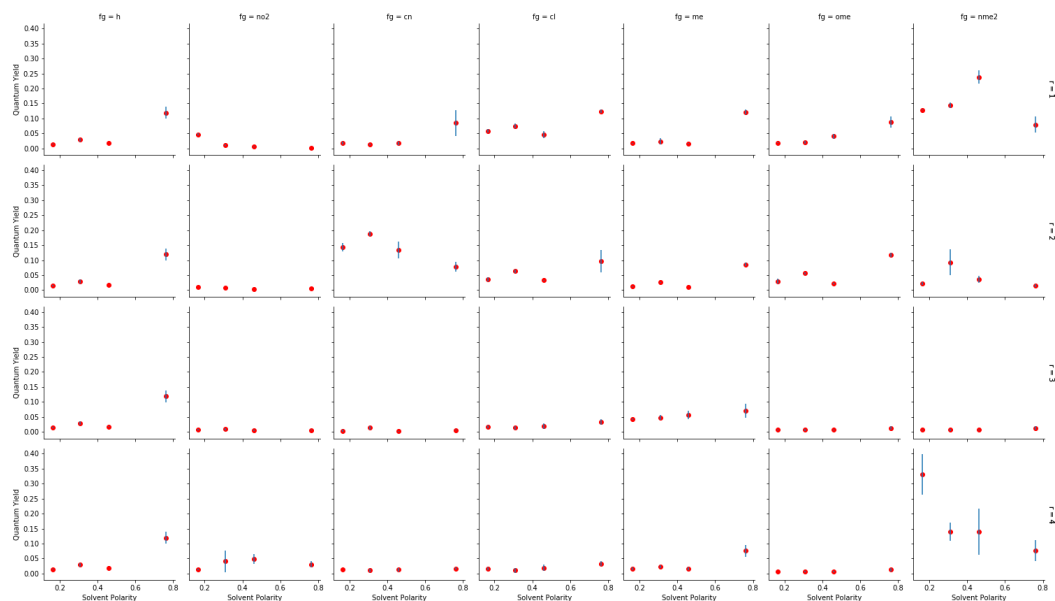


Figure 3.9 Plots of quantum yield as a function of solvent polarity. Measurements were taken in triplicate in degassed solvent. Error bars are shown as  $\pm$  the standard error. Plots are organized the same way as Figure 3.6.

### Measured spectroscopic data as a function of functional group Hammett parameter ( $\sigma_p$ )

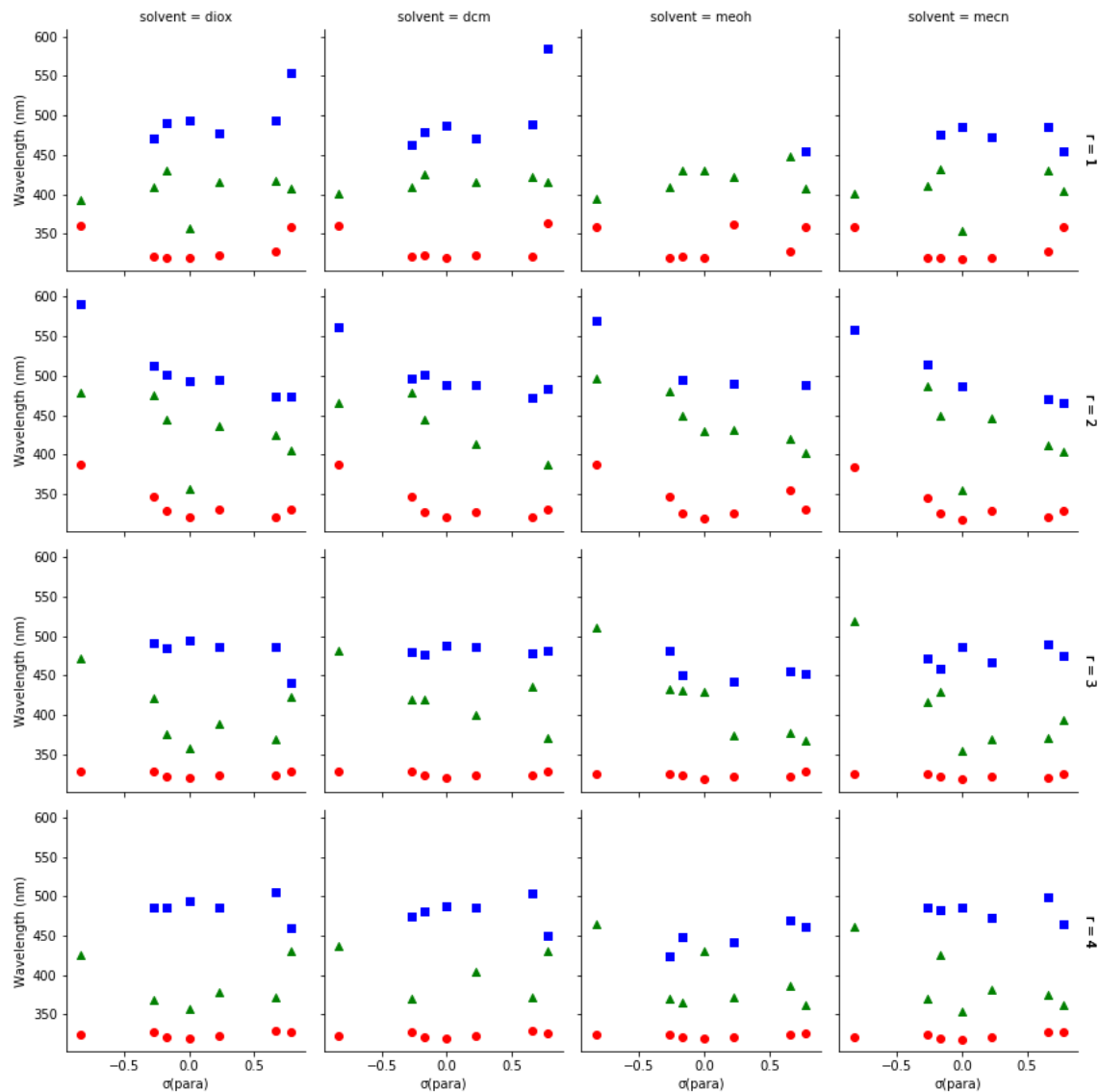


Figure 3.10 Plots of the absorption ( $\bullet$ ), enol emission ( $\blacktriangle$ ), and keto emission ( $\blacksquare$ ) as a function of functional group  $\sigma_p$ . Plots are broken up by solvent (left to right, Dioxane, Dichloromethane, Methanol, Acetonitrile) and substituent location (top to bottom, R<sub>1</sub>, R<sub>2</sub>, R<sub>3</sub>, R<sub>4</sub>).

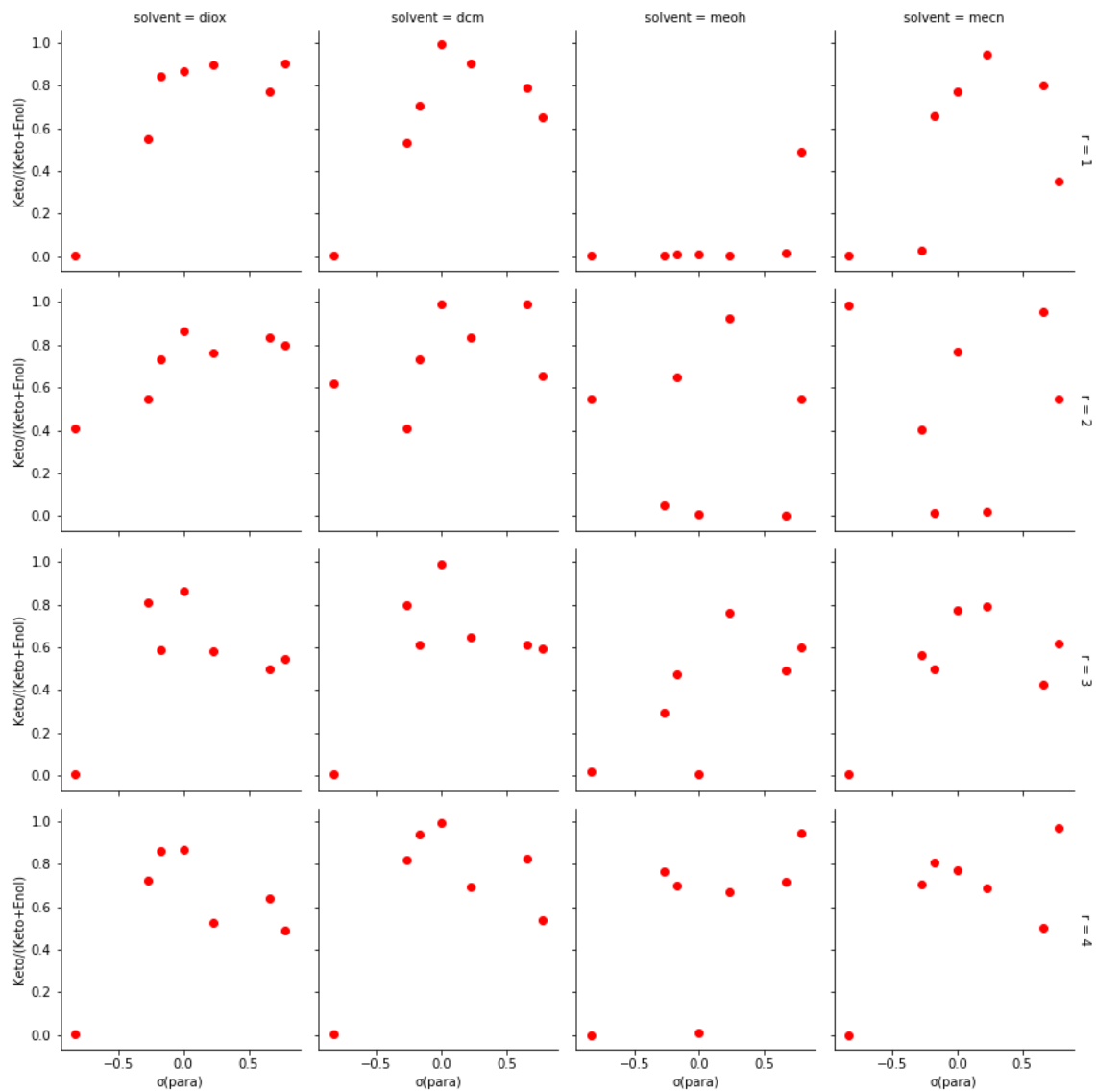


Figure 3.11 Plots normalized ratio of keto and enol emission as a function of functional group  $\sigma_p$ . Plots are organized the same way as Figure 3.10

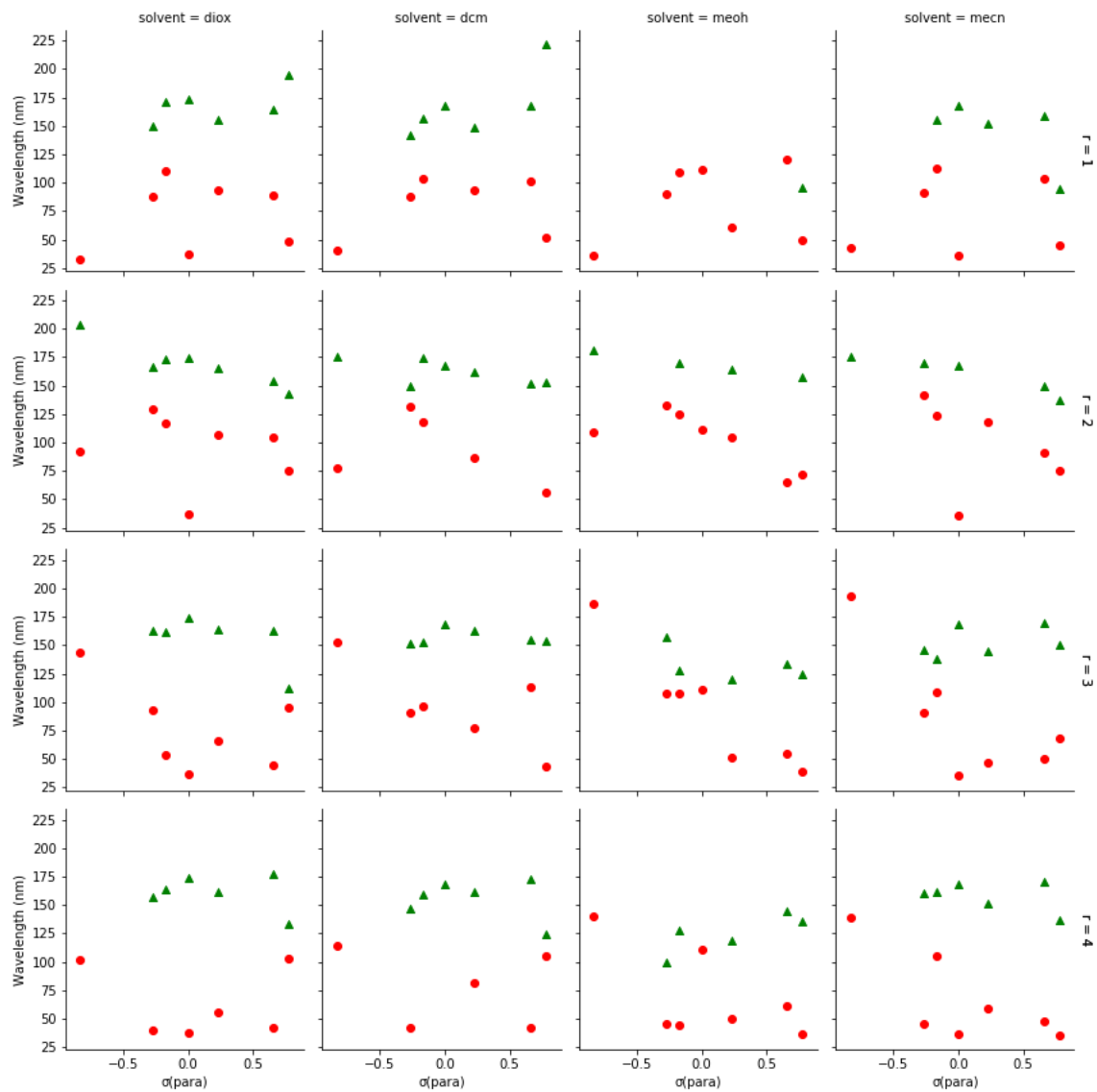


Figure 3.12 Plots Stokes shift of enol emission (•) and keto emission (▲) as a function of functional group  $\sigma_p$ . Plots are organized the same way as Figure 3.10

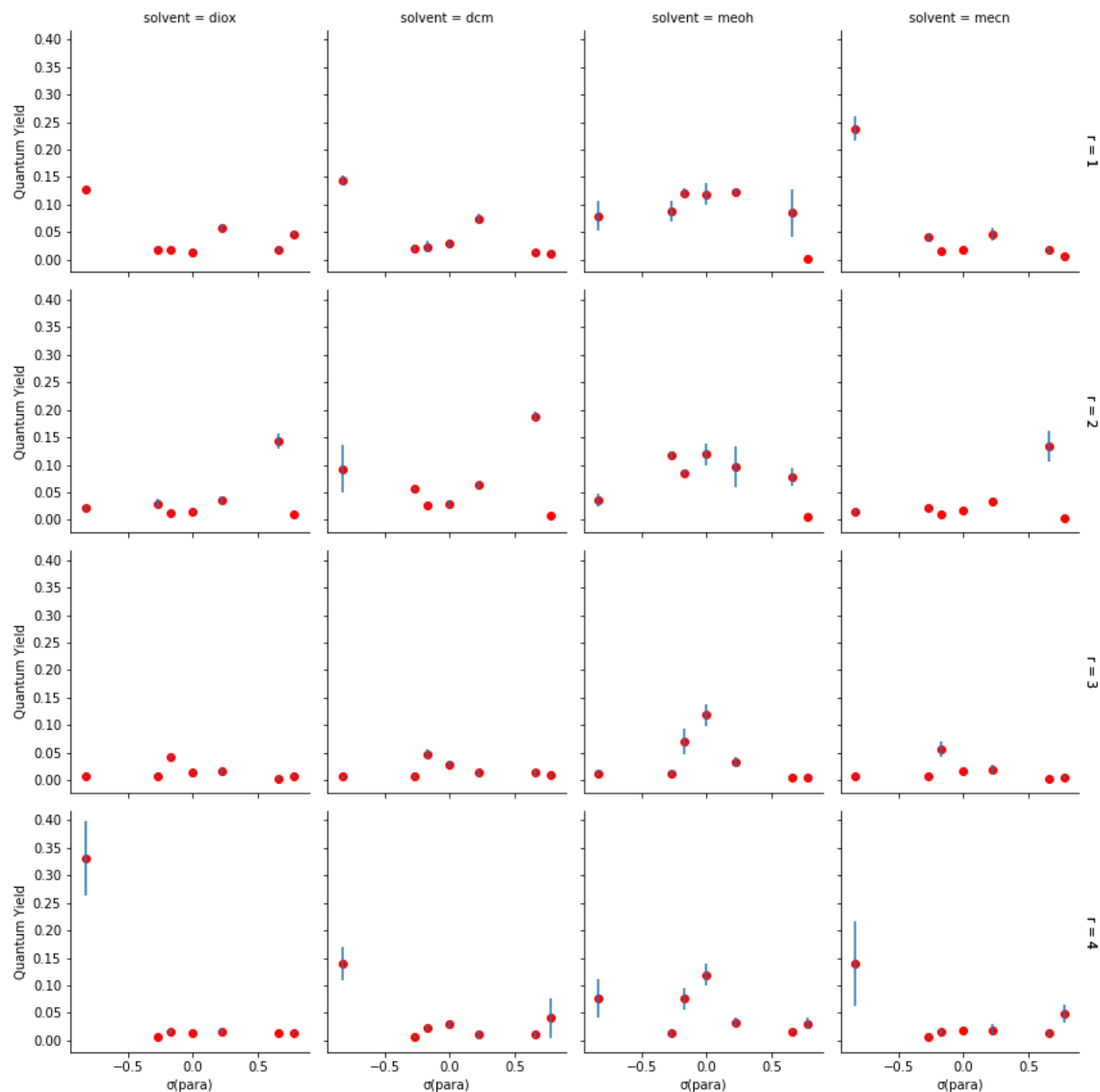


Figure 3.13 Plots of quantum yield as a function of functional group  $\sigma_p$ . Measurements were taken in triplicate in degassed solvent. Error bars are shown as  $\pm$  the standard error. Plots are organized the same way as Figure 3.10

### Quantum yield measurements

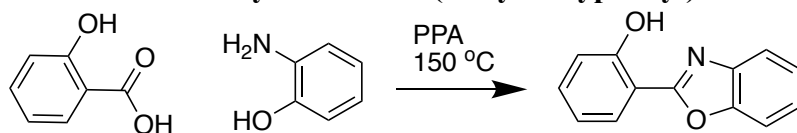
Stock solutions of compounds were made with degassed THF at a concentration of 1 mg/mL.

Quartz cuvettes were sealed with a septa, flushed with nitrogen gas and filled with degassed solvent (2 mL). Solvents were degassed either by the freeze-pump-thaw method or obtained from a solvent system. The stock solution was then added in 1  $\mu$ L increments to the blank solutions

until the desired absorbance was obtained. Final concentrations were calculated based on the amount of stock solution added. Each compound and solvent was tested in triplicate again quinine sulfate as a standard ( $\Phi_{fl} = 0.54$ ).<sup>48</sup>

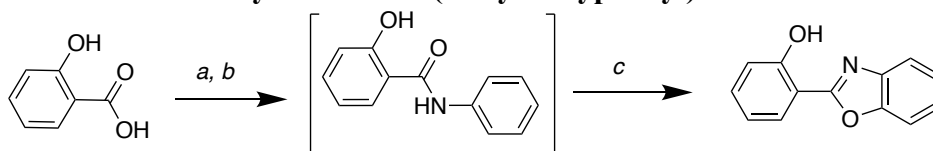
## Synthetic Procedures

### Method 1 for the synthesis of 2-(2'-hydroxyphenyl)benzoxazole derivatives:



Salicylic Acid derivative (1.0 eq.) and 2-Aminophenol derivative (1.2 eq.) were added to a vial with Polyphosphoric Acid (1 mL/mmol) and stirred at 150°C. Upon reaction completion, the reaction was then cooled then quenched with DI water (100x current volume). The solution was then extracted with Ethyl Acetate and the organic phase was concentrated under reduced pressure. The crude product was then purified using silica gel chromatography yielding the target compound as a powder.

### Method 2 for the synthesis of 2-(2'-hydroxyphenyl)benzoxazole derivatives:



*a.* 1.1 eq. (COCl)<sub>2</sub>, cat. DMF, DCM, *b.* 1.2 eq. 2-aminophenol, 1.2 eq. diisopropylethylamine, DCM *c.* TsOH, Toluene, reflux

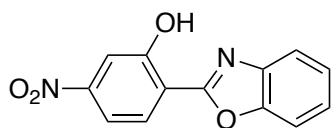
A solution of 1.0 eq. salicylic acid in dichloromethane (0.1 M) was cooled to 0 °C and 1.1 eq. of (COCl)<sub>2</sub> was added dropwise followed by 0.1 eq. of dimethylformamide. The resulting reaction was allowed to stir 0 °C → room temperature over the course of 30 minutes. Upon consumption of starting material, 1.2 eq. of 2-aminophenol was added followed by 1.2 eq. of diisopropylethylamine. The resulting reaction was allowed to stir overnight at room temperature.

Upon completion, the reaction was washed with 0.5M HCl (2x), sat. NaHCO<sub>3</sub> (2x), and brine (2x) to yield the intermediate amide which was used without further purification. The intermediate amide was dissolved in toluene. 0.2 eq. of TsOH was added and the reaction was refluxed on a Dean-Stark apparatus for 12 hours. Upon reaction completion, the solution was concentration and redissolved in EtOAc where it was washed with sat. NaHCO<sub>3</sub> (2x) and brine (2x). The organic layer was dried and concentrated down to yield crude target compound. The crude material was purified via silica gel chromatography to yield the target molecule.

**Method 3 for the synthesis of 2-(2'-hydroxyphenyl)benzoxazole derivatives:**

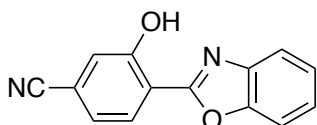


Salicylaldehyde (1.0 eq.) and 2-Aminophenol derivative (1.0 eq.) were combined in a round-bottom flask and dissolved in DMF (0.1 M) at room temperature. Upon the disappearance of starting material, Sodium Cyanide (1.0 eq.) is added and the reaction was run for 18 hours. Upon completion, the reaction was quenched with 1.0 M HCl (10x current volume) and the resulting precipitate was filtered to yield the crude product. The resulting crude solid was purified by silica gel chromatography yield the target compound as a powder.

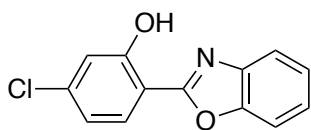


**2-(2-hydroxy-4-nitrophenyl)benzoxazole.** (Method 2, 2.0 mmol scale, XX% yield) <sup>1</sup>H NMR (400 MHz, CDCl<sub>3</sub>) δ. <sup>13</sup>C NMR (125 MHz, CDCl<sub>3</sub>) δ.

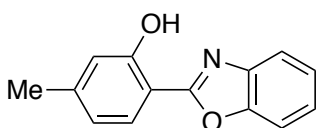




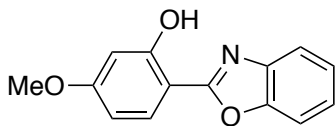
**2-(4-cyano-2-hydroxyphenyl)benzoxazole.** (Method 2, 0.7 mmol scale 12% yield.)  $^1\text{H}$  NMR (400 MHz,  $\text{CDCl}_3$ )  $\delta$  11.60 (s, 1H), 7.93 (d,  $J = 8.5$  Hz, 1H), 7.72 (m, 1H), 7.60 (m, 1H), 7.39 (m, 2H), 7.14 (d,  $J = 2.0$  Hz, 1H), 6.99 (dd,  $J = 8.5, 2.0$  Hz, 1H).  $^{13}\text{C}$  NMR (125 MHz,  $\text{CDCl}_3$ )  $\delta$  162.18, 159.28, 149.06, 139.78, 139.20, 127.93, 125.63, 125.19, 120.21, 119.31, 117.71, 110.71, 109.27, 77.35, 77.03, 76.72.



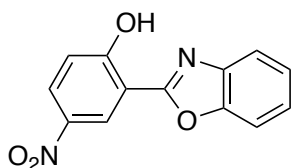
**2-(4-chloro-2-hydroxyphenyl)benzoxazole.** (Method 1, 1.0 mmol scale, 62% yield)  $^1\text{H}$  NMR (400 MHz,  $\text{CDCl}_3$ )  $\delta$  11.63 (s, 1H), 7.93 (d,  $J=8.44$  Hz, 1H), 7.72 (dd,  $J=2.96$  Hz, 3.56 Hz, 1H), 7.60 (dd,  $J=3.92$  Hz, 3.00 Hz, 1H), 7.39 (dd,  $J=3.00$  Hz, 3.68 Hz, 2H), 7.14 (s, 1H), 6.99 (d,  $J=8.40$  Hz, 1H).  $^{13}\text{C}$  (125 MHz,  $\text{CDCl}_3$ )  $\delta$  162.14, 159.25, 149.03, 139.75, 139.17, 127.90, 125.61, 125.17, 120.17, 119.28, 117.68, 110.69, 109.24, 77.36, 77.05, 76.73.



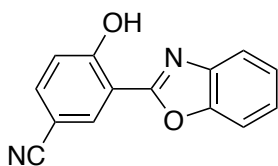
**2-(2-hydroxy-4-methylphenyl)benzoxazole.** (Method 1, 1.0 mmol scale, 45% yield)  $^1\text{H}$  NMR (400 MHz,  $\text{CDCl}_3$ )  $\delta$  11.40 (s, 1H), 7.90 (d,  $J=8.12$  Hz, 1H), 7.71 (dd,  $J=2.48$  Hz, 2.88 Hz, 1H), 7.59 (dd,  $J=2.92$  Hz, 2.68 Hz, 1H), 7.36 (dd,  $J=2.80$  Hz, 2.68 Hz, 2H), 6.94 (s, 1H), 6.83 (d,  $J=8.16$  Hz, 1H), 2.39 (s, 3H).  $^{13}\text{C}$  (125 MHz,  $\text{CDCl}_3$ )  $\delta$  162.07, 159.22, 148.97, 139.71, 139.15, 127.85, 125.62, 125.17, 120.14, 119.26, 117.66, 110.70, 109.18.



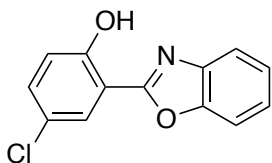
**2-(2-hydroxy-4-methoxyphenyl)benzoxazole.** (Method 2, 0.6 mmol, XX% yield).  $^1\text{H}$  NMR (400 MHz,  $\text{CDCl}_3$ )  $\delta$ .  $^{13}\text{C}$  NMR (125 MHz,  $\text{CDCl}_3$ )  $\delta$ .



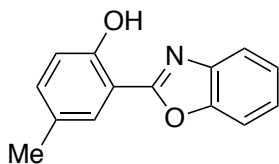
**2-(2-hydroxy-5-nitrophenyl)benzoxazole.** (Method 3, 1.0 mmol, 33% yield).  $^1\text{H}$  NMR (400 MHz,  $\text{CDCl}_3$ )  $\delta$  12.29 (s, 1H), 8.96 (d,  $J = 2.7$  Hz, 1H), 8.31 (dd,  $J = 9.2, 2.8$  Hz, 1H), 7.77 (dd,  $J = 6.4, 2.4$  Hz, 1H), 7.68 (dd,  $J = 6.7, 2.2$  Hz, 1H), 7.45 (m, 2H), 7.20 (d,  $J = 9.2$  Hz, 1H).  $^{13}\text{C}$  NMR (100 MHz,  $\text{CDCl}_3$ )  $\delta$  163.33, 160.86, 149.17, 140.48, 139.26, 128.51, 126.48, 125.62, 123.57, 119.58, 118.22, 111.05, 110.53, 77.32, 77.00, 76.68.



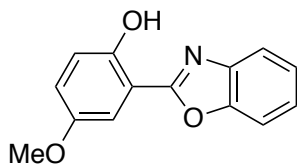
**2-(5-cyano-2-hydroxyphenyl)benzoxazole.** (Method 2, 0.26 mmol, 23% yield)  $^1\text{H}$  NMR (400 MHz,  $\text{CDCl}_3$ )  $\delta$  8.33 (d,  $J = 2.1$  Hz, 1H), 7.78 – 7.72 (m, 1H), 7.66 (ddd,  $J = 9.6, 7.9, 1.8$  Hz, 2H), 7.44 (m, 2H), 7.18 (d,  $J = 8.7$  Hz, 1H).  $^{13}\text{C}$  NMR (100 MHz,  $\text{CDCl}_3$ )  $\delta$  161.64, 160.76, 149.08, 139.30, 136.34, 131.70, 126.32, 125.53, 119.54, 118.74, 118.36, 111.49, 110.94, 103.32, 77.32, 77.00, 76.68.



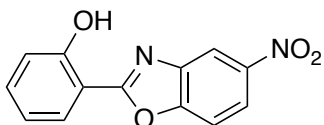
**2-(5-chloro-2-hydroxyphenyl)benzoxazole.** (Method 1, 1.0 mmol, 62% yield)  $^1\text{H}$  NMR (400 MHz,  $\text{CDCl}_3$ )  $\delta$  11.41 (s, 1H), 7.95 (d,  $J = 2.6$  Hz, 1H), 7.74 – 7.67 (m, 1H), 7.60 (m, 1H), 7.40 (m, 2H), 7.35 (dd,  $J = 8.8, 2.6$  Hz, 1H), 7.04 (d,  $J = 8.9$  Hz, 1H).  $^{13}\text{C}$  NMR (100 MHz,  $\text{CDCl}_3$ )  $\delta$  161.64, 157.21, 149.10, 139.75, 133.34, 127.71, 126.35, 125.81, 125.23, 124.42, 119.42, 118.92, 111.50, 110.77, 77.37, 77.06, 76.74, 30.34, 29.74.



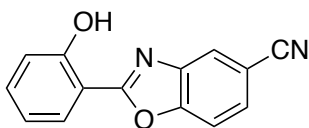
**2-(2-hydroxy-5-methylphenyl)benzoxazole.** (Method 1, 1.0 mmol, XX% yield)  $^1\text{H}$  NMR (400 MHz,  $\text{CDCl}_3$ ) ,  $^{13}\text{C}$  NMR (100 MHz,  $\text{CDCl}_3$ )



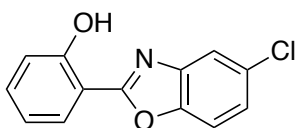
**2-(2-hydroxy-5-methoxyphenyl)benzoxazole.** (Method 2, 1.0 mmol, 16% yield).  $^1\text{H}$  NMR (400 MHz,  $\text{CDCl}_3$ )  $\delta$  11.07 (s, 1H), 7.73 (m, 1H), 7.60 (m, 1H), 7.49 (m, 1H), 7.38 (m, 2H), 7.05 (d,  $J = 1.4$  Hz, 2H), 3.86 (s, 3H).  $^{13}\text{C}$  NMR (100 MHz,  $\text{CDCl}_3$ )  $\delta$  162.76, 153.17, 152.53, 149.11, 140.13, 125.39, 125.02, 121.47, 119.29, 118.43, 110.62, 110.07, 109.66, 77.36, 77.04, 76.72, 55.96.



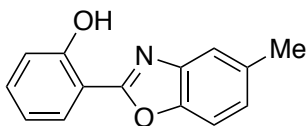
**2-(5-nitrobenzo[d]oxazol-2-yl)phenol.** (Method 3, 1.0 mmol scale, 9% yield).  $^1\text{H}$  NMR (400 MHz,  $\text{CDCl}_3$ )  $\delta$  10.98 (s, 1H), 8.62 (d,  $J=2.20$  Hz, 1H), 8.35 (dd,  $J=2.22$  Hz, 6.72 Hz, 1H), 8.03 (dd,  $J=1.26$  Hz, 6.64 Hz, 1H), 7.72 (d,  $J=8.92$  Hz, 1H), 7.51 (m,  $J=1.34$  Hz, 7.16 Hz, 1H), 7.15 (d,  $J=8.36$  Hz, 1H), 7.05 (t,  $J=7.58$  Hz, 1H).  $^{13}\text{C}$  (100 MHz,  $\text{CDCl}_3$ )  $\delta$  165.79, 159.18, 152.58, 140.62, 134.87, 127.39, 121.40, 119.96, 117.81, 115.41, 110.83, 109.46.



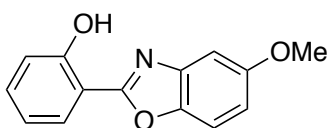
**2-(5-cyanobenzo[d]oxazol-2-yl)phenol.** (Method 3, 1.0 mmol scale, 51% yield).  $^1\text{H}$  NMR (400 MHz,  $\text{CDCl}_3$ )  $\delta$  10.98 (s, 1H), 8.01 (m,  $J=5.20$  Hz, 7.96 Hz, 2H), 7.69 (m,  $J=8.44$  Hz, 3.84 Hz, 8.48 Hz, 2H), 7.50 (m,  $J=8.44$  Hz, 7.24 Hz, 1H), 7.13 (d,  $J=8.36$  Hz, 1H), 7.03 (t,  $J=7.58$  Hz, 1H).  $^{13}\text{C}$  NMR (100 MHz,  $\text{CDCl}_3$ )  $\delta$  165.09, 159.26, 151.59, 140.75, 134.90, 129.59, 127.56, 123.76, 120.09, 118.62, 117.92, 120.08, 109.62, 109.26.



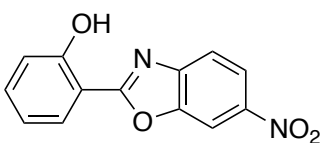
**2-(5-chlorobenzo[d]oxazol-2-yl)phenol.** (Method 3, 1.0 mmol scale, 63% yield).  $^1\text{H}$  NMR (400 MHz,  $\text{CDCl}_3$ )  $\delta$  11.18 (s, 1H), 7.93 (d,  $J=7.88$  Hz, 1H), 7.65 (s, 1H), 7.45 (m,  $J=8.64$  Hz, 2.48 Hz, 2.16 Hz, 7.96 Hz, 8.28 Hz), 7.30 (d,  $J=8.64$  Hz, 1H), 7.09 (d,  $J=8.32$  Hz, 1H), 6.98 (t,  $J=7.24$  Hz, 1H).  $^{13}\text{C}$  NMR (100 MHz,  $\text{CDCl}_3$ )  $\delta$  164.22, 158.93, 147.76, 141.20, 134.14, 130.63, 127.28, 125.72, 119.79, 119.29, 117.65, 111.44, 110.17.



**2-(5-methylbenzo[d]oxazol-2-yl)phenol.** (Method 3, 1.0 mmol scale, 72% yield)  $^1\text{H}$  NMR (400 MHz,  $\text{CDCl}_3$ )  $\delta$  11.50 (s, 1H), 7.95 (d,  $J=7.64$  Hz, 1H), 7.42 (m,  $J=9.44$  Hz, 8.16 Hz, 3H), 7.12 (d,  $J=8.32$  Hz, 2H), 6.98 (m,  $J=7.28$  Hz, 7.56 Hz, 1H), 2.45 (s, 3H).  $^{13}\text{C}$  NMR (100 MHz,  $\text{CDCl}_3$ )  $\delta$  162.93, 158.71, 147.33, 140.13, 134.91, 133.40, 127.06, 126.46, 119.52, 119.16, 117.40, 110.75, 109.99, 21.53.

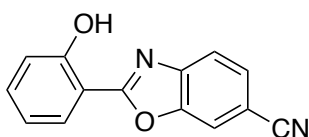


**2-(5-methoxybenzo[d]oxazol-2-yl)phenol.** (Method 3, 3.55 mmol scale, 62% yield).  $^1\text{H}$  NMR (400 MHz,  $\text{CDCl}_3$ )  $\delta$  11.45 (s, 1H), 7.94 (dd,  $J=1.60$  Hz, 6.28 Hz, 1H), 7.41 (m,  $J=3.24$  Hz, 5.68 Hz, 2.72 Hz, 5.52 Hz, 1.72 Hz, 2H), 7.15 (d,  $J=2.48$  Hz, 1H), 7.10 (d,  $J=8.36$  Hz, 1H), 6.98 (t,  $J=7.84$  Hz, 1H), 6.92 (dd,  $J=2.54$  Hz, 6.36 Hz, 1H), 3.84 (s, 3H).  $^{13}\text{C}$  NMR (100 MHz,  $\text{CDCl}_3$ )  $\delta$  163.60, 158.67, 157.70, 143.74, 140.87, 133.49, 127.04, 119.60, 117.45, 113.92, 110.84, 102.20, 56.00.

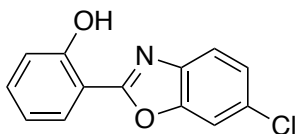


**2-(6-nitrobenzo[d]oxazol-2-yl)phenol.** (Method 3, 1.0 mmol, 15% yield).  $^1\text{H}$  NMR (400 MHz,  $\text{CDCl}_3$ )  $\delta$  11.07 (s, 1H), 8.53 (d,  $J=2.1$  Hz, 1H), 8.37 (dd,  $J=8.8, 2.1$  Hz, 1H), 8.06 (dd,  $J=$

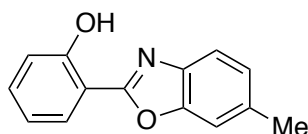
7.9, 1.5 Hz, 1H), 7.83 (d,  $J = 8.8$  Hz, 1H), 7.53 (ddd,  $J = 8.8, 7.4, 1.6$  Hz, 1H), 7.16 (d,  $J = 8.4$  Hz, 1H), 7.10 – 7.02 (m, 1H).  $^{13}\text{C}$  NMR (100 MHz,  $\text{CDCl}_3$ )  $\delta$  167.11, 159.37, 148.37, 145.34, 135.20, 127.69, 121.35, 120.09, 118.99, 117.89, 109.49, 107.31, 77.33, 77.02, 76.70.



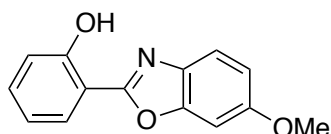
**2-(6-cyanobenzo[d]oxazol-2-yl)phenol.** (Method 3, 1.21 mmol scale, 10% yield).  $^1\text{H}$  NMR (400 MHz,  $\text{CDCl}_3$ )  $\delta$  11.06 (s, 1H), 8.02 (dd,  $J = 7.9, 1.5$  Hz, 1H), 7.91 (s, 1H), 7.80 (d,  $J = 8.2$  Hz, 1H), 7.69 (dd,  $J = 8.2, 1.2$  Hz, 1H), 7.55 – 7.46 (m, 1H), 7.13 (d,  $J = 8.4$  Hz, 1H), 7.04 (t,  $J = 7.6$  Hz, 1H).  $^{13}\text{C}$  NMR (100 MHz,  $\text{CDCl}_3$ )  $\delta$  165.72, 159.25, 148.38, 143.83, 134.92, 129.36, 127.52, 120.06, 119.96, 118.49, 117.77, 114.84, 109.42, 108.46, 77.32, 77.00, 76.68.



**2-(6-chlorobenzo[d]oxazol-2-yl)phenol.** (Method 3, 1.0 mmol scale, 60% yield).  $^1\text{H}$  NMR (400 MHz,  $\text{CDCl}_3$ )  $\delta$  11.76 (s, 1H), 7.92 (d,  $J = 7.84$  Hz, 1H), 7.58 (d,  $J = 8.52$  Hz, 1H), 7.55 (s, 1H), 7.43 (m,  $J = 7.92$  Hz, 7.68 Hz, 1H), 7.32 (d,  $J = 8.48$  Hz, 1H), 7.09 (d,  $J = 8.36$  Hz, 1H), 6.98 (m,  $J = 7.68$  Hz, 7.48 Hz, 1H).  $^{13}\text{C}$  NMR (100 MHz,  $\text{CDCl}_3$ )  $\delta$  163.53, 157.78, 149.33, 138.88, 133.99, 131.07, 127.20, 125.78, 119.76, 117.58, 111.40, 110.19.

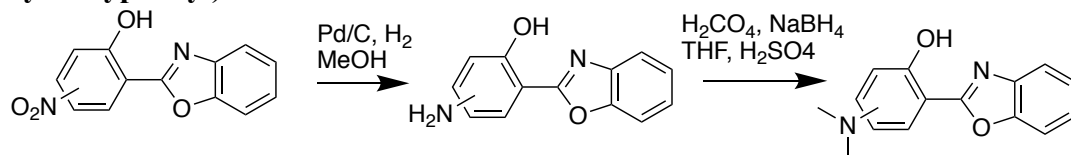


**2-(6-methylbenzo[d]oxazol-2-yl)phenol.** (Method 3, 1.0 mmol scale, 51% yield)  $^1\text{H}$  NMR (400 MHz,  $\text{CDCl}_3$ )  $\delta$  11.49 (s, 1H), 7.95 (dd,  $J=1.32$  Hz, 6.56 Hz, 1H), 7.53 (d,  $J=8.12$  Hz, 1H), 7.42 (m,  $J=1.36$  Hz, 7.12 Hz, 7.12 Hz, 1.36 Hz, 1H), 7.32 (s, 1H), 7.13 (dd,  $J=3.68$  Hz, 4.48 Hz, 2H), 6.99 (t,  $J=7.54$  Hz, 1H), 2.47 (s, 3H).  $^{13}\text{C}$  NMR (100 MHz,  $\text{CDCl}_3$ )  $\delta$  162.36, 158.59, 149.36, 137.78, 135.93, 133.29, 127.00, 126.19, 119.52, 118.55, 117.36, 110.82, 21.85.



**2-(6-methoxybenzo[d]oxazol-2-yl)phenol.** (Method 3, 3.54 mmol scale, 48% yield).  $^1\text{H}$  NMR (400 MHz,  $\text{CDCl}_3$ )  $\delta$  11.32 (s, 1H), 7.83 (d,  $J=7.80$  Hz, 1H), 7.44 (d,  $J=8.72$  Hz, 1H), 7.36 (m,  $J=7.76$  Hz, 8.16 Hz, 1H), 7.08 (d,  $J=8.04$  Hz, 1H), 6.93 (m,  $J=6.20$  Hz, 7.64 Hz, 2H), 6.84 (d,  $J=8.68$  Hz, 1H), 3.76 (s, 3H).  $^{13}\text{C}$  NMR (100 MHz,  $\text{CDCl}_3$ )  $\delta$  161.73, 158.26, 158.08, 149.81, 133.44, 132.85, 126.59, 119.36, 118.95, 117.11, 112.90, 110.67, 95.25, 55.70.

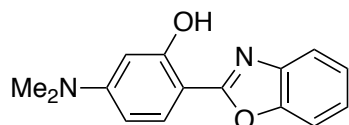
**Procedure for the synthesis of dimethylamino derivatives of 2-(2'-hydroxyphenyl)benzoxazole derivatives:**



1.0 eq. of the nitro 2-(2'-hydroxyphenyl)benzoxazole derivative was placed in a round-bottomed flask and dissolved in methanol (0.1 M). Palladium on Carbon (10 wt.%, 0.1 eq. Pd) was then added and the flask sealed. Hydrogen gas was bubbled through the reaction and held

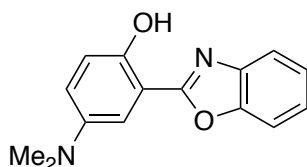
under positive pressure until completion. Upon completion, the reaction was filtered and the resulting filtrate was concentrated under reduced pressure yielding crude amine 2-(2'-hydroxyphenyl)benzoxazole derivative and used without further purification.

A solution of formaldehyde (37% in H<sub>2</sub>O, 14.0 eq. formaldehyde) was added to a flask with a 6 M H<sub>2</sub>SO<sub>4</sub> solution (46.0 eq. H<sub>2</sub>SO<sub>4</sub>) and allowed to stir at 0°C. 1.0 eq. of the amino 2-(2'-hydroxyphenyl)benzoxazole derivative and 5.0 eq. sodium borohydride dissolved in THF (1 M) was slowly added to the flask and the reaction was warmed to room temperature, stirred until disappearance of starting material. Upon completion, the reaction was quenched with H<sub>2</sub>O (~10x reaction volume) and extracted with Ethyl Acetate (3x). The organic phase was concentrated under reduced pressure yielding the crude product. The pure product was the subjected to silica gel chromatography to yield the target compound.

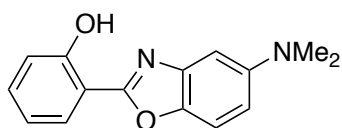


**2-(2-hydroxy-4-dimethylaminophenyl)benzoxazole.** (0.13 mmol, 54% yield). <sup>1</sup>H NMR (400 MHz, CDCl<sub>3</sub>) δ 7.83 (d, *J* = 8.8 Hz, 1H), 7.62 (dd, *J* = 7.36, 1.64 Hz, 1H), 7.53 (dd, *J* = 8.52, 1.36 Hz, 1H), 7.30 (m, 2H), 6.37 (m, 2H). <sup>13</sup>C NMR (100 MHz, CDCl<sub>3</sub>) δ 163.86, 160.22, 154.10, 148.96, 140.59, 128.10, 124.52, 124.02, 118.27, 110.15, 104.71, 99.49, 98.73, 77.35, 77.03, 76.71, 40.20.

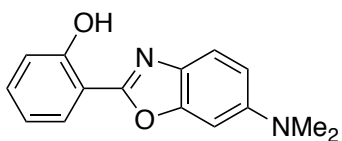




**2-(2-hydroxy-5-dimethylaminophenyl)benzoxazole.** (0.2 mmol, 57% yield).  $^1\text{H}$  NMR (400 MHz,  $\text{CDCl}_3$ )  $\delta$  11.03 (s, 1H), 7.74 (m, 1H), 7.65 (m, 1H), 7.49 (s, 1H), 7.41 (dd,  $J = 6.0, 3.3$  Hz, 2H), 7.10 (s, 2H), 3.00 (s, 6H).  $^{13}\text{C}$  NMR (100MHz,  $\text{CDCl}_3$ )  $\delta$  163.11, 149.14, 140.22, 125.30, 124.97, 121.25, 119.26, 118.11, 110.64, 110.33, 77.34, 77.02, 76.70, 42.29.



**2-(5-dimethylaminobenzo[d]oxazol-2-yl)phenol.** (0.2 mmol, 49% yield).  $^1\text{H}$  NMR (400 MHz,  $\text{CDCl}_3$ )  $\delta$  11.67 (s, 1H), 7.96 (d,  $J = 7.6$  Hz, 1H), 7.40 (m, 2H), 7.14 (d,  $J = 8.3$  Hz, 1H), 6.98 (m, 2H), 6.76 (d,  $J = 9.0$  Hz, 1H), 2.96 (s, 6H).  $^{13}\text{C}$  NMR (100 MHz,  $\text{CDCl}_3$ )  $\delta$  162.74, 158.37, 149.00, 141.71, 140.82, 132.90, 126.72, 119.23, 117.09, 111.67, 110.80, 110.11, 101.61, 41.32.



**2-(6-dimethylaminobenzo[d]oxazol-2-yl)phenol.** (0.15 mmol, 75% yield).  $^1\text{H}$  NMR (400 MHz,  $\text{CDCl}_3$ )  $\delta$  11.54 (s, 1H), 7.94 (d,  $J = 7.8$  Hz, 1H), 7.50 (d,  $J = 8.8$  Hz, 1H), 7.38 (t,  $J = 7.8$  Hz, 1H), 7.12 (d,  $J = 8.3$  Hz, 1H), 6.99 (t,  $J = 7.5$  Hz, 1H), 6.81 (s, 1H), 6.74 (dd,  $J = 8.8, 2.2$  Hz, 1H), 2.99 (s, 6H).  $^{13}\text{C}$  NMR (100 MHz,  $\text{CDCl}_3$ )  $\delta$  160.51, 158.01, 151.01, 149.62, 132.47, 130.67, 126.54, 119.47, 118.95, 117.15, 111.34, 110.95, 93.68, 41.16.

## References

1. Klymchenko, A. S., Solvatochromic and Fluorogenic Dyes as Environment-Sensitive Probes: Design and Biological Applications. *Acc Chem Res* **2017**, *50* (2), 366-375.
2. Loving, G. S.; Sainlos M Fau - Imperiali, B.; Imperiali, B., Monitoring protein interactions and dynamics with solvatochromic fluorophores. (1879-3096 (Electronic)).
3. Santos-Figueroa, L. E.; Moragues, M. E.; Climent, E.; Agostini, A.; Martínez-Máñez, R.; Sancenón, F., Chromogenic and fluorogenic chemosensors and reagents for anions. A comprehensive review of the years 2010–2011. *Chemical Society Reviews* **2013**, *42* (8), 3489-3613.
4. Thooft, A. M.; Cassaidy, K.; VanVeller, B., A Small Push–Pull Fluorophore for Turn-on Fluorescence. *The Journal of Organic Chemistry* **2017**, *82* (17), 8842-8847.
5. Han, J.; Burgess, K., Fluorescent Indicators for Intracellular pH. *Chemical Reviews* **2010**, *110* (5), 2709-2728.
6. Nadler, A.; Schultz, C., The Power of Fluorogenic Probes. *Angewandte Chemie International Edition* **2013**, *52* (9), 2408-2410.
7. Zhu, H.; Fan, J.; Du, J.; Peng, X., Fluorescent Probes for Sensing and Imaging within Specific Cellular Organelles. *Accounts of Chemical Research* **2016**, *49* (10), 2115-2126.
8. Gautier, A.; Tebo, A. G., Fluorogenic Protein-Based Strategies for Detection, Actuation, and Sensing. *Bioessays* **2018**, *40* (10), e1800118.
9. Zhou, P.; Han, K., Unraveling the Detailed Mechanism of Excited-State Proton Transfer. *Acc Chem Res* **2018**, *51* (7), 1681-1690.
10. Sedgwick, A. C.; Wu, L.; Han, H. H.; Bull, S. D.; He, X. P.; James, T. D.; Sessler, J. L.; Tang, B. Z.; Tian, H.; Yoon, J., Excited-state intramolecular proton-transfer (ESIPT) based fluorescence sensors and imaging agents. *Chem Soc Rev* **2018**, *47* (23), 8842-8880.
11. Mishra, V. R.; Ghanavatkar, C. W.; Sekar, N., Towards NIR-Active Hydroxybenzazole (HBX)-Based ESIPT Motifs: A Recent Research Trend. *ChemistrySelect* **2020**, *5* (6), 2103-2113.
12. Zhao, J.; Ji, S.; Chen, Y.; Guo, H.; Yang, P., Excited state intramolecular proton transfer (ESIPT): from principal photophysics to the development of new chromophores and applications in fluorescent molecular probes and luminescent materials. *Physical Chemistry Chemical Physics* **2012**, *14* (25), 8803-8817.

13. Benelhadj, K.; Muzuzu, W.; Massue, J.; Retailleau, P.; Charaf-Eddin, A.; Laurent, A. D.; Jacquemin, D.; Ulrich, G.; Ziessel, R., White emitters by tuning the excited-state intramolecular proton-transfer fluorescence emission in 2-(2'-hydroxybenzofuran)benzoxazole dyes. *Chemistry (Weinheim an der Bergstrasse, Germany)* **2014**, *20* (40), 12843-12857.
14. Meisner, Q. J.; Younes, A. H.; Yuan, Z.; Sreenath, K.; Hurley, J. J. M.; Zhu, L., Excitation-Dependent Multiple Fluorescence of a Substituted 2-(2'-Hydroxyphenyl)benzoxazole. *The Journal of Physical Chemistry A* **2018**, *122* (47), 9209-9223.
15. Barbatti, M.; Aquino, A. J. A.; Lischka, H.; Schrieffer, C.; Lochbrunner, S.; Riedle, E., Ultrafast internal conversion pathway and mechanism in 2-(2'-hydroxyphenyl)benzothiazole: a case study for excited-state intramolecular proton transfer systems. *Physical Chemistry Chemical Physics* **2009**, *11* (9), 1406-1415.
16. Kim, S.; Seo, J.; Park, S. Y., Torsion-induced fluorescence quenching in excited-state intramolecular proton transfer (ESIPT) dyes. *Journal of Photochemistry and Photobiology A: Chemistry* **2007**, *191* (1), 19-24.
17. Grabowski, Z. R.; Rotkiewicz, K.; Rettig, W., Structural Changes Accompanying Intramolecular Electron Transfer: Focus on Twisted Intramolecular Charge-Transfer States and Structures. *Chemical Reviews* **2003**, *103* (10), 3899-4032.
18. Pijeu, S.; Foster, D.; Hohenstein, E. G., Excited-State Dynamics of 2-(2'-Hydroxyphenyl)benzothiazole: Ultrafast Proton Transfer and Internal Conversion. *The Journal of Physical Chemistry A* **2017**, *121* (24), 4595-4605.
19. Mutai, T.; Sawatani, H.; Shida, T.; Shono, H.; Araki, K., Tuning of Excited-State Intramolecular Proton Transfer (ESIPT) Fluorescence of Imidazo[1,2-a]pyridine in Rigid Matrices by Substitution Effect. *The Journal of Organic Chemistry* **2013**, *78* (6), 2482-2489.
20. Shigemitsu, Y.; Mutai, T.; Houjou, H.; Araki, K., Excited-State Intramolecular Proton Transfer (ESIPT) Emission of Hydroxyphenylimidazopyridine: Computational Study on Enhanced and Polymorph-Dependent Luminescence in the Solid State. *The Journal of Physical Chemistry A* **2012**, *116* (49), 12041-12048.
21. Enander, K.; Choulier, L.; Olsson, A. L.; Yushchenko, D. A.; Kanmert, D.; Klymchenko, A. S.; Demchenko, A. P.; Mély, Y.; Altschuh, D., A peptide-based, ratiometric biosensor construct for direct fluorescence detection of a protein analyte. *Bioconjug Chem* **2008**, *19* (9), 1864-70.
22. Kim, T.-I.; Kang, H. J.; Han, G.; Chung, S. J.; Kim, Y., A highly selective fluorescent ESIPT probe for the dual specificity phosphatase MKP-6. *Chemical Communications* **2009**, (39), 5895-5897.

23. Strizhak, A. V.; Postupalenko, V. Y.; Shvadchak, V. V.; Morellet, N.; Guittet, E.; Pivovarenko, V. G.; Klymchenko, A. S.; Mély, Y., Two-color fluorescent l-amino acid mimic of tryptophan for probing peptide-nucleic acid complexes. *Bioconjug Chem* **2012**, *23* (12), 2434-43.
24. Mancini, D. T.; Sen, K.; Barbatti, M.; Thiel, W.; Ramalho, T. C., Excited-State Proton Transfer Can Tune the Color of Protein Fluorescent Markers. *Chemphyschem* **2015**, *16* (16), 3444-9.
25. Chen, L.; Wu, D.; Kim, J.-M.; Yoon, J., An ESIPT-Based Fluorescence Probe for Colorimetric, Ratiometric, and Selective Detection of Phosgene in Solutions and the Gas Phase. *Analytical Chemistry* **2017**, *89* (22), 12596-12601.
26. Lampkin, B. J.; Monteiro, C.; Powers, E. T.; Bouc, P. M.; Kelly, J. W.; VanVeller, B., A designed protein binding-pocket to control excited-state intramolecular proton transfer fluorescence. *Org Biomol Chem* **2019**, *17* (5), 1076-1080.
27. Gutierrez, M.; Alarcos, N.; Liras, M.; Sánchez, F.; Douhal, A., Switching to a Reversible Proton Motion in a Charge-Transferred Dye. *The Journal of Physical Chemistry B* **2015**, *119* (2), 552-562.
28. Wiethaus, G.; Toldo, J. M.; da Silveira Santos, F.; da Costa Duarte, R.; Gonçalves, P. F. B.; Rodembusch, F. S., Experimental and theoretical investigation of long-wavelength fluorescence emission in push-pull benzazoles: intramolecular proton transfer or charge transfer in the excited state? *Phys Chem Chem Phys* **2019**, *21* (8), 4408-4420.
29. Alarcos, N.; Gutierrez, M.; Liras, M.; Sanchez, F.; Douhal, A., An abnormally slow proton transfer reaction in a simple HBO derivative due to ultrafast intramolecular-charge transfer events. *Physical Chemistry Chemical Physics* **2015**, *17* (25), 16257-16269.
30. Alarcos, N.; Gutierrez, M.; Liras, M.; Sanchez, F.; Moreno, M.; Douhal, A., Direct observation of breaking of the intramolecular H-bond, and slowing down of the proton motion and tuning its mechanism in an HBO derivative. *Physical Chemistry Chemical Physics* **2015**, *17* (22), 14569-14581.
31. Azarias, C.; Budzak, S.; Laurent, A. D.; Ulrich, G.; Jacquemin, D., Tuning ESIPT fluorophores into dual emitters. *Chem Sci* **2016**, *7* (6), 3763-3774.
32. Hsieh, C.-C.; Jiang, C.-M.; Chou, P.-T., Recent Experimental Advances on Excited-State Intramolecular Proton Coupled Electron Transfer Reaction. *Accounts of Chemical Research* **2010**, *43* (10), 1364-1374.
33. Hammes-Schiffer, S.; Stuchebrukhov, A. A., Theory of Coupled Electron and Proton Transfer Reactions. *Chemical Reviews* **2010**, *110* (12), 6939-6960.
34. Zgierski, M. Z.; Fujiwara, T.; Lim, E. C., Coupled Electron and Proton Transfer Processes in 4-Dimethylamino-2-hydroxy-benzaldehyde. *The Journal of Physical Chemistry A* **2011**, *115* (35), 10009-10017.

35. Seo, J.; Kim, S.; Park, S. Y., Strong solvatochromic fluorescence from the intramolecular charge-transfer state created by excited-state intramolecular proton transfer. *J Am Chem Soc* **2004**, *126* (36), 11154-5.
36. Klymchenko, A. S.; Demchenko, A. P., Multiparametric probing of intermolecular interactions with fluorescent dye exhibiting excited state intramolecular proton transfer. *Physical Chemistry Chemical Physics* **2003**, *5* (3), 461-468.
37. Klymchenko, A. S.; Mely, Y., Fluorescent environment-sensitive dyes as reporters of biomolecular interactions. *Prog Mol Biol Transl Sci* **2013**, *113*, 35-58.
38. Mena, L. D.; Vera, D. M. A.; Baumgartner, M. T.; Jimenez, L. B., Adiabatic deprotonation as an important competing pathway to ESIPT in photoacidic 2-phenylphenols. *Physical Chemistry Chemical Physics* **2019**, *21* (23), 12231-12240.
39. Houari, Y.; Charaf-Eddin, A.; Laurent, A. D.; Massue, J.; Ziessel, R.; Ulrich, G.; Jacquemin, D., Modeling optical signatures and excited-state reactivities of substituted hydroxyphenylbenzoxazole (HBO) ESIPT dyes. *Physical Chemistry Chemical Physics* **2014**, *16* (4), 1319-1321.
40. Lavis, L. D.; Raines, R. T., Bright building blocks for chemical biology. *ACS Chem Biol* **2014**, *9* (4), 855-66.
41. Lampkin, B. J. a. N. Y. H. a. K. P. B. a. V. B., Demonstration of Baird's rule complementarity in the singlet state with implications for excited-state intramolecular proton transfer. *Physical Chemistry Chemical Physics* **2019**, *21* (22), 11608--11614.
42. Rurack, K.; Spieles, M., Fluorescence Quantum Yields of a Series of Red and Near-Infrared Dyes Emitting at 600–1000 nm. *Analytical Chemistry* **2011**, *83* (4), 1232-1242.
43. Stasyuk, A. J.; Banasiewicz, M.; Cyrański, M. K.; Gryko, D. T., Imidazo[1,2-a]pyridines susceptible to excited state intramolecular proton transfer: one-pot synthesis via an Ortoleva-King reaction. *J Org Chem* **2012**, *77* (13), 5552-8.
44. Zhao, H.; Dietrich, J., Privileged scaffolds in lead generation. *Expert Opin Drug Discov* **2015**, *10* (7), 781-90.
45. Xue, C.; Lin, T. Y.; Chang, D.; Guo, Z., Thioflavin T as an amyloid dye: fibril quantification, optimal concentration and effect on aggregation. *R Soc Open Sci* **2017**, *4* (1), 160696.
46. Connelly, S.; Mortenson, D. E.; Choi, S.; Wilson, I. A.; Powers, E. T.; Kelly, J. W.; Johnson, S. M., Semi-quantitative models for identifying potent and selective transthyretin amyloidogenesis inhibitors. *Bioorg Med Chem Lett* **2017**, *27* (15), 3441-3449.

47. Bulawa, C. E.; Connelly, S.; Devit, M.; Wang, L.; Weigel, C.; Fleming, J. A.; Packman, J.; Powers, E. T.; Wiseman, R. L.; Foss, T. R.; Wilson, I. A.; Kelly, J. W.; Labaudinière, R., Tafamidis, a potent and selective transthyretin kinetic stabilizer that inhibits the amyloid cascade. *Proc Natl Acad Sci U S A* **2012**, *109* (24), 9629-34.
48. Albert, M. B., Standards for photoluminescence quantum yield measurements in solution (IUPAC Technical Report). *Pure and Applied Chemistry* **2011**, *83* (12), 2213-2228.

**CHAPTER 4. DEMONSTRATION OF BAIRD'S RULE COMPLEMENTARITY IN THE SINGLET STATE WITH IMPLICATIONS FOR EXCITED-STATE INTRAMOLECULAR PROTON TRANSFER**

Bryan J. Lampkin, ‡<sup>a</sup> Yen H. Nguyen, ‡<sup>a</sup> Peter B. Karadakov,<sup>b</sup> and Brett VanVeller,<sup>\*a</sup>

<sup>a</sup> Department of Chemistry, Iowa State University, Ames, Iowa, 50011, USA

<sup>b</sup> Department of Chemistry, University of York, Heslington, York YO10 5DD, UK

‡ These authors contributed equally to this manuscript

Modified from a manuscript published in *Physical Chemistry Chemical Physics*, **2019**,  
21, 11608-11614

Copyright © 2019 Royal Society of Chemistry

**Abstract**

The aromatic character of an arene is proposed to switch from aromatic in the ground state ( $S_0$ ) to antiaromatic in the  $S_1$  and  $T_1$  excited states. This behavior is known as Baird's rule and has been invoked to explain excited-state properties, primarily in the triplet state, whereas rationalization of antiaromaticity in the singlet state is less developed. This work demonstrates the first application of Baird's rule to rationalize previously unexplained experimental behavior of the singlet state process known as excited-state intramolecular proton transfer (ESIPT). Further, by analyzing the variations in isotropic magnetic shielding around the base arenes (benzene and naphthalene) of ESIPT fluorophores in the  $S_0$  and  $S_1$  electronic states, different shielding distributions indicate a complementarity to Baird's rule: greater aromaticity in  $S_0$  leads to greater antiaromaticity in  $S_1$  and *vice versa*. These findings have immediate application in the design of functional ESIPT fluorophores and, more generally, for photochemical reactions that are driven by the relief of antiaromaticity in the excited state. Notably, a tenet of traditional chromophore design states that expansion of conjugation generally leads to a red-shift

absorbance and emission wavelengths. The results of this study show that ESIPT fluorophores run contrary to those conventional design principles and this behavior can only be rationalized by considering Baird's rule.

## Introduction

Aromaticity plays a major role in the chemical and electronic properties of molecules in the ground state following Hückel's rules.<sup>1-3</sup> Alternatively, the concepts of aromaticity and antiaromaticity have also been shown to influence the properties of singlet and triplet excited states. In general, an annulene with  $[4n + 2]$   $\pi$ -electrons in its aromatic ground state ( $S_0$ ) can be regarded as antiaromatic in its  $S_1$  and  $T_1$  excited states. The converse is similarly true for annulenes with a  $4n$   $\pi$ -electron antiaromatic ground states possessing aromatic character in the excited state.<sup>4-9</sup> This inversion of aromaticity between the ground and excited states has colloquially come to be known as *Baird's rule*.<sup>10, 11</sup> Baird originally proposed the inversion of Hückel's rules between  $S_0$  and  $T_1$ ,<sup>4</sup> but subsequent theoretical work suggested Baird's rule to be applicable to  $S_1$  states as well.<sup>12-15</sup> While numerous studies<sup>10</sup> have been conducted to investigate the excited-state aromaticity of various annulenes—establishing Baird's rule as a useful convention for understanding electronic states—the application of excited-state aromaticity to rationalize and design photochemical properties is less developed and predominantly focused on triplet aromaticity.<sup>16-19</sup>

The goal of this work was to apply Baird's rules to interpret the unconventional behavior of benzoxazole fluorophores that undergo excited-state intramolecular proton transfer (ESIPT), where traditional strategies to red-shift the fluorescent wavelength instead lead to blue-shifted emission.<sup>20, 21</sup> In doing so, we demonstrate the complementarity of Baird's rule, where lower aromaticity in  $S_0$  leads to lower antiaromaticity in  $S_1$ . These results provide a deeper



understanding of excited-state potential energy surfaces for applications in the design of functional chromophores and photochemical pathways.

Excited-state intramolecular proton transfer (ESIPT) is a photo-chemical process that leads to a dramatically large Stokes shift of the wavelength of fluorescence.<sup>20</sup> Briefly, the 2-(2-hydroxyphenyl)-benzoxazole derivative (Figure 4.1) exists in its phenolic enol form **E** in the ground state. After excitation of **E**, direct fluorescence from **E\*** can produce an emitted photon with a relatively small Stokes shift. Alternatively, the structure of **E\*** is such that an excited-state tautomerization can occur to produce the keto form **K\*** (Figure 4.1, ESIPT step). The isomerization from **E\*** to **K\*** is fast ( $\sim$ ps) and highly favorable. Emission then takes place from **K\*** to the ground-state keto form **K**—where the quinoidal character of **K** places it higher in energy in the ground state than **E** (an example of Hückel  $[4n + 2]$  aromatic stability). The net result is that a stabilized **K\*** and destabilized **K** closes the energy gap ( $S_1' - S_0'$ ) such that fluorescence from **K\*** can be 4150 nm red-shifted relative to fluorescence from **E\*** ( $S_1 - S_0$ ).

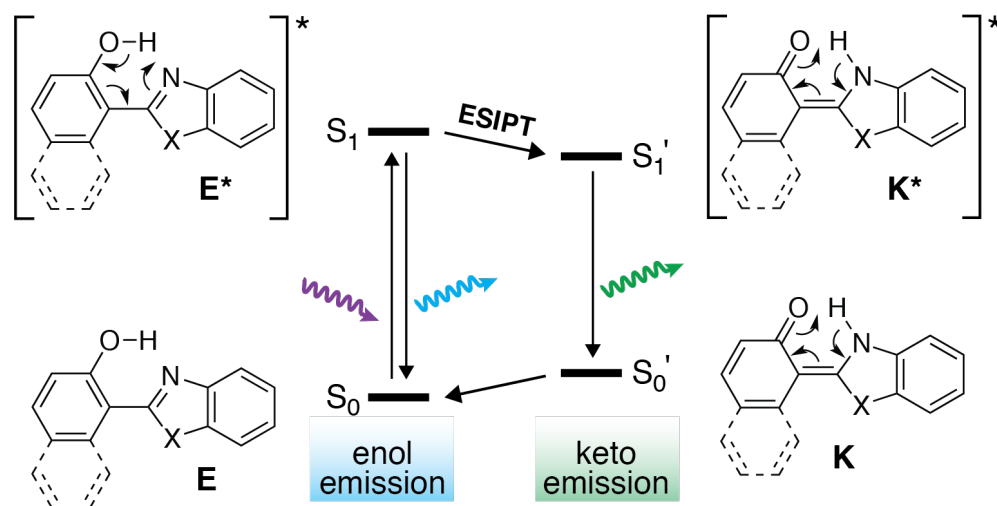


Figure 4.1 Excited-State Intramolecular Proton Transfer (ESIPT). Isomerization to the keto form closes the energy gap, red-shifts emission and creates a large Stokes shift.

The ESIPT process has been applied to the design of new functional molecules for biosensing and imaging.<sup>20,21</sup> Thus, insights into the factors that govern the isomerization and wavelength of emission are immensely valuable to the design and optimization of novel chemical tools based on ESIPT. While the excited-state behavior of derivatives based on **E** has been extensively studied, one aspect of their emissive behavior has eluded explanation.<sup>22-24</sup>

Consider the behavior of two benzoxazole derivatives **HBO** and **NAP** (Figure 4.2 and Table 4.1). In general, expansion of conjugation leads to a red-shift in the absorption and emission of a chromophore. Accordingly, the absorbance maximum of **NAP** is  $\sim 40$  nm longer than **HBO**. In contrast, however, the emission wavelength of **NAP** is not similarly red-shifted and the Stokes shift is far smaller than for **HBO**. The origins of this odd behavior have not been adequately explained.<sup>22-24</sup> Additionally, for **NAP**, two emissive bands are observed. The predominant band is ascribed to emission from **NAP-K\*** (460 nm) with a weaker, poorly defined band from **NAP-E\*** (400 nm).<sup>22</sup>

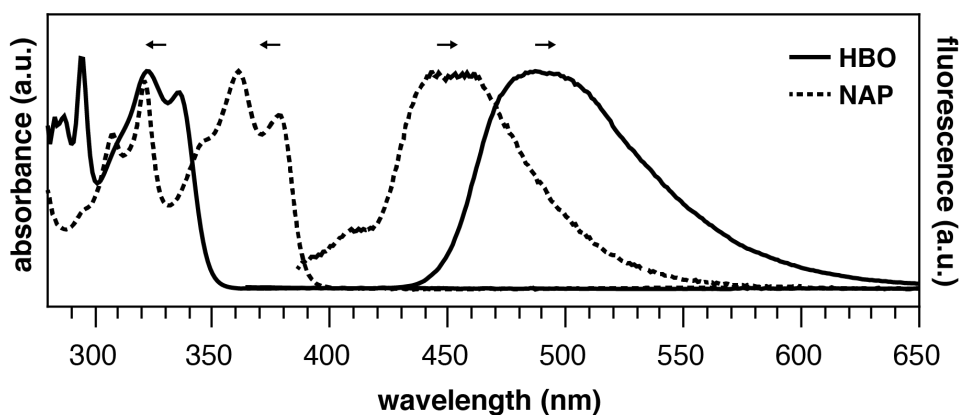


Figure 4.2 Absorbance and emission traces of HBO (solid) and Nap (dashed) in toluene.

Table 4.1 Spectral data of ESIPT fluorophores in Toluene

	Abs $\lambda_{\max}$ (nm)	Em $\lambda_{\max}$ (nm)	Stokes Shift $\lambda_{\max}$ (nm)
	335	508	173
	278	400, 460	22, 82

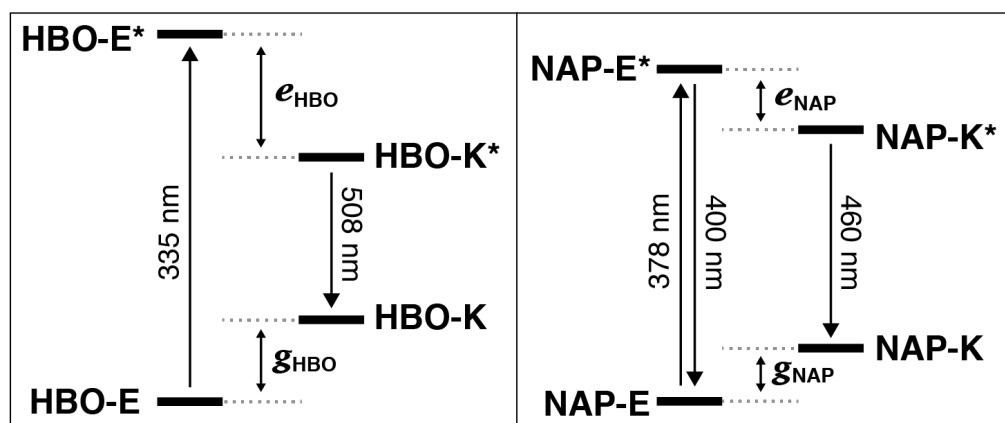


Figure 4.3 Excited-state intramolecular proton transfer (ESIPT). Isomerization to the keto form closes the energy gap, red-shifts emission and creates a large Stokes shift.

From the spectral data of **HBO** and **NAP** in Table 1, we can develop the potential energy diagrams in Figure 4.3.<sup>23</sup> Based on the higher energy of emission from **NAP-K\*** (460 nm) versus **HBO-K\*** (508 nm), **HBO-K\*** is more stabilized relative to **HBO-E\*** than for **NAP-K\*** relative to **NAP-E\*** ( $e_{\text{HBO}} > e_{\text{NAP}}$ ). Similarly, the smaller energy difference between **NAP-E\*** and **NAP-K\*** ( $e_{\text{NAP}}$ ) means that a detectable amount of **NAP-E\*** exists and a minor band for enol emission is observed.<sup>25</sup> Overall, these results are congruent with the notion that tautomerization of **NAP-E\*** to **NAP-K\*** is not as energetically stabilizing as tautomerization of **HBO-E\*** to **HBO-K\***

despite the larger conjugated system in **NAP**. Given the utility of ESIPT probes for a variety of sensing and imaging applications,<sup>20, 21</sup> it is essential to understand the factors that contribute to the photochemical mechanism to establish reliable design criteria.

It has been proposed theoretically that aromaticity may play a role in the tautomeric proton transfer of phenolic derivatives in the excited state.<sup>26, 27</sup> Similarly, according to Baird's rule, the aromatic phenol (**E**) is antiaromatic in the excited state, and isomerization to the quinoidal keto form (**K**) can be conceptually understood to relieve the destabilizing effects of antiaromaticity.

Naphthalene is generally understood to be less aromatic than benzene in the ground state.<sup>28-31</sup> We therefore propose that naphthalene is less antiaromatic than benzene in the excited state. This complementarity of greater aromaticity in the ground state leading to greater antiaromaticity in the excited state (and vice versa) is an aspect of Baird's rule that has not been experimentally demonstrated.

Thus, **NAP-E\*** is less antiaromatic relative to **HBO-E\***, which creates a lower driving force to form **NAP-K\***. Consequently, **NAP-K\*** is less stabilized in the excited state and a larger energy gap must exist between **NAP-K\*** and **NAP-K** relative to the energy gap between **HBO-K\*** and **HBO-K**. As an aside, the reduced Stokes shift of **NAP** likely also derives from the lower energetic bias between the enol and keto tautomers in the ground state ( $g_{\text{HBO}}$  and  $g_{\text{NAP}}$ , Figure 4.3). The lower ground-state aromaticity of naphthalene versus benzene means that  $g_{\text{HBO}} > g_{\text{NAP}}$ . Thus, because **NAP-K** is not as destabilized relative to **NAP-E** due to this reduced aromaticity, the energy gap between **NAP-K** and **NAP-K\*** is necessarily larger than for **HBO**.

## Results and Discussion

The proposed role that the reduced excited-state antiaromaticity of naphthalene plays in the photophysics of **NAP** is supported by calculations off-nucleus isotropic magnetic shielding isosurfaces of benzene and naphthalene in the ground and excited state (Figure 4.4-Figure 4.6). The comparison of ground and excited-state aromaticity is well-served by this computational approach<sup>15</sup> because the off-nucleus magnetic isotropic shielding, displayed as a function of position in the contour plots of Figure 4.4-Figure 4.6, addresses important drawbacks associated with single-point nucleus-independent chemical shift (NICS) values.<sup>32</sup> Mainly, the arbitrary position at which a single-point NICS value is calculated may not possess sufficient information to fully characterize the aromaticity of a  $\pi$ -system.<sup>33, 34</sup> Additionally, geometric indices of aromaticity are often not applicable for excited-state aromaticity. For example, bond-length alternation is often invoked as an indication of reduced aromaticity in the ground state,<sup>35</sup> but benzene maintains the same  $D_{6h}$  symmetry across  $S_0$  and  $S_1$ .<sup>36-38</sup> Thus, off-nucleus isotropic magnetic shielding isosurfaces provide one of the most insightful and succinct means of comparing aromaticity between molecules.

The contour plots in Figure 4.4-Figure 4.6 display the spatial variation in the values of the off-nucleus isotropic magnetic shielding,  $\sigma_{\text{iso}}(\mathbf{r})$ . The shape of the isotropic shielding surfaces and contour plots in Figure 4.4-Figure 4.6 show profoundly different isotropic shielding distributions between the  $S_0$  and  $S_1$  of both benzene and naphthalene, where positive  $\sigma_{\text{iso}}(\mathbf{r})$  values indicate more shielded regions that can be associated with stronger bonding (aromatic) and negative  $\sigma_{\text{iso}}(\mathbf{r})$  values indicate more deshielded regions corresponding to weaker bonding (antiaromatic). Such contour plots have been referred to as “fingerprints” of aromaticity that

allow for unambiguous classification of the degree of aromaticity and antiaromaticity in the electronic states of benzene and naphthalene.<sup>15</sup>

The isotropic shielding is represented by three plotting plane orientations (Scheme 4.1) to provide a more comprehensive picture of the spatial variation of  $\sigma_{\text{iso}}(\mathbf{r})$ .

In general, the contour plots in Figure 4.4-Figure 4.6 reveal

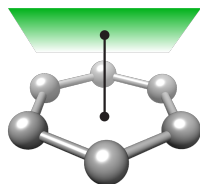


**Figure 4**  
1 Å above  
molecular plane

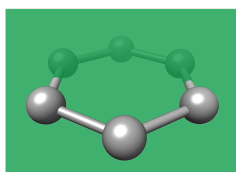


**Figure 5**  
vertical slice  
through C–C bonds

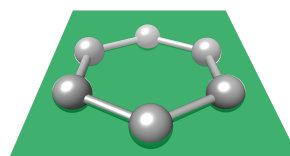


**Figure 6**  
horizontal slice  
through molecular plane

Scheme 4.1 Planes of contour plots in Figure 4.4-Figure 4.6

al that benzene is more aromatic relative to the benzene moiety in naphthalene in the ground state and, conversely, benzene is more antiaromatic relative to benzene moiety in naphthalene in the excited state.

The  $S_0$  of benzene in Figure 4.4 displays a shielded ring inside of which the isotropic shielding,  $\sigma_{\text{iso}}(\mathbf{r})$ , is above 15 ppm. In contrast, the regions where  $\sigma_{\text{iso}}(\mathbf{r})$  exceeds 15 ppm in each of the six-membered rings in  $S_0$  of naphthalene are smaller and discontinuous, indicating a lower aromaticity compared with  $S_0$  of benzene. The  $S_1$  contour plots reveal a complimentary relationship to the aromaticity in  $S_0$ . The  $S_1$  of benzene shows  $\sigma_{\text{iso}}(\mathbf{r})$  going down to under  $-30$  ppm in a sizeable central circular region, which indicates that it is more antiaromatic than  $S_1$  of naphthalene where the contour line surrounding the corresponding deshielded regions has  $\sigma_{\text{iso}}(\mathbf{r})$  of  $-25$  ppm.

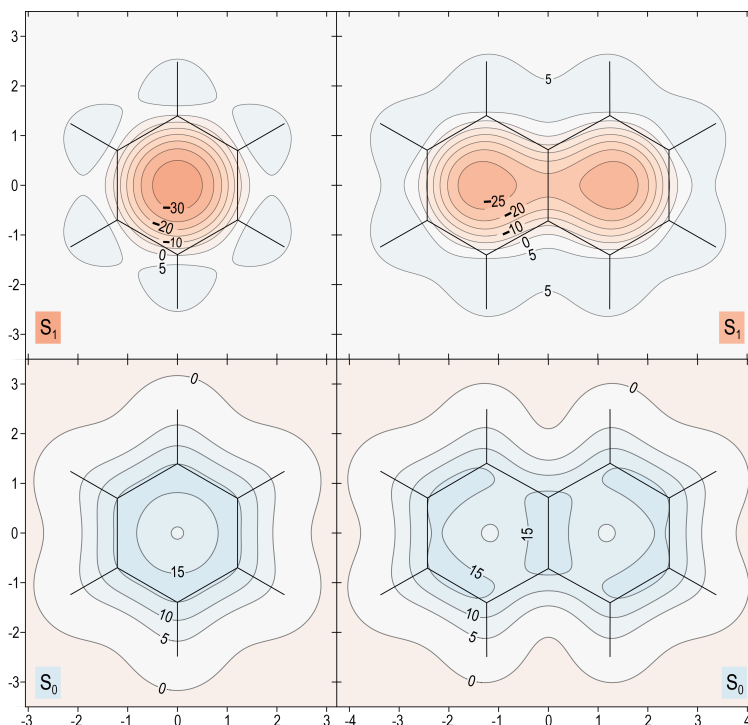


Figure 4.4 Isotropic shielding contour plots 1 Å above the molecular (horizontal) plane for the the  $S_0$  and  $S_1$  states of benzene (left) and naphthalene (right).  $\sigma_{\text{iso}}(\mathbf{r})$  values were obtained using state-optimized  $\pi$ -space CASSCF(6,6)-GIAO/6-311+G\* and CASSCF(10,10)-GIAO/6-311+G\* wavefunctions for benzene and naphthalene respectively,  $\sigma_{\text{iso}}(\mathbf{r})$  in ppm, axes in Å.

The spatial variation of  $\sigma_{\text{iso}}(\mathbf{r})$  represented in Figure 4.5 reinforces the conclusions from Fig. 4. The areas of strong bonding exhibiting  $\sigma_{\text{iso}}(\mathbf{r})$  over 40 ppm, are larger in the  $S_0$  of benzene than for naphthalene (see inset). Here we have another confirmation that the greater aromaticity of benzene in  $S_0$  leads to greater antiaromaticity in  $S_1$  compared with naphthalene: The most deshielded region extending above and below the central parts of the benzene ring features  $\sigma_{\text{iso}}(\mathbf{r})$  below  $-40$  ppm whereas the corresponding regions in naphthalene are less deshielded by about 5 ppm.

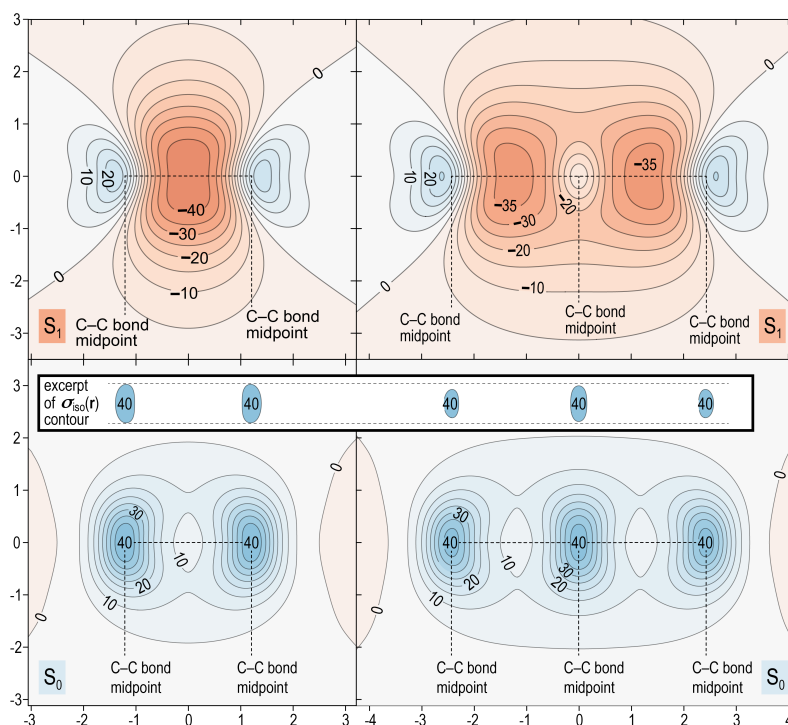


Figure 4.5 Isotropic shielding contour plots in the vertical plane slicing through the C-C bonds for the  $S_0$  and  $S_1$  states of benzene (left) and naphthalene (right). Same wavefunctions as for Figure 4.4,  $\sigma_{\text{iso}}(\mathbf{r})$  in ppm, axes in Å.

The in-plane variation in  $\sigma_{\text{iso}}(\mathbf{r})$  represented in Figure 4.6 is less indicative of differences in aromaticity in  $S_0$ . We do note, however, that the area where  $\sigma_{\text{iso}}(\mathbf{r})$  falls to under 10 ppm at the center of each ring is smaller for benzene than for naphthalene, which shows that benzene possesses higher values of  $\sigma_{\text{iso}}(\mathbf{r})$  overall compared with naphthalene. The  $S_1$  contour plots reinforce the observations made in relation to Figure 4.5: the central region of the benzene ring features more extensive deshielding than the central regions of the six-membered rings in naphthalene, which is an indication of greater antiaromaticity.

Finally, we introduce a new “fingerprint” of aromaticity switching in Figure 4.7, which displays the difference contour plots that result from subtracting  $\sigma_{\text{iso}}(\mathbf{r})$  for  $S_0$  from  $\sigma_{\text{iso}}(\mathbf{r})$  for  $S_1$ . Figure 4.7 confirms that the overall change in aromatic character from ground to excited state is greater for benzene than for naphthalene by 4-7 ppm.



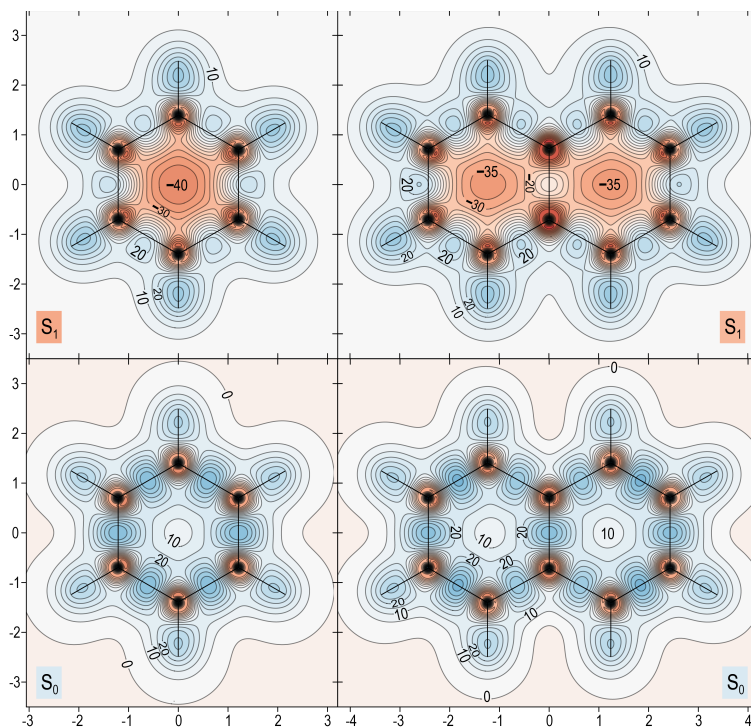


Figure 4.6 Isotropic shielding contour plots in the molecular (horizontal) plane for the  $S_0$  and  $S_1$  states of benzene (left) and naphthalene (right). Same wavefunctions as for Figure 4.4,  $\sigma_{\text{iso}}(\mathbf{r})$  in ppm, axes in Å.

The overall conclusion from all of the contour plots is that differences in aromaticity and bonding between benzene and naphthalene are smaller in  $S_0$  relative to  $S_1$ . Indeed, differences in ground-state aromaticity are small (these are more obvious in the  $S_0$  shielding plots 1 Å above the molecular plane, see Figure 4.4, whereas the  $S_0$  shielding plots in Figure 4.5 and Figure 4.6 display very similar bonding patterns). This finding, albeit based on a single comparative example, may imply that small differences in ground state aromaticity can lead to much larger differences in antiaromaticity in the excited state.

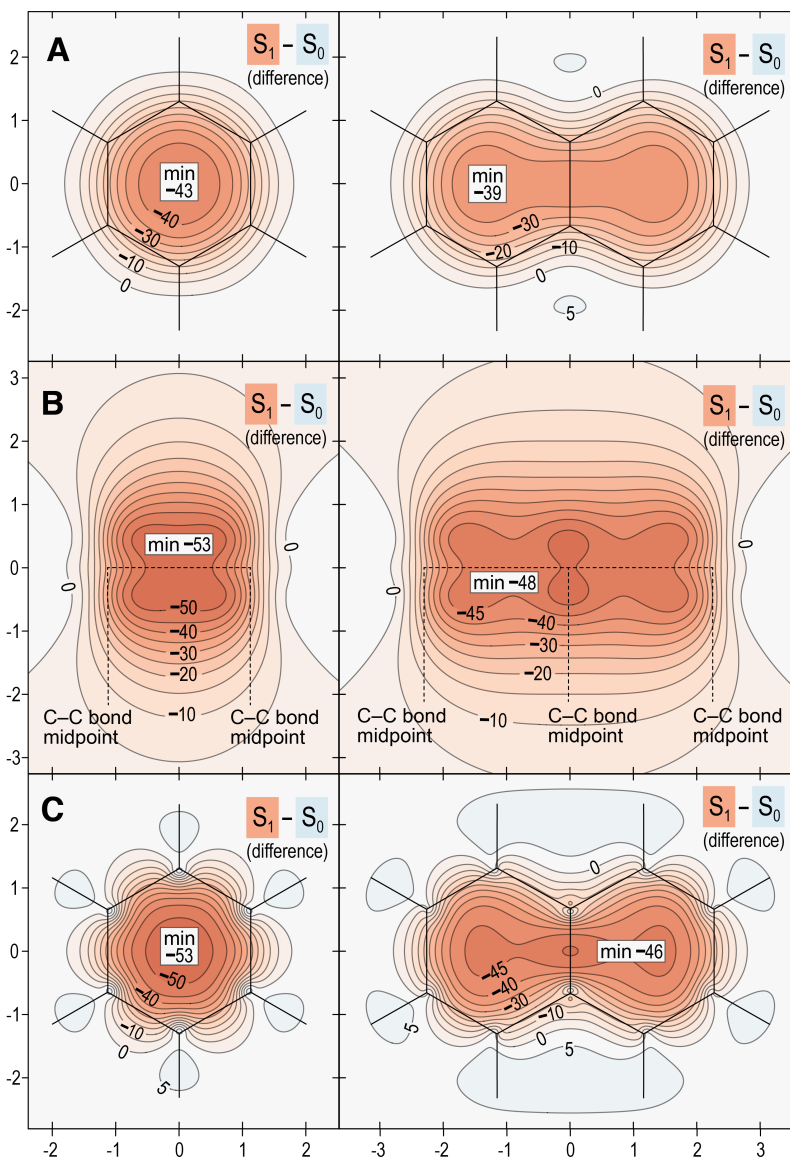


Figure 4.7 Isotropic shielding difference plots between  $S_1$ - $S_0$  for benzene (left) and naphthalene (right) in three orientations described by Scheme 4.1: (A) same as for Figure 4.4; (B) same as for Figure 4.5; (C) same as for Figure 4.6. Same wavefunctions as for Figure 4.4,  $\sigma_{\text{iso}}(\mathbf{r})$  in ppm, axes in Å.

Collectively, these results affirm the greater aromaticity of benzene compared with naphthalene in  $S_0$ .<sup>28-31</sup> Conversely, benzene is more antiaromatic in  $S_1$  than naphthalene. Therefore, the greater aromaticity of benzene in  $S_0$  similarly leads to greater antiaromaticity in  $S_1$  relative to naphthalene ( $\Delta\sigma_{\text{iso}}(\mathbf{r})$  of about  $-5$  ppm). These results demonstrate that, when applied

to singlet states, Baird's rule is complimentary between  $S_0$  and  $S_1$ , where greater aromaticity in  $S_0$  leads to greater antiaromaticity in  $S_1$ . The implications of this observation build a compelling case for the role that aromaticity effects play in the ESIPT process of **HBO** and **NAP**.

The greater antiaromaticity in the phenol of **HBO-E\*** creates a larger energetic difference between **HBO-E\*** and the quinoidal **HBO-K\*** (which could be considered nominally nonaromatic by Hückel's rules). In contrast, the reduced antiaromaticity of **NAP-E\*** relative to **HBO-E\*** creates a smaller energetic driving force to form **NAP-K\***. We therefore propose that these aromaticity effects are responsible for the reduced Stoke's shift for **NAP**. Similarly, the smaller energetic bias between **NAP-E\*** and **NAP-K\*** means that enol emission from **NAP-E\*** can be detected relative to keto emission.

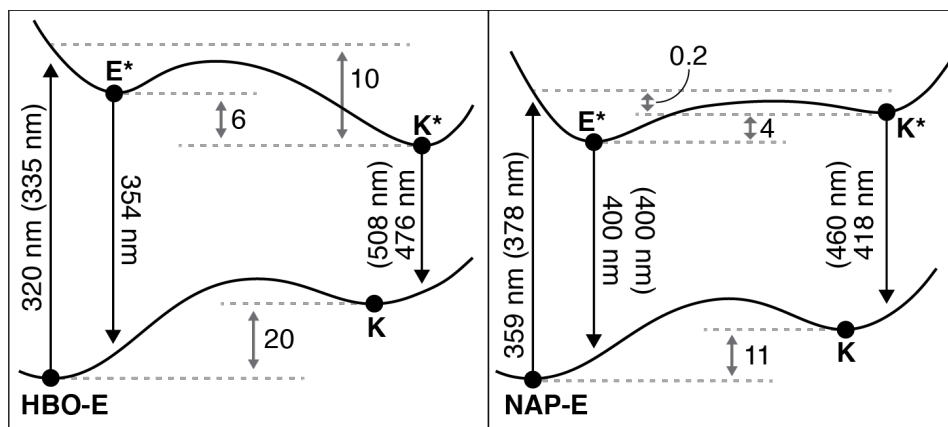


Figure 4.8 Computed TD-DFT potential energy diagram for HBO and NAP (at the TD-DFT B3LYP/6-311+G(d,p) level). all vertical transitions are reported in nm with experimentally determined values from Table 4.1 provided in parentheses. Adiabatic energy differences reported in kcal mol<sup>-1</sup>.

Finally, we note that Baird's rules of excited-state aromaticity have primarily been validated in arenes with  $(\pi, \pi^*)$  excited states.<sup>10</sup> The ESIPT process similarly occurs in the  $(\pi, \pi^*)$  excited state,<sup>24</sup> which justifies our application of Baird's rule to explain the behavior of **NAP**.

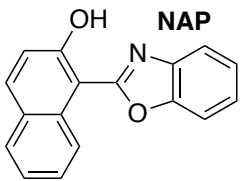
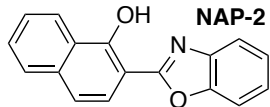
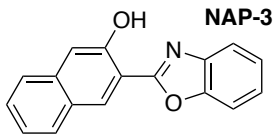
The potential energy diagrams in Figure 4.3 were constructed based on the observable spectral properties of **HBO** and **NAP**. To gain further insight into the ESIPT process, we calculated the energetic parameters defined in Figure 4.8.

The computed wavelengths of absorption and emission correspond to the Frank-Condon vertical transitions from the ground state and the optimized excited state geometry for both **HBO** and **NAP**. All electronic energies were normalized to the ground state energy of the enol form (**E**) for both **HBO** and **NAP**. As anticipated, based on the lower aromaticity of naphthalene versus benzene discussed above, there is a smaller energy difference between the **E** and **K** species of **NAP** relative to **HBO**.

Alternatively, in the excited state, the analysis in Figure 4.4-Figure 4.7 predict a greater stabilization of **HBO-K\*** compared with **HBO-E\***, in accord with Baird's rule. Indeed, we compute a favorable stabilization (6 kcal/mol) of **HBO-K\*** following ESIPT, whereas the energetic stabilization of **NAP-K\*** was computed to be energetically uphill (4 kcal/mol) relative to **NAP-E\***. The spontaneous formation of **NAP-K\*** has been spectroscopically confirmed,<sup>22</sup> implying an exothermic ESIPT process to form **NAP-K\***. We therefore conclude that our computed endothermic process likely arises from error associated with excited-state geometry optimization of **K\***. TD-DFT geometry optimizations have been characterized to significantly underestimate CO bond lengths and as a result, will give inaccurate emission energies.<sup>39, 40</sup> Nevertheless, the reported gas phase transition energies (in nm) match experimental observables within documented TD-DFT errors (0.2–0.3 eV),<sup>41</sup> where emission from **NAP-K\*** shows the most inaccurate computed value (418 nm) relative to experiment (460 nm). This inaccuracy further suggests that an error in the computed geometry is responsible for the discrepancy in energy between theory and experiment of **NAP-E\*** and **NAP-K\***.

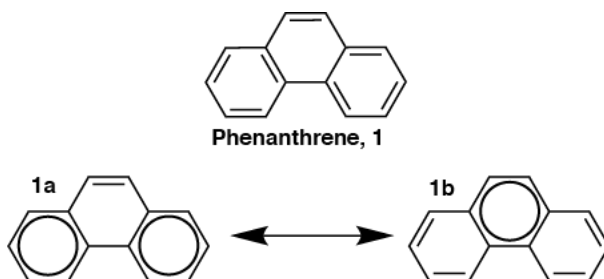
To further exemplify Baird's rule complementarity and how this generalization can be leveraged towards photochemical design, we examined the ESIPT properties of the 2-(hydroxynaphthyl)-benzoxazole family. While this family of ESIPT dyes have been studied in the past,<sup>22-24</sup> an explanation for their varying photophysical properties is lacking. The only difference between **NAP**, **NAP-2**, and **NAP-3** is their substitution pattern of the hydroxyl and benzoxazole functional groups. Therefore, with respect to the aromaticity of these three molecules governing their emissive properties, we'd expect to obtain similar results. However, the Stokes shift for **NAP-3** is significantly larger than that for **NAP** and **NAP-2** (Table 4.2). This indicates, qualitatively at least, that either the excited-state energy of **E\*** is higher or the excited-state energy of **K\*** is lower for **NAP-3** than that of **NAP** or **NAP-2** or some combination of both. Both the absorption and keto emission of **NAP-3** is lower and higher than both **NAP** and **NAP-2**, respectively and thus this qualitative assessment holds true.

Table 4.2 Spectroscopic properties of 2-(hydroxynaphthyl)-benzoxazole family

	Abs $\lambda_{\max}$ (nm)	Em $\lambda_{\max}$ (nm)	Stokes Shift $\lambda_{\max}$ (nm)
 <b>NAP</b>	378	400, 460	22, 82
 <b>NAP-2</b>	373	400, 466	27, 93
 <b>NAP-3</b>	337	417, 700	80, 363

Previously, relative Stokes shifts in benzoxazole-based ESIPT dyes were explained using Baird's rule where the more aromatic the ground-state molecule is, the more (anti)aromatic the excited-state becomes. With respect to the ESIPT process, the more (anti)aromatic a molecule is the larger the driving force to isomerize to the nonaromatic keto form which results in a larger Stokes shift. The aforementioned naphthalene derivatives, all by Hückel's  $[4n+2]$  rule, show the same degree of aromaticity and thus Baird's rule alone cannot explain these spectroscopic differences. In fact, a limitation of Hückel aromaticity is in the evaluation of the relative stability of structural isomers and of the local aromaticity within polycyclic aromatic hydrocarbons (PAHs), such as naphthalene. In 1972, Erich Clar developed a simple set of rules to address this deficiency<sup>30</sup> which have subsequently become known as Clar's aromatic sextets (or simply Clar Sextets).<sup>42</sup> Briefly, the theory of Clar Sextets states that the most dominant resonance form of a molecule is one in which the maximum number of disjoint  $\pi$ -aromatic sextets can be drawn, where an aromatic  $\pi$ -aromatic sextet (consisting of  $[4n+2]$   $\pi$ -electrons) is typically represented by a circle. An example of phenanthrene is shown below (Scheme 4.2). Phenanthrene can either be drawn as resonance forms **1a** or **1b**. However, because **1a** has more disjoint  $\pi$ -aromatic sextets, it can be considered the more dominant resonance form. In fact, experiment supports this idea as the 9,10 CC bond in phenanthrene is the most reactive and shares similar reactivity to a standalone CC double bond.

Scheme 4.2 Possible resonance forms of phenanthrene using Clar's Sextets



Where this relates to the differences between the emissions of **NAP**, **NAP-2**, and **NAP-3** is the *relative* aromaticity of each of the naphthalene keto isomers. After ESIPT occurs in the naphthalene derivatives, **NAP** and **NAP-2** isomerize such that they contain one Clar sextet

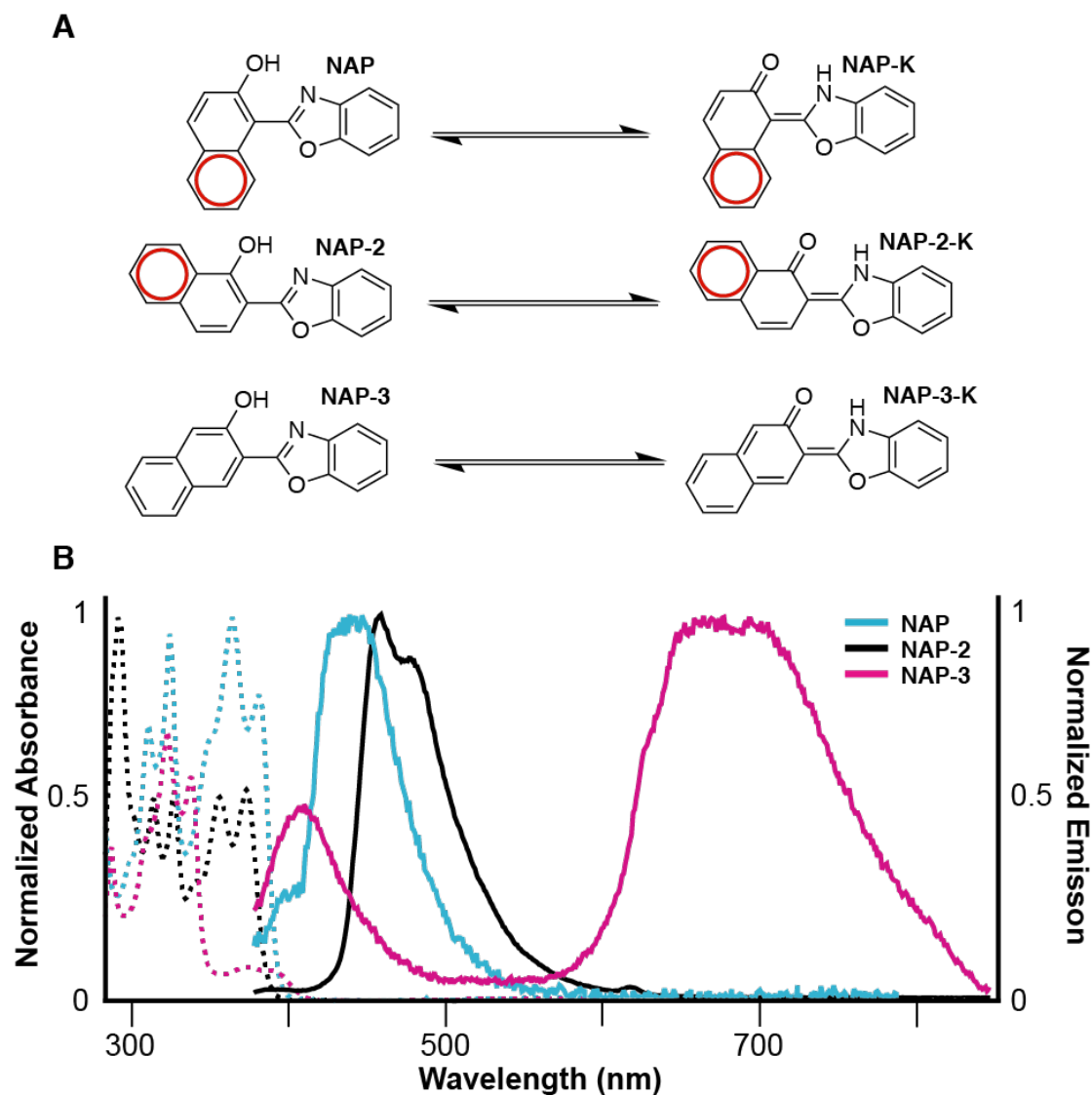


Figure 4.9 (A) Isomerization of Naphthalene ESIP chromophores. Upon isomerization, the number of Clar sextets for **NAP** and **NAP-2** remains the same. (B) Overlaid absorption and emission profiles of naphthalene ESIP chromophores.

whereas **NAP-3** isomerizes to contain zero Clar sextets (Figure 4.9A). In fact, the number of Clar sextets remains the same for **NAP** and **NAP-2** which likely explains their small Stokes shifts. Although **NAP** and **NAP-2** isomerized to relieve excited-state (anti)aromaticity from  $E^*$ , because they contain one Clar sextet, they each still have some degree of (anti)aromaticity.<sup>43, 44</sup> This higher degree of (anti)aromaticity results in a higher  $K^*$  energy relative to that of **NAP-3**. A higher  $K^*$  energy will result in a lower wavelength emission, which is what is observed (Figure 4.9B). It can then be concluded the larger Stokes shift of **NAP-3** is a result of a large stabilizing excited-state tautomerization energy that relieves all (anti)aromaticity and thus provides an example of how the complementary nature of Baird's rule can be utilized in photochemical design. To my knowledge, the role of aromaticity in the benzoxazole moiety has not been explored.

### Conclusion

We present compelling evidence that aromaticity plays a key role in determining the energetic difference between tautomeric species in the excited state. This result has immediate implications for the design of ESIPT chromophores based on **HBO**. The ESIPT process has been applied to the development of new functional molecules and sensors.<sup>20, 21, 45</sup> Thus, an understanding of how structure relates to spectral features is critical to the design of novel ESIPT materials. This work reveals that expansion of conjugation is not a viable strategy to red-shift the emissive properties of ESIPT fluorophores unless expansion of the  $\pi$ -system leads to a more aromatic phenolic partner than the base phenol in **HBO**. Notably, this result runs contrary to traditional chromophore design principles in which expansion of conjugation generally leads to a red-shift in absorbance and emissive properties. These results can only be rationalized by considering Baird's rule (see below).



We propose that the aromaticity of the phenolic ring should be given strong consideration during the design of novel ESIPT chromophores as it can dramatically impact the Stokes shift of keto emission. Further, we predict that strategies centered around using electron-donating and electron-withdraw substitution (so called “push-pull” chromophores) may provide more fruitful avenues to increase the Stokes shift of keto emission, as has been demonstrated.<sup>46</sup> To date, however, a systematic investigation of the role that substitution of the **HBO** core can play in tuning the absorbance and enol vs keto emission features of **HBO** has not been experimentally demonstrated.<sup>25</sup>

More generally, this work corroborates the tenets of Baird’s rule that  $[4n + 2]$  Hückel aromatic character in the ground state flips to antiaromatic character in the excited state.<sup>10</sup> Furthermore, experimental evidence for Baird’s rule operating in the singlet excited state is lacking.<sup>12-15</sup> This report provides experimental demonstration of Baird’s rule in the singlet state, where the excited-state isomerization observed in **HBO** can be rationalized to be a process by which excited-state antiaromaticity is alleviated via intramolecular proton transfer to a quinoidal isomer.

Finally, this work proposes and demonstrates a largely intuitive concept within Baird’s rule that greater aromaticity in  $S_0$  leads to greater antiaromaticity in  $S_1$ , and presumably vice versa in terms of antiaromaticity in  $S_0$ .

## Experimental

### Computational Details

(Done by Peter B. Karadakov) All complete-active-space self-consistent field calculations with gauge-including atomic orbitals (CASSCF-GIAO) on benzene and naphthalene reported in this paper were carried out using the MCSCF-GIAO (multiconfigurational SCF with

GIAOs) methodology<sup>44,45</sup> and implemented in the Dalton 2016.2 program package,<sup>46</sup> within the 6-311+G\* basis set.

The  $S_0(1^1A_{1g})$  and  $S_1(1^1B_{2u})$  electronic states of benzene were described using state-optimized p-space CASSCF(6,6) wavefunctions (with ‘6 electrons in 6 orbitals’), at the experimental  $D_{6h}$  gas-phase ground-state geometry established through analysis of the  $n_4$  vibration–rotation bands of  $C_6H_6$  and  $C_6D_6$ .<sup>47</sup> The geometry of benzene chosen for the current calculations is identical to that used in previous shielding studies.<sup>12,15,48</sup>

In the calculations on the  $S_0(1^1A_g)$  and  $S_1(1^1B_{3u})$  electronic states of naphthalene we employed state-optimized p-space CASSCF(10,10) wavefunctions (with ‘10 electrons in 10 orbitals’), at the  $D_{2h}$  gas-phase ground-state geometry determined through a combination of ultrahigh-resolution laser spectroscopy and ab initio calculations.<sup>49</sup>

As ground-state geometries were used in excited state calculations, the comparisons between the properties of the  $S_0$  and  $S_1$  electronic states of benzene and naphthalene are in the context of vertical excitations.

$s_{iso}(r)$  contour plots for the  $S_0$  and  $S_1$  electronic states of benzene and naphthalene were constructed using regular grids of points with a spacing of 0.05 Å. To reduce computational effort, for each grid  $s_{iso}(r)$  values were calculated within one quadrant of the respective grid only and replicated by symmetry.

The CASSCF(6,6)/6-311+G\* and CASSCF(10,10)/6-311+G\*  $S_1' S_0$  vertical excitation energies of 4.98 eV and 4.22 eV that we obtained for benzene and naphthalene, respectively, agree well with experimental data and other theoretical results.<sup>12,50</sup>

Additional data on NICS and magnetic susceptibilities for the  $S_0$  and  $S_1$  electronic states of benzene and naphthalene, calculated at the CASSCF(6,6)-GIAO/6-311+G\* and

CASSCF(10,10)- GIAO/6-311+G\* levels of theory, respectively, are reported in Table 2. The selection of NICS indices includes the original NICS index,  $\text{NICS}(0)$ ,<sup>51</sup> defined as  $\chi_{s_{\text{iso}}}$  (at ring center),  $\text{NICS}(1) = \chi_{s_{\text{iso}}}$  (at 1 Å above ring center),<sup>52,53</sup>  $\text{NICS}(0)_{zz} = \chi_{s_{zz}}$  (at ring center)<sup>54,55</sup> and  $\text{NICS}(1)_{zz} = \chi_{s_{zz}}$  (at 1 Å above ring center).<sup>56</sup> The magnetic susceptibility data is comprised of the isotropic magnetic susceptibilities,  $w_{\text{iso}}$ , and the out-of-plane components of the magnetic susceptibility tensor,  $w_{zz}$ .

The comparison between the CASSCF-GIAO NICS values for the  $S_0$  and  $S_1$  electronic states of benzene and naphthalene shows clearly that whereas, in the electronic ground states, the six-membered ring in benzene is more aromatic than a six-membered ring in naphthalene, in the first singlet excited states a six-membered ring in naphthalene is less antiaromatic (or, more aromatic) than the six-membered ring in benzene. The  $\text{NICS}(0)_{zz}$  and  $\text{NICS}(1)_{zz}$  indices suggest more pronounced differences between the aromaticities of the six-membered rings in the two molecules in each electronic state than do  $\text{NICS}(0)$  and  $\text{NICS}(1)$ . The CASSCF(6,6)-GIAO/6-311+G\* NICS values for the  $S_0$  and  $S_1$  electronic states of benzene are in good agreement with the corresponding CASSCF(6,6)-GIAO/6-311++G(2d,2p) NICS data from literature,<sup>12</sup> which is an indication that the accuracy afforded by the 6-311+G\* basis is sufficient for the purposes of the current investigation. As expected, the NICS data in Table 2 fully supports the conclusions following from the analyses of Fig. 4–7.

When comparing the isotropic magnetic susceptibilities and the out-of-plane components of the magnetic susceptibility tensor for the two molecules, it is important to remember that these are ‘entire molecule’ and not ‘per ring’ values, so each of  $w_{\text{iso}}$  and  $w_{zz}$  for naphthalene needs to be divided by 2 before juxtaposing it with the correspond value for benzene. A comparison of this type leads to conclusions analogous to those derived from the NICS values, with one exception:

due to the larger differences between the diagonal components of the  $S_1$  magnetic susceptibility tensor for naphthalene, the corresponding  $w_{\text{iso}}$  value turns out to be higher than the corresponding value for benzene.

Finally, we note that HBO and NAP possess large p-systems making calculation of the full p-space by CASSCF impractical. For this reason, we chose TD-DFT to analyze these molecules in Fig. 8 (see ESI† for details). TD-DFT allowed for computation of these systems in a straightforward manner, introducing correlation effects for both core and valence electrons. However, TD-DFT cannot be used to describe singlet excited state (anti)aromaticity as the required methodology has not been developed and implemented in code.

(Done by Bryan J. Lampkin) Computations for Figure 4.8 were performed using the Gaussian09 suite. B3LYP and TD-B3LYP were the functional and method of choice.<sup>47, 48</sup> This selection was justified by its use in modeling ESIPT fluorescence<sup>23</sup> as well as by the fact that our own functional screen of HBO absorption showed that B3LYP best matched experiment (Table 4.3). All optimized geometries were verified to be local minima by the absence of any imaginary frequencies in the vibrational analysis. Ground state and excited state vibrational analyses were done using analytic and numeric methods, respectfully. All geometric and vibrational parameters were determined using the 6-31+G(d) basis set while both ground and excited state electronic energies were determined using a more extended basis set, 6-311+G(d,p).<sup>49</sup> All calculations were obtained using default G09 parameters unless otherwise stated. Excited state geometries were obtained by taking the ground state optimized geometries and subjecting them to TD-DFT geometry optimizations. We restricted these optimizations to the respective first singlet excited states. Absorption values reported were obtained by vertically exciting the ground state optimized geometry from  $S_0$  to  $S_n$  while emission values reported were

obtained by vertically exciting the relaxed excited state optimized geometry from  $S_0$  to  $S_n$ .<sup>50</sup> All reported excited state energies are from the  $S_1$  state. There was no observed switching of orbitals involved in the lowest energy excited states across the ESIPT potential energy surface.

Table 4.3 TD-DFT functional screen of HBO  $S_0 - S_1$  excitation.

	$S_0-S_1$ Excitation Energy (eV)	$\Delta E$
Experiment	3.721	-
B3LYP	3.8691	0.1481
CAM-B3LYP	4.1859	0.3168
LC $\omega$ PBE	4.3936	0.2077
M062x	4.2393	-0.1543
PBE1PBE	3.9690	-0.2703
$\omega$ B97xD	4.2096	0.2406

### Calculated Coordinates

#### HBO Enol $S_0$

	X	Y	Z
C	-1.909668	0.646875	-0.000104
C	-1.957643	-0.753872	0.000088
C	-3.133332	-1.487597	0.000189
C	-4.315344	-0.737487	0.000086
C	-4.294835	0.670603	-0.000108
C	-3.095541	1.386595	-0.000206
C	0.113406	-0.081713	-0.000003
H	-3.136517	-2.572725	0.000338
H	-5.270141	-1.255644	0.000157
H	-5.237001	1.211691	-0.000181
H	-3.07823	2.472101	-0.000353
C	1.555516	-0.209335	-0.000032

#### HBO Keto $S_0$

	X	Y	Z
C	-1.951393	-0.762345	0.000084
C	-1.897317	0.636008	0.000006
C	-3.06524	1.394402	-0.000068
C	-4.274662	0.688658	-0.000041
C	-4.31158	-0.714885	0.000032
C	-3.134416	-1.47748	0.000103
C	0.175363	-0.184072	-0.000006
H	-3.038673	2.479275	-0.000088
H	-5.208229	1.243692	-0.000061
H	-5.270768	-1.22388	0.000043
H	-3.146714	-2.562243	0.000136
C	1.574482	-0.252043	-0.000077

C	2.179314	-1.474059	-0.000146
C	2.359699	0.962314	0.000085
C	3.56248	-1.586384	-0.000152
H	1.556226	-2.363017	-0.000232
C	3.757189	0.835161	0.000076
C	4.348668	-0.422605	-0.000041
H	4.030002	-2.566462	-0.000239
H	4.353003	1.742789	0.000169
H	5.432894	-0.501303	-0.000045
N	-0.571673	1.035072	-0.00015
O	-0.659946	-1.216608	0.000148
O	1.844458	2.209059	0.000221
H	0.855921	2.156492	0.000261

Energy -706.045492636 ht

HBO Enol S<sub>1</sub>

	X	Y	Z
C	-1.893169	0.644606	0.000097
C	-1.97314	-0.772939	-0.0001
C	-3.160564	-1.478466	-0.00014
C	-4.339585	-0.704888	0.000023
C	-4.290526	0.702631	0.000221
C	-3.082863	1.403363	0.000264
C	0.121567	-0.149653	-0.000122
H	-3.182586	-2.56345	-0.000287
H	-5.302905	-1.206635	-0.000001
H	-5.224045	1.259586	0.000344
H	-3.05108	2.488363	0.000415
C	1.537353	-0.26669	-0.000112
C	2.235327	-1.481692	-0.000006
C	2.343523	0.953639	-0.000083
C	3.653682	-1.510932	0.000179
H	1.677923	-2.412313	-0.00002
C	3.752054	0.902067	0.000125
C	4.416211	-0.333887	0.000264
H	4.152474	-2.476231	0.000277
H	4.290903	1.844393	0.000141
H	5.500242	-0.375785	0.000412
N	-0.576484	1.004623	0.000074

C	2.292978	1.025381	-0.000029
C	2.270688	-1.495673	-0.000131
C	3.730913	0.924903	0.00006
C	3.643422	-1.522135	-0.000037
H	1.698734	-2.420018	-0.000136
C	4.366619	-0.293115	0.000096
H	4.287739	1.85747	0.00008
H	4.177475	-2.467538	-0.000001
H	5.454502	-0.324831	0.000159
N	-0.544262	0.952867	0.000111
O	-0.656044	-1.259518	0.000031
O	1.693513	2.148909	-0.000159
H	0.036875	1.827253	0.000157

Energy -706.026821884 ht

HBO Keto S<sub>1</sub>

	X	Y	Z
C	-1.970353	-0.754419	0.000015
C	-1.941314	0.649241	-0.000108
C	-3.132536	1.394356	-0.00011
C	-4.325172	0.652606	0.000033
C	-4.337698	-0.74742	0.000157
C	-3.136586	-1.497079	0.000145
C	0.152225	-0.134059	-0.000155
H	-3.130677	2.478873	-0.000218
H	-5.271185	1.187412	0.000036
H	-5.287355	-1.273798	0.000257
H	-3.127469	-2.581247	0.000242
C	1.596921	-0.225383	-0.000079
C	2.364158	1.015397	-0.000028
C	2.247964	-1.442227	-0.000119
C	3.785077	0.891452	0.000114
C	3.685234	-1.527249	-0.00006
H	1.668994	-2.362192	-0.000239
C	4.434393	-0.368064	0.000066
H	4.357579	1.814348	0.000306
H	4.156298	-2.505081	-0.00009
H	5.520078	-0.412576	0.000168
N	-0.602317	0.982958	-0.000266

O -0.691934 -1.275143 -0.000214  
 O 1.756691 2.143847 -0.000356  
 H 0.737182 2.017117 -0.000889

Energy -705.90895572 ht

O -0.663577 -1.222354 -0.000027  
 O 1.775697 2.153422 0.000346  
 H -0.10087 1.88209 -0.000371

Energy -705.919838633 ht

NAP Enol S<sub>0</sub>

	X	Y	Z
C	2.758526	0.553797	-0.000014
C	2.454815	-0.812189	0.000044
C	3.407447	-1.818653	0.000105
C	4.740185	-1.390223	0.000088
C	5.073236	-0.021714	0.000023
C	4.092561	0.972658	-0.000023
C	0.603793	0.355956	-0.000213
H	3.137984	-2.86985	0.000149
H	5.534186	-2.131498	0.000126
H	6.121038	0.265615	0.000022
H	4.349006	2.027573	-0.00005
C	-0.820426	0.640956	-0.00011
C	-1.867548	-0.367661	-0.000066
C	-1.187739	2.007545	-0.000029
C	-1.636649	-1.772181	-0.000128
C	-3.237716	0.061339	0.000047
C	-2.553353	2.396052	0.000082
C	-2.682882	-2.677779	-0.000082
H	-0.626952	-2.152743	-0.000212
C	-4.287573	-0.891993	0.000091
C	-3.541731	1.45291	0.000118
H	-2.769982	3.4595	0.000139
C	-4.02463	-2.245429	0.000028
H	-2.459307	-3.741822	-0.000133
H	-5.313088	-0.528743	0.000177
H	-4.585743	1.757948	0.000208
H	-4.836169	-2.967914	0.000063
O	1.083016	-0.933102	0.00002
N	1.562599	1.259426	0.000001
O	-0.313865	3.026006	-0.000042
H	0.615738	2.662373	-0.000091

NAP Keto S<sub>0</sub>

	X	Y	Z
C	2.774045	0.547133	0.000032
C	2.458106	-0.813875	-0.000142
C	3.408793	-1.817305	-0.000127
C	4.746452	-1.394566	0.000078
C	5.081394	-0.031209	0.000252
C	4.101578	0.969385	0.000229
C	0.546226	0.307955	-0.000094
H	3.133353	-2.866665	-0.000267
H	5.536585	-2.139374	0.000093
H	6.128477	0.257528	0.0004
H	4.363813	2.022484	0.000353
C	-0.820597	0.62022	0
C	-1.894232	-0.371747	0.000017
C	-1.124037	2.054085	0.00009
C	-1.694433	-1.774473	-0.000024
C	-3.245971	0.092116	0.000091
C	-2.524451	2.433781	0.000025
C	-2.765477	-2.660011	0.000014
H	-0.692599	-2.179159	-0.000078
C	-4.315878	-0.827559	0.00012
C	-3.514655	1.506257	0.000085
H	-2.731728	3.499582	-0.000064
C	-4.089698	-2.194505	0.000087
H	-2.566804	-3.729107	-0.000014
H	-5.33256	-0.439675	0.000163
H	-4.556254	1.823489	0.000092
H	-4.921803	-2.893203	0.000111
O	1.07846	-0.948897	-0.000321
N	1.556042	1.209513	-0.000078
O	-0.236974	2.960789	-0.000255
H	1.252358	2.208289	-0.000031

Energy -859.688097079

Energy -859.677383604 ht

NAP Enol S<sub>1</sub>NAP Keto S<sub>1</sub>

	X	Y	Z		X	Y	Z
C	2.746414	0.558244	0.000045	C	2.778927	0.562854	0.000024
C	2.448373	-0.824969	-0.000043	C	2.470188	-0.806861	-0.00001
C	3.404388	-1.822081	-0.000061	C	3.425511	-1.806698	-0.000036
C	4.742144	-1.387482	0.000015	C	4.766682	-1.370947	-0.000026
C	5.070463	-0.015147	0.000104	C	5.092736	-0.005745	0.000011
C	4.092034	0.977574	0.000121	C	4.113046	0.996139	0.000038
C	0.582911	0.339203	-0.000053	C	0.549378	0.309794	0.00001
H	3.140306	-2.874685	-0.000126	H	3.156762	-2.857466	-0.000062
H	5.538564	-2.126059	0.000005	H	5.562184	-2.110053	-0.000045
H	6.118345	0.272894	0.000159	H	6.139547	0.285532	0.00002
H	4.346074	2.03289	0.000187	H	4.37056	2.04999	0.000068
C	-0.805054	0.622292	-0.000053	C	-0.84355	0.61429	0.00002
C	-1.872377	-0.370671	-0.000026	C	-1.891711	-0.35993	0.000012
C	-1.198158	2.045999	-0.000034	C	-1.190794	2.067684	0.000028
C	-1.645426	-1.76861	-0.000049	C	-1.664131	-1.775749	0.000001
C	-3.244045	0.080067	0.000042	C	-3.279454	0.096197	0.000014
C	-2.5373	2.426679	0.000035	C	-2.571092	2.432391	-0.000009
C	-2.69719	-2.702925	-0.000014	C	-2.705178	-2.687103	-0.000003
H	-0.632837	-2.143447	-0.000097	H	-0.650125	-2.148295	-0.000005
C	-4.278505	-0.880836	0.000078	C	-4.307261	-0.863521	0.00001
C	-3.549639	1.466479	0.000075	C	-3.578967	1.487695	-0.000001
H	-2.759195	3.488772	0.000047	H	-2.785452	3.496529	-0.00004
C	-4.016841	-2.258472	0.00005	C	-4.040563	-2.230687	0.000004
H	-2.46739	-3.764335	-0.000035	H	-2.490734	-3.751818	-0.000012
H	-5.308137	-0.530108	0.00013	H	-5.337923	-0.515946	0.000009
H	-4.591444	1.775138	0.000127	H	-4.621953	1.794078	-0.000017
H	-4.842198	-2.965362	0.000079	H	-4.861821	-2.942483	0
O	1.082496	-0.959649	-0.000092	O	1.095506	-0.948394	-0.000013
N	1.574466	1.253903	0.00003	N	1.56721	1.210255	0.000042
O	-0.289176	3.02445	-0.000131	O	-0.278919	2.956038	-0.000089
H	0.636928	2.626496	-0.000307	H	1.27319	2.208174	0.000078

Energy -859.566916014 ht

Energy -859.563201528 ht



## References

1. Gleiter, R.; Haberhauer, G., *Aromaticity and Other Conjugation Effects*. Wiley-VCH: Weinheim, Germany, 2012.
2. Martin, N.; Haley, M. M.; Tykwinski, R., *Aromaticity: A Web Themed Issue, Chem. Commun.* 2012; Vol. 48.
3. Schleyer, P. v. R., *Chem. Rev.* **2005**, *105*, complete issue 10.
4. Baird, N. C., Quantum Organic Photochemistry .2. Resonance and Aromaticity in Lowest Pi-3-Pi] State of Cyclic Hydrocarbons. *Journal of the American Chemical Society* **1972**, *94* (14), 4941-&.
5. Aihara, J., Aromaticity-Based Theory of Pericyclic Reactions. *B Chem Soc Jpn* **1978**, *51* (6), 1788-1792.
6. Fratev, F.; Monev, V.; Janoschek, R., Abinitio Study of Cyclobutadiene in Excited-States - Optimized Geometries, Electronic-Transitions and Aromaticities. *Tetrahedron* **1982**, *38* (19), 2929-2932.
7. Wrackmeyer, B.; Schanz, H. J.; Hofmann, M.; Schleyer, P. V. R., A New Carborane Cage: Hexacarba-arachno-dodecaborane(12). *Angew Chem Int Ed Engl* **1998**, *37* (9), 1245-1247.
8. Kataoka, M., Magnetic susceptibility and aromaticity in the excited states of benzene. *J Chem Res* **2004**, (8), 573-574.
9. Soncini, A.; Fowler, P. W., Ring-current aromaticity in open-shell systems. *Chemical Physics Letters* **2008**, *450* (4-6), 431-436.
10. Rosenberg, M.; Dahlstrand, C.; Kilsa, K.; Ottosson, H., Excited state aromaticity and antiaromaticity: opportunities for photophysical and photochemical rationalizations. *Chem Rev* **2014**, *114* (10), 5379-425.
11. Ottosson, H., Organic photochemistry: Exciting excited-state aromaticity. *Nat Chem* **2012**, *4* (12), 969-71.
12. Karadakov, P. B., Ground- and excited-state aromaticity and antiaromaticity in benzene and cyclobutadiene. *J Phys Chem A* **2008**, *112* (31), 7303-9.
13. Karadakov, P. B., Aromaticity and antiaromaticity in the low-lying electronic states of cyclooctatetraene. *J Phys Chem A* **2008**, *112* (49), 12707-13.
14. Feixas, F.; Vandenbussche, J.; Bultinck, P.; Matito, E.; Sola, M., Electron delocalization and aromaticity in low-lying excited states of archetypal organic compounds. *Phys Chem Chem Phys* **2011**, *13* (46), 20690-703.

15. Karadakov, P. B.; Hearnshaw, P.; Horner, K. E., Magnetic Shielding, Aromaticity, Antiaromaticity, and Bonding in the Low-Lying Electronic States of Benzene and Cyclobutadiene. *J Org Chem* **2016**, *81* (22), 11346-11352.
16. Ueda, M.; Jorner, K.; Sung, Y. M.; Mori, T.; Xiao, Q.; Kim, D.; Ottosson, H.; Aida, T.; Itoh, Y., Energetics of Baird aromaticity supported by inversion of photoexcited chiral [4n]annulene derivatives. *Nat Commun* **2017**, *8* (1), 346.
17. Fischer, L. J.; Dutton, A. S.; Winter, A. H., Anomalous effect of non-alternant hydrocarbons on carbocation and carbanion electronic configurations. *Chem Sci* **2017**, *8* (6), 4231-4241.
18. Ayub, R.; Papadakis, R.; Jorner, K.; Zietz, B.; Ottosson, H., Cyclopropyl Group: An Excited-State Aromaticity Indicator? *Chemistry - A European Journal* **2017**, *23* (55), 13684-13695.
19. Oh, J.; Sung, Y. M.; Mori, H.; Park, S.; Jorner, K.; Ottosson, H.; Lim, M.; Osuka, A.; Kim, D., Unraveling Excited-Singlet-State Aromaticity via Vibrational Analysis. *Chem-U.S* **2017**, *3* (5), 870-880.
20. Zhao, J.; Ji, S.; Chen, Y.; Guo, H.; Yang, P., Excited state intramolecular proton transfer (ESIPT): from principal photophysics to the development of new chromophores and applications in fluorescent molecular probes and luminescent materials. *Phys Chem Chem Phys* **2012**, *14* (25), 8803-17.
21. Sedgwick, A. C.; Wu, L.; Han, H. H.; Bull, S. D.; He, X. P.; James, T. D.; Sessler, J. L.; Tang, B. Z.; Tian, H.; Yoon, J., Excited-state intramolecular proton-transfer (ESIPT) based fluorescence sensors and imaging agents. *Chem Soc Rev* **2018**, *47* (23), 8842-8880.
22. Iijima, T.; Momotake, A.; Shinohara, Y.; Sato, T.; Nishimura, Y.; Arai, T., Excited-state intramolecular proton transfer of naphthalene-fused 2-(2'-hydroxyaryl)benzazole family. *J Phys Chem A* **2010**, *114* (4), 1603-9.
23. Kanda, T.; Momotake, A.; Shinohara, Y.; Sato, T.; Nishimura, Y.; Arai, T., Photoinduced Proton Transfer in 2-(2'-Hydroxynaphthalenyl)-benzoxazole: Observation of Fluorescence with a Small Stokes Shift Induced by Excited-State Intramolecular Proton Transfer. *B Chem Soc Jpn* **2009**, *82* (1), 118-120.
24. Roohi, H.; Hejazi, F.; Mohtamedifar, N.; Jahantab, M., Excited state intramolecular proton transfer (ESIPT) in 2-(2'-hydroxyphenyl)benzoxazole and its naphthalene-fused analogs: A TD-DFT quantum chemical study. *Spectrochim Acta A* **2014**, *118*, 228-238.
25. Azarias, C.; Budzak, S.; Laurent, A. D.; Ulrich, G.; Jacquemin, D., Tuning ESIPT fluorophores into dual emitters. *Chem Sci* **2016**, *7* (6), 3763-3774.
26. Gutierrez-Arzaluz, L.; Cortes-Guzman, F.; Rocha-Rinza, T.; Peon, J., Ultrafast excited state hydrogen atom transfer in salicylideneaniline driven by changes in aromaticity. *Phys Chem Chem Phys* **2015**, *17* (47), 31608-12.

27. Nishina, N.; Mutai, T.; Aihara, J. I., Excited-State Intramolecular Proton Transfer and Global Aromaticity. *J Phys Chem A* **2017**, *121* (1), 151-161.
28. Setiawan, D.; Kraka, E.; Cremer, D., Quantitative Assessment of Aromaticity and Antiaromaticity Utilizing Vibrational Spectroscopy. *J Org Chem* **2016**, *81* (20), 9669-9686.
29. Giambiagi, M.; de Giambiagi, M. S.; Silva, C. D. D.; de Figueiredo, A. P., Multicenter bond indices as a measure of aromaticity. *Physical Chemistry Chemical Physics* **2000**, *2* (15), 3381-3392.
30. Clar, E., *The Aromatic Sextet*. Wiley: London, NY, 1972.
31. Krygowski, T. M.; Cyranski, M. K., Structural aspects of aromaticity. *Chem Rev* **2001**, *101* (5), 1385-419.
32. Chen, Z.; Wannere, C. S.; Corminboeuf, C.; Puchta, R.; Schleyer, P., Nucleus-independent chemical shifts (NICS) as an aromaticity criterion. *Chem Rev* **2005**, *105* (10), 3842-88.
33. Fias, S.; Fowler, P. W.; Delgado, J. L.; Hahn, U.; Bultinck, P., Correlation of delocalization indices and current-density maps in polycyclic aromatic hydrocarbons. *Chem. - Eur. J.* **2008**, *14* (10), 3093-3099.
34. Van Damme, S.; Acke, G.; Havenith, R. W. A.; Bultinck, P., Can the current density map topology be extracted from the nucleus independent chemical shifts? *Phys. Chem. Chem. Phys.* **2016**, *18* (17), 11746-11755.
35. Krygowski, T. M.; Szatyłowicz, H.; Stasyuk, O. A.; Dominikowska, J.; Palusiak, M., Aromaticity from the viewpoint of molecular geometry: application to planar systems. *Chem Rev* **2014**, *114* (12), 6383-422.
36. Palmer, I. J.; Ragazos, I. N.; Bernardi, F.; Olivucci, M.; Robb, M. A., An Mc-Scf Study of the S1 and S2 Photochemical-Reactions of Benzene. *Journal of the American Chemical Society* **1993**, *115* (2), 673-682.
37. Dreyer, J.; Klessinger, M., The photochemical formation of fulvene from benzene via prefulvene - A theoretical study. *Chem-Eur J* **1996**, *2* (3), 335-341.
38. Malar, E. J. P.; Jug, K., Structures and Properties of Excited-States of Benzene and Some Monosubstituted Benzenes. *Journal of Physical Chemistry* **1984**, *88* (16), 3508-3516.
39. Brémond, E.; Savarese, M.; Adamo, C.; Jacquemin, D., Accuracy of TD-DFT Geometries: A Fresh Look. *Journal of Chemical Theory and Computation* **2018**, *14* (7), 3715-3727.

40. Jacquemin, D., What is the Key for Accurate Absorption and Emission Calculations, Energy or Geometry? *Journal of Chemical Theory and Computation* **2018**, *14* (3), 1534-1543.
41. Laurent, A. D.; Jacquemin, D., TD-DFT benchmarks: A review. *International Journal of Quantum Chemistry* **2013**, *113* (17), 2019-2039.
42. Solà, M., Forty years of Clar's aromatic  $\pi$ -sextet rule. *Frontiers in chemistry* **2013**, *1*, 22-22.
43. Wu, C.-H.; Karas, L. J.; Ottosson, H.; Wu, J. I.-C., Excited-state proton transfer relieves antiaromaticity in molecules. **2019**, (116), 20303-20308.
44. Nguyen, Y. H. An aromaticity view of proton transfer in ground state and excited state. Iowa State University, Graduate Theses and Dissertations, 2019.
45. Lampkin, B. J.; Monteiro, C.; Powers, E. T.; Bouc, P. M.; Kelly, J. W.; VanVeller, B., A designed protein binding-pocket to control excited-state intramolecular proton transfer fluorescence. *Org Biomol Chem* **2019**, *17* (5), 1076-1080.
46. Seo, J.; Kim, S.; Park, S. Y., Strong solvatochromic fluorescence from the intramolecular charge-transfer state created by excited-state intramolecular proton transfer. *J Am Chem Soc* **2004**, *126* (36), 11154-5.
47. Becke, A. D., Density-functional thermochemistry. III. The role of exact exchange. *Journal of Chemical Physics* **1998**, *98*, 5648-5652.
48. Lee, C.; Yang, W.; Parr, R. G., Development of the Colle-Salvetti correlation-energy formula into a functional of the electron density. *Physical Review B* **1988**, *37* (2), 785-789.
49. Houari, Y.; Charaf-Eddin, A.; Laurent, A. D.; Massue, J.; Ziessel, R.; Ulrich, G.; Jacquemin, D., Modeling optical signatures and excited-state reactivities of substituted hydroxyphenylbenzoxazole (HBO) ESIPT dyes. *Physical Chemistry Chemical Physics* **2014**, *16* (4), 1319-1321.
50. Adamo, C.; Jacquemin, D., The calculations of excited-state properties with Time-Dependent Density Functional Theory. *Chemical Society Reviews* **2013**, *42* (3), 845-856.

## CHAPTER 5. A MOLECULAR DOUBLE-MUTANT CYCLE TO UNTANGLE THE CONTRIBUTIONS OF AROMATICITY AND ELECTRONIC EFFECTS ON EXCITED-STATE INTRAMOLECULAR FLUORESCENCE

Bryan J. Lampkin, Yen H. Nguyen, Brett VanVeller\*

Department of Chemistry, Iowa State University, Ames, Iowa 50011, USA

Modified from a manuscript to be submitted

### Abstract

Excited-State Intramolecular Proton Transfer (ESIPT) fluorescence is an environmentally sensitive fluorescent pathway that can red-shift a chromophore's emission by often greater than 100 nm. Both the proton donor acidity and its ring aromaticity have shown to influence ESIPT spectral properties. In the following manuscript we describe an experimental method, which resembles the Double Mutant Cycle (DMC) commonly used in structural biology, to dissect the contributions of a ring's electron density, using hydroxyl group  $pK_a$  as an experimental proxy, and aromaticity in ESIPT. In examining ESIPT spectral properties by controlling systematically for a change in ring electron density and ring aromaticity, and then changing both properties together, we found that these two properties function independently of one another in ESIPT fluorescence.

### Introduction

Weak, non-covalent interactions play an important role in macromolecular events such as binding affinity or conformational equilibrium. Often, these non-covalent interactions function in a cooperative manner; that is, their combined effects on the overall system are non-additive.<sup>1</sup> Many, if not all, cooperative effects that have been studied with respect to intermolecular interactions.<sup>1-3</sup> However, it is feasible that two, independent, intramolecular properties can influence one another. For example, both a phenol ring's aromaticity and its acidity, an experimental indicator of electron density, manifests itself through the cyclic  $\pi$  system.<sup>4</sup>

Therefore, it stands to reason that that these two factors must be inherently interrelated. To our knowledge, studies to dissect this relationship are lacking and we seek to provide further insight.

An application where this relationship could play an important role is in the Excited-State Intramolecular Proton Transfer (ESIPT) fluorescent pathway.<sup>5-7</sup> ESIPT occurs when a conjugated molecule with an intramolecular hydrogen bond undergoes a proton transfer and subsequently isomerizes in the excited state (Figure 5.1A, See Ch1 for a more detailed discussion). This photon induced isomerization is often ascribed to the increase in both the acidity of the proton donor the basicity of the proton acceptor in the excited-state.<sup>8,9</sup> In fact, we recently demonstrated that derivatized 2-(2'-hydroxyphenol)benzoxazole (HBO) molecules, which undergo ESIPT, show both an increase in excited-state isomerization (as evidenced by an increase in keto emission) and a stabilization of the isomerized product (as evidenced by the decrease in the Stokes shift of the keto emission) as the phenol acidity increased by 5' derivatization (See Ch3). Additionally, the role of the phenol aromaticity has also been noted as a governing factor in a molecule's ability to undergo ESIPT.<sup>10,11</sup> We also recently showed, both theoretically and experimentally, that the more ground-state aromatic a molecule is, the more excited-state (anti)aromatic the molecule becomes and thus the driving force to excited-state isomerization to a nonaromatic species is greater. A consequence of this property is a larger observed Stokes shift of the keto emission and a comparatively greater keto emission ratio.

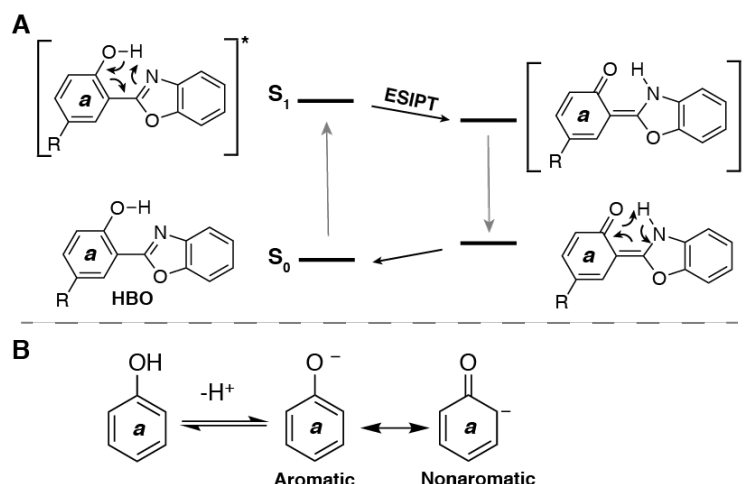


Figure 5.1(A) Schematic of the ESIP photochemical process of HBO. Previous studies have implicated the importance of both the R substituent and the aromaticity of ring *a* in the ESIP spectral properties. (B) Stabilization of phenolate via  $\pi$  electron delocalization to break aromaticity.

Naturally, this begs to question the interplay between phenol aromaticity and acidity in ESIP. Conceptually, if the acidity of a proton is dictated by the stability of the resulting conjugate base, then it can be rationalized that a less aromatic phenol derivative will be more acidic (than phenol) as its cost to dearomatize is less (Figure 5.1B). We postulate that any confounding effects between phenol aromaticity and acidity could be studied experimentally by a system that systematically varies ring *a*'s aromaticity and OH acidity independently. We view phenol acidity as a physical, measurable property of the electron density of a substituted phenol ring. Therefore, throughout this chapter, the use of phenol acidity and ring electron density are used interchangeably.

We were inspired by the double-mutant cycle (DMC) technique used in protein structure analysis to probe inter/intramolecular interactions in macromolecules (Figure 5.2A).<sup>12-15</sup> Briefly, in a double mutant cycle, two amino acid residues (*i* and *j*) are mutated individually in the system ( $X_{i,o}$  and  $X_{o,j}$ ) and then as a pair ( $X_{i,j}$ ); thus obtaining three experimental  $\Delta\Delta G$  values. The effects of the two mutations *i* and *j* are considered to interact and influence one another when parallel

$\Delta\Delta G$  are not equal (i.e.  $\Delta\Delta G_{o,o \rightarrow i,o} \neq \Delta\Delta G_{o,j \rightarrow i,j}$  and  $\Delta\Delta G_{o,o \rightarrow o,j} \neq \Delta\Delta G_{i,o \rightarrow i,j}$ ). The interaction energy can then be quantified as the difference between the doubly mutated structure and the sum of the individually mutated structures (energy of interaction =  $\Delta\Delta G_{i,j} - \Delta\Delta G_{i,o} + \Delta\Delta G_{o,j}$ ). If the mutations do not influence one another, then parallel  $\Delta\Delta G$  will be equal (i.e.  $\Delta\Delta G_{o,o \rightarrow i,o} = \Delta\Delta G_{o,j \rightarrow i,j}$  and  $\Delta\Delta G_{o,o \rightarrow o,j} = \Delta\Delta G_{i,o \rightarrow i,j}$ ) and the energy of interaction computes to zero.

We hypothesized that the comparative principles of the double mutant cycle could be applied to untangle the role that aromaticity and electron density might play in the ESIPT mechanism – where changes in aromaticity represent one mutation (vertical) and changes in hydroxyl  $pK_a$  represent the other (horizontal) (Figure 5.2B). However, the DMC is principally applied to mutants that affect the binding forces within macromolecules,<sup>15, 16</sup> where the free energy associated with stability can be directly measured (e.g., using isothermal calorimetry for example). Conversely, there are obvious impracticalities to mutating the properties of aromaticity and electron density in small molecules because these properties stem directly from their structure – making direct comparison of their free energies irrelevant. Instead, we sought to apply the DMC analysis in such a way that the contributions from aromaticity and hydroxyl  $pK_a$  could be interrogated and interpreted in the context of Excited-State Intramolecular Proton Transfer (ESIPT). Thus, we sought to redesign the DMC by identifying four distinct molecules, in which the magnitude of the change in aromaticity was selected to be same for each of the vertical parallel comparisons:

$$\Delta\text{aromaticity}_{1 \rightarrow 3} = \Delta\text{aromaticity}_{2 \rightarrow 4}$$

Likewise, the magnitude of the change in electron density was selected to be the same for each of the horizontal parallel comparisons:

$$\Delta\text{electron density}_{1 \rightarrow 2} = \Delta\text{electron density}_{3 \rightarrow 4}$$



In this context, we propose that if a given experimental parameter ( $P$ ) was interrogated and found to alter these parallel comparisons such that,

$$\Delta P_{1 \rightarrow 3} \neq \Delta P_{2 \rightarrow 4} \text{ and } \Delta P_{1 \rightarrow 2} \neq \Delta P_{3 \rightarrow 4}$$

Then aromaticity and electron density would be understood to interact to modify and/or determine the experimental parameter  $P$ . In contrast, if,

$$\Delta P_{1 \rightarrow 3} = \Delta P_{2 \rightarrow 4} \text{ and } \Delta P_{1 \rightarrow 2} = \Delta P_{3 \rightarrow 4}$$

we propose that aromaticity and electron density are independent in determining the experimental parameter  $P$ .

The analysis proposed above is a reimagining of the classical DMC used for protein structure analysis. This analysis instead works backwards from a system that is programed to display no interaction between the aromaticity and electron density mutations due to parallel interactions that have been pre-selected to be equal. Deviations from this exclusivity, therefore, probes the effect of changing electron density while keeping aromaticity constant and vice versa. Our proposed DMC along with an application to ESIPT are outlined below.

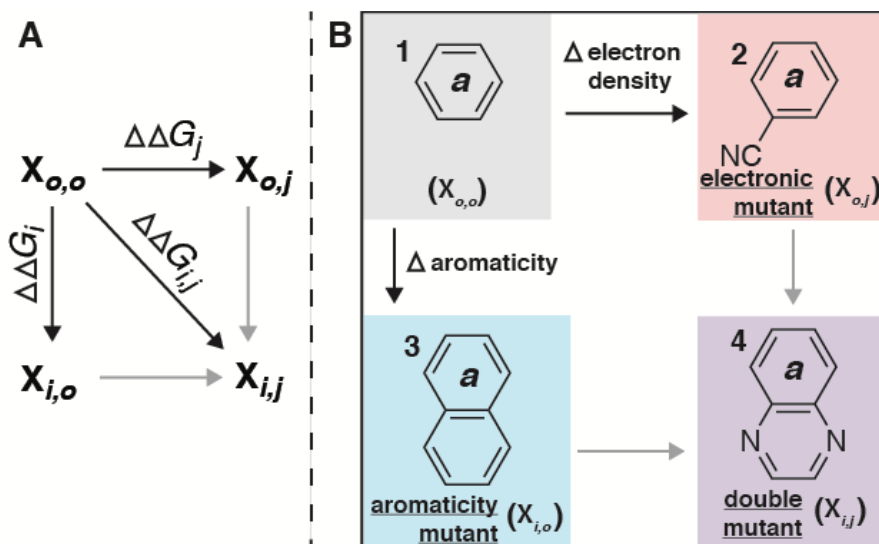


Figure 5.2 (A) Diagram of a DMC analysis. Quantification of the interaction between  $i$  &  $j$  is accomplished by subtracting the sum of the individual mutants from the double mutant. (B) Envisioned molecular DMC where electron density is varied laterally and aromaticity is varied horizontally in the diagram. See below for a more detailed discussion.

## Results and Discussion

### Design of the linear free energy analysis

We sought to apply the comparative strategies of the double mutant cycle to untangle the role that aromaticity and the hydroxyl  $pK_a$  might play in ES IPT. Towards this end, we identified molecules that could be suitably compared following the rationale outlined above (Figure 5.2B).

- i. Benzene, **1**, serves as the starting structure ( $X_{o,o}$ ).
- ii. Benzonitrile, **2**, represents the electron-density mutant ( $X_{o,j}$ ) – in which a decrease of electron density is probed while holding the aromaticity of the benzene moiety constant.

An experimental manifestation of this effect can be observed in comparing the  $pK_a$  values of the corresponding phenolic derivatives (**5** & **6**), where, as anticipated, 4-Cyanophenol (**6**) is more acidic ( $\Delta pK_a = 1.91$ , Table 5.1) than phenol, **5**. Based on several calculated aromatic indices based on thermodynamic, magnetic and geometric methods (Table 5.1 ,

see Experimental section for a description of each index and methods of computation), the aromaticity of the benzene ring of benzonitrile maintains a similar aromaticity to phenol. Substituent effects have shown little to no effect on ground state aromaticity.

- iii. Naphthalene, **3**, represents the compliment to benzonitrile as the aromaticity mutant ( $X_{i,o}$ ) while holding the electron density constant. The aromaticity of ring **a** changes based on the aromatic indices in Table 5.1 and Figure 5.3. Conversely, the electron-withdrawing effect, which is estimated by the similar OH  $pK_a$  values between 2-naphthol, **7**, and **5** is held constant.
- iv. Finally, we identified quinoxaline, **4**, as the double mutant in terms of electron density and aromaticity ( $X_{i,j}$ ) (Table 5.1). Quinoxaline was selected because its phenolic derivative, **8**, displayed the same change in  $pK_a$  (a proxy for electron-withdrawing ability) compared to **7** as was observed for **5** compared to **6**, such that the two horizontal, parallel comparisons are commensurate (Table 5.1 and Figure 5.3).

$$\text{If } \Delta pK_{a\ 5 \rightarrow 6} \approx \Delta pK_{a\ 7 \rightarrow 8}$$

$$\text{Then } \Delta \text{electron density}_{5 \rightarrow 6} \approx \Delta \text{electron density}_{7 \rightarrow 8}$$

Likewise, the computed aromatic indices (Table 5.1) of **4/8** were similar to those of **3/7** ensuring a similar change in aromaticity in the two vertical comparisons.

$$\Delta \text{aromaticity}_{5 \rightarrow 7} \approx \Delta \text{aromaticity}_{6 \rightarrow 8}$$

These molecules set up the parallel relationships described in the introduction. Deviations from this exclusivity, therefore, probes the effect of changing electron density while keeping aromaticity constant and vice versa.

Admittedly, the analysis in Figure 5.2B and Figure 5.3 is necessarily more qualitative in nature than the classical DMC used in protein structure analysis (Figure 5.2A). Despite

molecules **1-4** being judiciously chosen to ensure that the magnitude of  $\Delta$ aromaticity and  $\Delta pK_a$  were commensurate across each comparison, we should not necessarily expect perfect cancellation. We propose that this analysis is ‘as accurate as possible’ and sought to test our proposed DMC with an application to understanding the ESIPT fluorescent mechanism (Scheme 5.1). Additionally, it is important to note that there is no one accurate descriptor of aromaticity. Instead, it’s important to use several different descriptors.<sup>17</sup> We prudently chose to characterize a molecule’s aromaticity by means of structural, energetic and magnetic criteria and the general trend of an increase or decrease in aromaticity is consistent across all three descriptors.

Table 5.1 Aromatic index and electron density values for the DMC molecules

	Aromaticity			Electron Density
	HOMA <sup>a</sup>	ASE ( $\Delta H$ ) <sup>b</sup>	NICS(1)	pK <sub>a</sub>
<b>1</b>	0.99	33.36	10.45	-
<b>5</b>	0.99	-	10.15	9.88 <sup>c</sup>
<b>2</b>	0.99	33.41	10.60	-
<b>6</b>	0.99	-	10.13	7.97 <sup>c</sup>
<b>3</b>	0.81	22.05	10.71	-
<b>7</b>	0.81	-	10.64	9.51 <sup>c</sup>
<b>4</b>	0.83	21.09	11.03	-
<b>8</b>	0.82	-	10.96	8.08 <sup>d</sup>

<sup>a</sup>Harmonic Oscillator Model of Aromaticity.<sup>18</sup> <sup>b</sup>Aromatic Stabilization Energy,<sup>19</sup> corrected aromatic stabilization enthalpies in kcal/mol obtained from toluene derivatives of each phenol analog. See SI for more details. <sup>c</sup>pK<sub>a</sub> values taken from Ref<sup>20</sup>. <sup>d</sup>pK<sub>a</sub> values taken from Ref.<sup>21</sup>

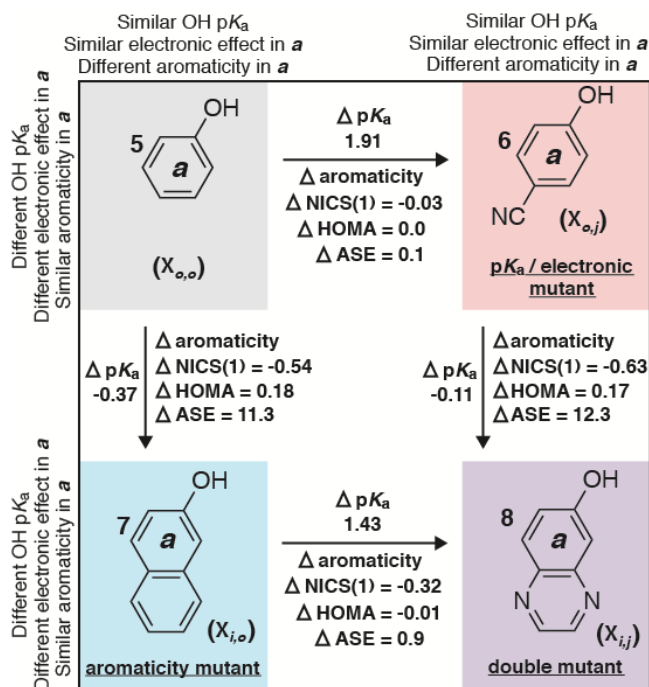
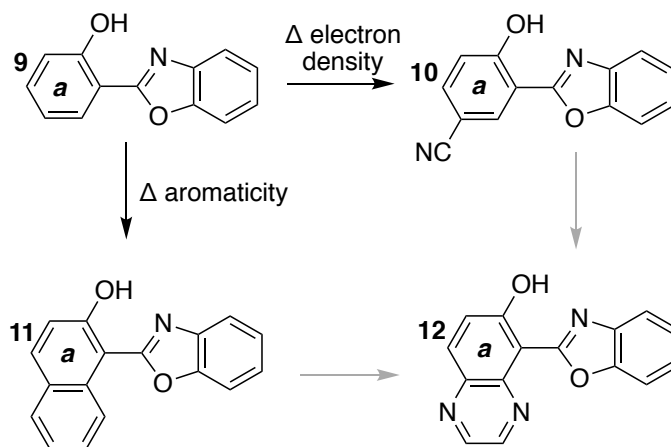


Figure 5.3 Double Mutant Cycle summary. The electron density ( $pK_a$ ) variants go left to right where the aromaticity variants go top to bottom. Full data can be found in X. Computational details and an explanation of the aromatic indices can be found in the experimental section.



Scheme 5.1 Molecules used to evaluate the role of electron density and aromaticity of *a* on ESIPT. Electron density mutants goes left to right and aromaticity mutants run top to bottom.

### Effect of Aromaticity in ESIPT

We begin by examining, qualitatively, the effect that varying the aromaticity of the phenol analog has on ESIPT spectroscopic properties. The comparison of **9** and **11** HBO analogs with respect to ESIPT has already been reported.<sup>10</sup> To summarize, **9** has a shorter absorption wavelength and a longer keto emission wavelength than **11** rendering a larger Stokes shift (Figure 5.4A). This can be rationalized with the use of Baird's rule which states that a ground state aromatic molecule becomes (anti)aromatic in the lowest lying excited-states.<sup>22</sup> Because **9** is more aromatic than **11** in the ground state, it becomes more (anti)aromatic in the excited state and thus leads to a larger excitation energy. The more (anti)aromatic **9** then has a larger change in aromaticity than **11** upon ESIPT to a nonaromatic isomer. In fact, **11** shows a small emissive hump at ~420nm which is indicative of its enol emission suggesting that there is a small energy gap between the enol and keto excited states.<sup>23</sup> Additionally, the nonaromatic isomer of **9** will be more destabilized in the ground state than the nonaromatic isomer of **11** due to **9**'s greater ground state aromaticity of ring *a*. A stabilized isomerized **9** in the excited state and a destabilized **9** in the ground state will increase the keto emission wavelength relative to that of **11**.

Interestingly, the same general pattern occurs for the comparison of **10** and **12** (Figure 5.4B). The more ground state aromatic **10** has an expected shorter wavelength absorption and a longer wavelength keto emission than **12**.

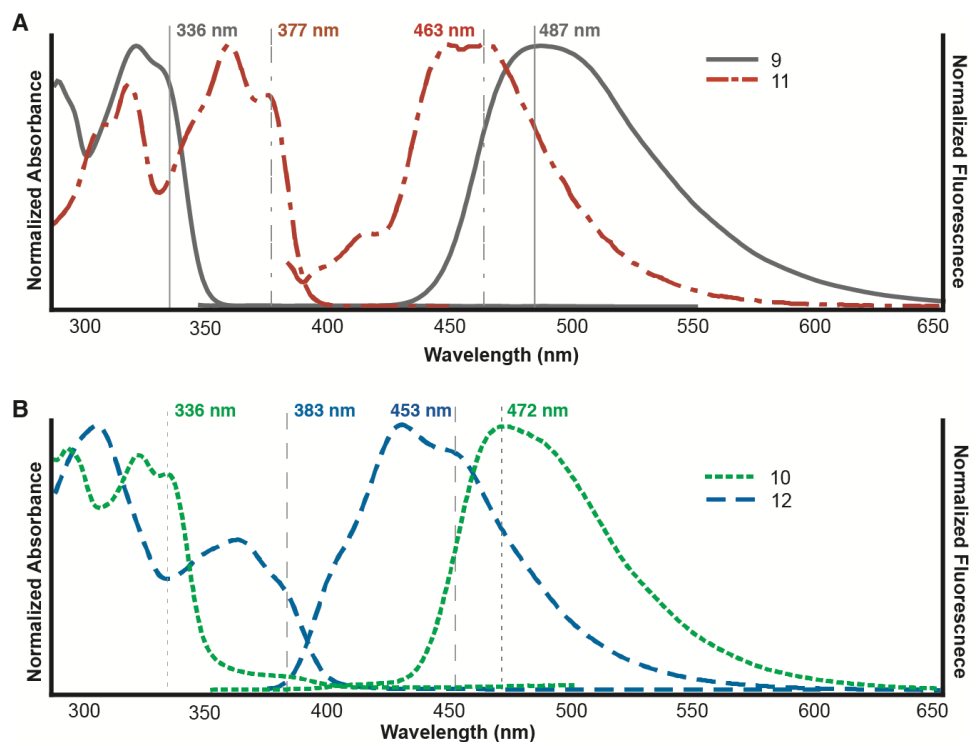


Figure 5.4 Normalized absorption and emission traces of **9-12** in toluene. (A) and (B) compare directly molecules that have the same electron density (*i.e.* same OH  $pK_a$ ) while varying the aromaticity of ring *a*.

### Effect of Acidity in ESIPT

Comparing the absorption and emission properties of **9-12** as a function of ring *a* electron density lends much subtler differences. For instance, in comparing **9** and **10**, the absorption values are identical and **9** only emits 15 nm longer than **10** (Figure 5.5A). A similar picture holds for the comparison between **11** and **12** of which the absorption and emissions are only separated by 6 and 10 nm, respectively (Figure 5.5B). It appears that the acidity of the phenol does not play a large role in the ground state properties of **9-12**. However, both of the acidity mutants (**10** & **12**) show smaller Stokes shifts which arise from their more hypsochromic keto emissions. The shorter emission wavelength is likely due to the stabilization of the ground-state isomer of both acidity mutants, where the isomer nitrogen lone pair can delocalize into the electron withdrawing moieties of **10** and **12**. This resonance stabilization suggests that it's not necessarily the acidity of

the OH that influences ESIPT, but instead the acidity of the NH that forms after ESIPT. These results emphasize the important dual role that functionalization of the 5' position has on spectral properties of HBO-based ESIPT dyes.

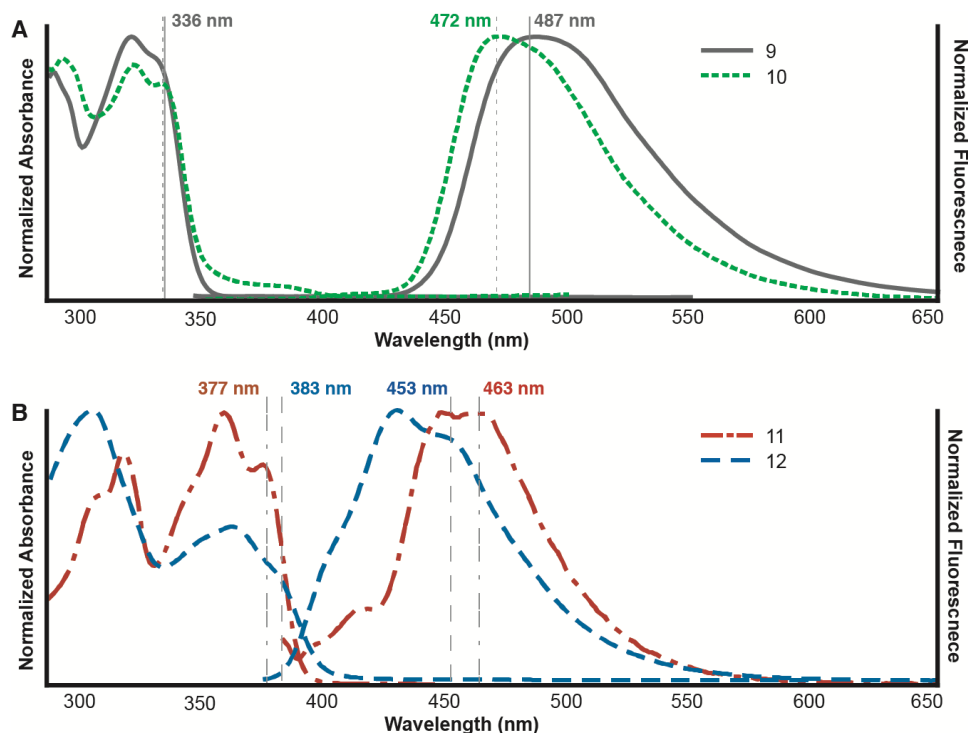


Figure 5.5 Normalized absorption and emission traces of **9-12** in toluene. (A) and (B) compare directly molecules that have the same aromaticity while varying the electron density of ring *a*.

Further, the identical absorption values for **9** and **10** validate the notion that substituents don't affect the ground state aromaticity of a molecule.<sup>24</sup> However, it was recently predicted that substituent effects can drastically influence excited-state aromaticity in the triplet state.<sup>25</sup> Therefore, the subtle differences in keto emissions between both **9/10** and **11/12** might be an artifact of substituent derived variations in excited state aromaticity. However, if this were the case, functionalization at the 4' position in HBO (para to the benzoxazole) would also see a functional group dependence on ESIPT fluorescence, which was not observed (See Ch3). Either



way, a more thorough investigation of the excited-state aromaticity of these electron density mutants by means of isotropic shielding analysis would be informative.<sup>10</sup>

### The confounding effects of Aromaticity and phenol Acidity on ESIPT Fluorescence

In evaluating the Stokes shift for **9-12**, we can compare the effects of ring *a* aromaticity and OH acidity on ESIPT fluorescence. Importantly, the differences in Stokes shift between individual mutants will shed light both the relative importance of aromaticity and acidity and, if any, possible cooperativity between the two.

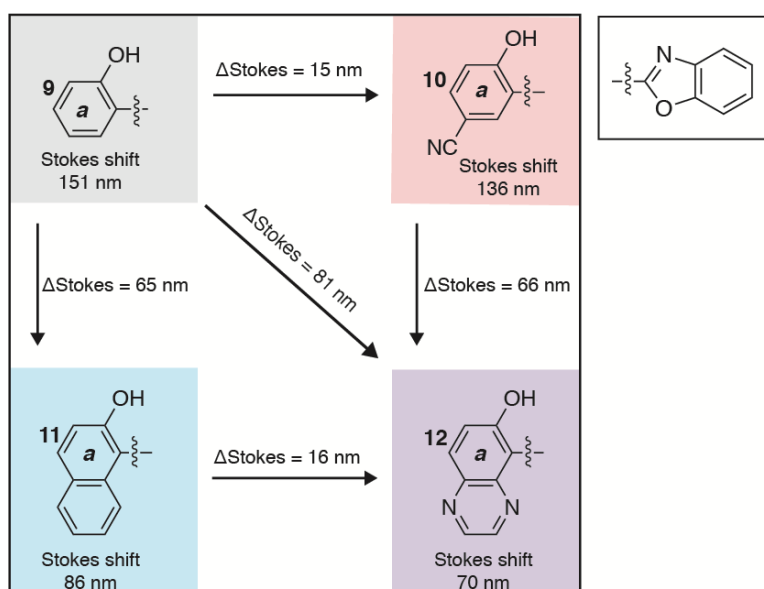


Figure 5.6 Experimental Stokes shifts of HBO analogs in the proposed DMC analysis where the  $pK_a$  mutants run right to left and the aromaticity mutants run top to bottom.

On the surface, it's clear that changing the aromaticity of ring *a* influences the Stokes shift more dramatically than varying the acidity of the hydroxyl group (65 nm vs. 15 nm). What's interesting is that the  $\Delta$ Stokes shift for both sets of aromaticity variants (**9&11**, **10&12**) are nearly equal (Figure 5.6). Further, the  $\Delta$ Stokes shift for both sets of  $pK_a$  variants (**9&10**, **11&12**) are also nearly equal. This would imply that, because the parallel mutations are commensurate, that aromaticity and phenol  $pK_a$  function independently in the ESIPT

mechanism. Another way of analyzing the data in X with respect to a DMC is that the Stokes shift difference between the double mutant (**12**→**9**, 81 nm) is near equal to the sum of the individual mutants (**10**→**9**, 15 nm, and **11**→**9**, 65 nm) indicating that the aromaticity of ring **a** and OH acidity are additive effects in ESIPT fluorescence.<sup>12-14, 16</sup>

On one hand, additivity is to be expected. Aromaticity differences in the excited state are greater than in the ground state and therefore aromatic effects in ESIPT are going to exist largely in the excited state.<sup>10</sup> Another way to say this is that the need for ring **a** to relieve excited-state (anti)aromaticity and isomerize to a nonaromatic isomer is *greater* than the need to isomerize from a ground state nonaromatic isomer to regain its ground state aromaticity. The effect of the 5' substituent (which happens to increase the hydroxyl acidity) functions largely in stabilizing the ground state nonaromatic isomer.<sup>26</sup> This occurs through resonance stabilization of the newly conjugated lone pair of the amine that resulted from the excited state isomerization (Figure 5.7A). Although, it is perplexing, conceptually at least, that there isn't observed interaction between the ground state resonance stabilization and the re-aromatization of ring **a**.

### Conclusion

Inspired by the double mutant cycle analysis most often employed in structural biology, we developed an experimental analysis that systematically explores the effects of a ring's aromaticity and its electron density (as measured by a phenol moiety hydroxyl group  $pK_a$ ) on some experimental parameter. This was done by identifying four molecules that vary in either their aromaticity (2-naphthol, **7**), hydroxyl acidity (4-cyanophenol, **6**), or both (quinoxalin-6-ol, **8**) when compared to the base molecule, phenol, **5**.

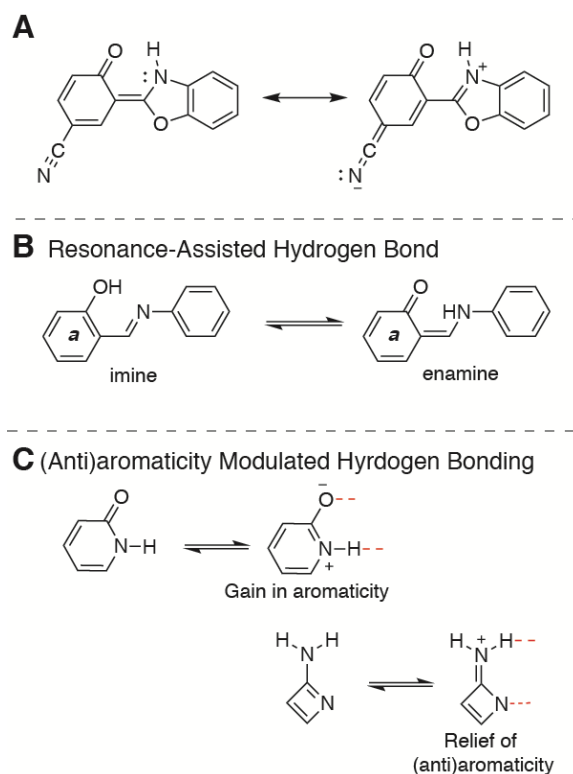


Figure 5.7 (A) Resonance stabilization of the non-aromatic isomer by delocalization of the nitrogen lone pair into the 5' electron withdrawing group. (B) An example of a RAHB where phenol aromaticity (*a*) and OH acidity dictates imine/enamine equilibrium. (C) Examples of AMHB where either a gain in ring aromaticity or relief in ring (anti)aromaticity strengthens hydrogen bonding.

We applied this experimental method to examine the interplay between the phenol aromaticity and acidity in ESIPT fluorescence. Both of these factors have been shown to influence the Stokes shift on the ESIPT spectral properties of HBO related chromophores. In analyzing the Stokes shifts of **9-12** in toluene, the data suggests that an HBO ESIPT dye's aromaticity in ring *a* and its hydroxyl  $pK_a$  function independently with respect to the excited state isomerization. While this observation can be rationalized to some degree, it was certainly not expected. This is also not to say that the proposed DMC-like analysis is adequate for studying the spectral properties of ESIPT dyes or that the Stokes shift of these dyes are the right experimental output to measure. However, at the very least, this is an interesting observation in

ESIPT fluorescence and warrants further exploration. Additionally our experimental analysis is, at least we believe, both a novel and creative way to tease apart the relationship between two fundamental descriptors of organic molecules.

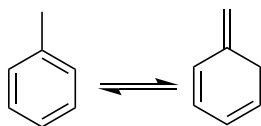
Ultimately, for this method to be validated, it needs to be tested against other chemical systems. For example, the strength of Resonance-Assisted Hydrogen Bonds (RAHB) and their relative equilibrium between imine/enamine tautomers, have been cited to be influenced by both the acidity<sup>27, 28</sup> and the aromaticity of the phenol (Figure 5.7B).<sup>21</sup> Additionally, (Anti)aromaticity Modulated Hydrogen Bonding (AHMB), where hydrogen bond strength increases if either a gain in aromaticity or a loss of (anti)aromaticity occurs, could be explored (Figure 5.7C).<sup>29-31</sup> A proton donor's  $pK_a$  has been related to hydrogen bond strength<sup>32</sup> and based the miniature thought experiment above (Figure 5.1B), it's reasonable to postulate that a molecule that gains *more* aromaticity upon hydrogen bonding will form a *stronger* hydrogen bond and vice versa. Another way to validate the above method (and conclusions pertaining to tuning ESIPT fluorescence) is to apply these design rules towards new ESIPT chromophores. If anything, chemically reducing the degree of aromaticity of ring *a* to reduce the experimental Stokes shift can be viewed as a *loss of function*. The true test would be to obtain a *gain in function* by increasing the ground state aromaticity to be greater than that of benzene – a feat that cannot be done.<sup>33</sup> In the meantime, however, the results from this study will inform ESIPT chromophore design for its ever increasing number of applications.

## Experimental Details

### Computational Details

All calculations were done using the Gaussian 16 suite of programs.<sup>34</sup> All geometry optimizations and frequency analyses were done using the M06-2X/6-311++g(d,p) level of theory. HOMA calculations were done using an  $R_{opt}$  value of 1.388 Å and an  $\alpha$  value of 257.7.<sup>18</sup>

Aromatic stabilization energies (ASE) are reported as  $\Delta H$  of tautomerization to gain aromaticity as shown below.<sup>19</sup> All structures used for the ASE calculations had a methyl where the phenol hydroxyl group would be.



All NICS(1) values are reported as literature precedent where the value represents the negative isotropic shielding value of a neutral ghost atom located 1 Å above the ring in question.<sup>35</sup> The more negative the value, the more aromatic the ring is.

### Computed Coordinates

#### Benzene, 1

	X	Y	Z
C	-0.994202	-0.977593	0.000002
C	0.349671	-1.349653	0.000057
C	1.343782	-0.372181	-0.000051
C	0.994117	0.977682	0.000006
C	-0.349554	1.349682	0.000053
C	-1.343815	0.372065	-0.000048
H	-1.76716	-1.737993	-0.000062
H	0.621375	-2.399371	0.000081
H	2.388745	-0.661495	-0.00012
H	1.767264	1.737882	0.000021
H	-0.621507	2.39933	-0.000002
H	-2.388713	0.661636	-0.000035

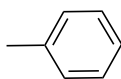
Energy -232.3113 Hartree

#### Phenol, 5

	X	Y	Z
C	-0.221265	-1.219262	0
C	1.166594	-1.186306	-0.000005
C	1.849725	0.027252	0.000002
C	1.127371	1.214856	-0.000001

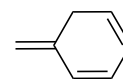
C	-0.263548	1.195473	0
C	-0.93571	-0.024127	0.000003
H	-0.768054	-2.153817	0.000005
H	1.719214	-2.118529	-0.000004
H	2.93207	0.046142	0.000009
H	1.645668	2.166479	0
H	-0.825888	2.124006	0.000004
O	-2.295517	-0.110305	0.000004
H	-2.677872	0.77085	-0.00004

Energy -307.4230 Hartree



	X	Y	Z
C	-0.193003	1.199476	-0.00815
C	1.198357	1.200277	0.001989
C	1.89708	-0.001884	0.007557
C	1.194092	-1.202686	0.001993
C	-0.196216	-1.197446	-0.008204
C	-0.90937	0.002556	-0.010404
H	-0.732102	2.141245	-0.016529
H	1.73668	2.141002	0.001626
H	2.980446	-0.003701	0.012459
H	1.729739	-2.144944	0.00162
H	-0.738738	-2.137452	-0.016493
C	-2.416422	0.000854	0.008593
H	-2.816526	-0.825084	-0.582127
H	-2.789669	-0.111602	1.030319
H	-2.816936	0.933654	-0.391119

Energy -271.5052 Hartree



	X	Y	Z
C	-1.026885	0.013516	0.034472
C	-0.270961	1.264612	0.138271
C	1.068449	1.275448	0.049072
C	1.82311	0.038386	-0.165491
C	1.215982	-1.149745	-0.105207
C	-2.340704	0.011429	-0.213872
H	-2.893898	-0.913164	-0.333849
C	-0.242176	-1.263365	0.24948
H	-0.299142	-1.520935	1.318181
H	-0.71351	-2.09189	-0.284253
H	-2.89366	0.939921	-0.301387
H	-0.829478	2.19079	0.2255
H	1.609982	2.213634	0.089117
H	2.883652	0.106768	-0.378015
H	1.77516	-2.066804	-0.255643

Energy -271.4509 Hartree

## Benzonitrile, 2

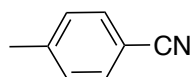
Symbol	X	Y	Z
C	-1.477672	-1.206966	0.000032
C	-0.089532	-1.21313	0.000003
C	0.602778	-0.000025	-0.000013
C	-0.089507	1.213119	0.000003
C	-1.477629	1.206992	0.000033
C	-2.170516	0.000014	0.000046
H	-2.019117	-2.144902	0.000044
H	0.463142	-2.144208	-0.000009
H	0.463216	2.144168	-0.00001
H	-2.019074	2.144928	0.000044
H	-3.25385	0.000043	0.000068
C	2.04055	-0.000022	-0.000045
N	3.190693	0.000011	-0.000071

Energy -324.4377

## 4-Cyanophenol, 6

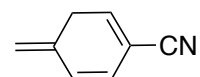
Symbol	X	Y	Z
C	-1.005774	1.221208	0.000003
C	0.37674	1.212359	-0.000001
C	1.073346	-0.00117	-0.000003
C	0.368236	-1.205584	0
C	-1.017823	-1.198919	0.000003
C	-1.705154	0.01423	0.000005
H	-1.564729	2.148128	0.000005
H	0.928251	2.144167	-0.000003
H	0.90918	-2.143496	-0.000002
H	-1.566396	-2.134867	0.000004
O	-3.057653	0.086242	0.000008
H	-3.439439	-0.795873	0.000024
C	2.507891	-0.008703	-0.000008
N	3.658512	-0.015502	-0.000012

Energy -399.6635 Hartree



	X	Y	Z
C	-0.973016	1.201632	-0.009209
C	0.414292	1.209693	-0.002861
C	1.111279	0.000312	0.000997
C	0.412315	-1.209061	-0.002871
C	-0.973927	-1.199118	-0.009271
C	-1.68679	0.002142	-0.009654
H	-1.511756	2.142723	-0.015808
H	0.962305	2.143686	-0.004088
H	0.959469	-2.14356	-0.004109
H	-1.514438	-2.139405	-0.015821
C	-3.191854	-0.001269	0.013147
H	-3.591862	-0.829228	-0.574076
H	-3.557135	-0.114132	1.037624
H	-3.594957	0.93086	-0.384232
C	2.54783	-0.000746	0.00437
N	3.69823	-0.001779	0.007517

Energy -636.7454 Hartree



	X	Y	Z
C	1.787104	-0.042503	-0.011376
C	0.998661	-1.26496	0.166132
C	-0.340352	-1.236894	0.198484
C	-1.060321	0.036099	0.041506
C	-0.409095	1.208419	0.036628
C	3.0724	-0.090792	-0.372268
H	3.647519	0.811049	-0.548384
C	1.07278	1.264115	0.261352
H	1.22476	1.527893	1.319391
H	1.520319	2.075368	-0.316819
H	3.580001	-1.039917	-0.500891
H	1.528405	-2.210248	0.2133
H	-0.922239	-2.145457	0.290302
H	-0.956071	2.137663	-0.074459
C	-2.488319	-0.002763	-0.113042
N	-3.631405	-0.054382	-0.23242

Energy -363.6911 Hartree

### Naphthalene, 3

	X	Y	Z
C	2.423958	-0.707878	-0.000001
C	1.241352	-1.39815	0
C	0.000007	-0.710516	0.000001
C	0	0.710519	0.000001
C	1.241353	1.398148	0.000001
C	2.423956	0.707879	-0.000001
H	-1.236102	-2.482949	0.000004
H	3.366102	-1.243031	-0.000001
H	1.236114	-2.482944	-0.000001
C	-1.241361	-1.398153	0.000001
C	-1.241361	1.398156	0.000001
H	1.236116	2.482945	-0.000002
H	3.366103	1.243028	-0.000002
C	-2.423953	0.707883	-0.000001
C	-2.423953	-0.707887	-0.000001



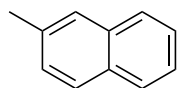
H	-1.236111	2.48295	0.000004
H	-3.366108	1.243018	-0.000004
H	-3.366106	-1.243024	-0.000001

Energy -315.8154 Hartree

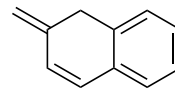
## 2-Naphthol, 7

	X	Y	Z
C	2.685852	-1.000178	0.000002
C	1.409697	-1.496319	0
C	0.290625	-0.621425	-0.000001
C	0.523329	0.781216	-0.000001
C	1.85671	1.264861	-0.000002
C	2.915553	0.396974	0
H	-1.230283	-2.176162	-0.000005
H	3.530317	-1.679322	0.000005
H	1.234411	-2.566585	0.000002
C	-1.038278	-1.109779	-0.000004
C	-0.593988	1.653624	0
H	2.022052	2.337114	-0.000005
H	3.931074	0.773915	0.000002
C	-1.87092	1.162564	0.000004
C	-2.093776	-0.236679	0
H	-0.423626	2.724778	0
H	-2.720573	1.838451	0.000008
O	-3.356603	-0.748299	0.000006
H	-3.999376	-0.034942	-0.000051

Energy -461.0394 Hartree



	X	Y	Z
C	-2.69359	-1.046963	0.000003
C	-1.404553	-1.511617	-0.000007
C	-0.3091	-0.610692	-0.000004
C	-0.569614	0.785101	0.000011
C	-1.913226	1.237524	0.000018



	X	Y	Z
C	2.686312	-0.969147	-0.149979
C	1.398719	-1.472221	0.021327
C	0.311296	-0.616542	0.146352
C	0.516815	0.77097	0.09015
C	1.811074	1.268478	-0.075364

C	-2.951996	0.344016	0.000014	C	2.893437	0.405394	-0.193504
H	1.223248	-2.132617	-0.000043	H	3.523379	-1.650242	-0.247195
H	-3.522848	-1.744413	0.000003	H	1.238375	-2.544965	0.060642
H	-1.203733	-2.577775	-0.000018	C	-0.638122	1.669984	0.157739
C	1.037408	-1.062573	-0.000023	H	1.963288	2.341959	-0.118764
C	0.532182	1.681012	0.000016	H	3.892857	0.803045	-0.323355
H	-2.103999	2.305558	0.000025	C	-1.897496	1.215896	0.078419
H	-3.975672	0.699129	0.000018	C	-2.186216	-0.217009	-0.025361
C	1.81565	1.210851	0.000003	H	-0.44177	2.736434	0.201674
C	2.090335	-0.184873	-0.000002	H	-2.732134	1.907896	0.036241
H	0.337769	2.748442	0.000026	C	-1.078524	-1.140706	0.4231
H	2.648321	1.907058	0.000006	H	-1.209857	-2.137022	-0.004018
C	3.519718	-0.656375	-0.000011	H	-1.170819	-1.248461	1.513573
H	4.050415	-0.285926	-0.88091	C	-3.37091	-0.665735	-0.449633
H	4.050175	-0.286645	0.881337	H	-3.570952	-1.725873	-0.555142
H	3.577034	-1.74527	-0.000443	H	-4.17067	0.021067	-0.703129
Energy -425.1227 Hartree				Energy -425.0873 Hartree			

## Quinoxaline, 4

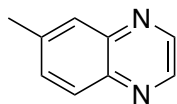
	X	Y	Z
C	2.308739	-0.711468	0.000008
C	0.042856	-0.709368	-0.000005
C	0.042868	0.709394	-0.000008
C	2.30875	0.711457	0.000009
H	-1.159741	-2.488969	0.000006
H	3.250615	-1.252573	0.00001
C	-1.189896	-1.40631	0.000004
C	-1.189907	1.406314	0.000002
H	3.250623	1.252565	0.000007
C	-2.368003	0.70873	0.000002
C	-2.368005	-0.708745	0.000003
H	-1.159802	2.488975	-0.000002
H	-3.311888	1.24031	0.000001
H	-3.311893	-1.240317	0.000004
N	1.208411	1.413599	-0.000005
N	1.2084	-1.413602	-0.000011
Energy -417.8943 Hartree			

quinoxalin-6-ol, **8**

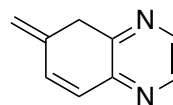
	X	Y	Z
C	2.561914	-0.995841	-0.000005
C	0.324645	-0.628524	0.000004
C	0.563418	0.771863	0.000004
C	2.797891	0.40677	-0.000004
H	-1.168746	-2.189407	-0.000003
H	3.402862	-1.683676	-0.000007
C	-0.997848	-1.120827	-0.000003
C	-0.541677	1.65675	-0.000002
H	3.815218	0.786316	-0.000007
C	-1.816368	1.16338	-0.000001
C	-2.046663	-0.237675	-0.000004
H	-0.342241	2.721341	-0.000001
H	-2.665519	1.83992	0.000001
O	-3.309209	-0.738388	0.000004
H	-3.950519	-0.023307	-0.000024
N	1.824421	1.277771	0.000005
N	1.362826	-1.511979	0.000005

Energy

-493.1185 Hartree



	X	Y	Z
C	2.569008	-1.041874	0.000002
C	0.342901	-0.618604	-0.000004
C	0.60997	0.773996	0.000004
C	2.835241	0.354427	0
H	-1.164381	-2.146023	-0.000023
H	3.393525	-1.749136	0.000006
C	-0.998823	-1.074395	-0.000012
C	-0.477697	1.683077	0.000002
H	3.861365	0.710518	0.000015
C	-1.759972	1.211297	-0.000005
C	-2.042333	-0.185443	-0.000009
H	-0.253636	2.743104	0.000002
H	-2.591698	1.908435	-0.000009
C	-3.47497	-0.644833	0.000012



	X	Y	Z
C	2.571711	-0.962669	-0.141059
C	0.349024	-0.625425	0.12623
C	0.56047	0.766393	0.072823
C	2.784407	0.409606	-0.171467
H	3.397131	-1.659261	-0.23945
C	-0.584443	1.675465	0.13616
H	3.783553	0.816773	-0.284325
C	-1.842755	1.216325	0.073762
C	-2.14351	-0.215774	-0.014924
H	-0.359558	2.735112	0.163899
H	-2.676733	1.909412	0.034454
C	-1.034207	-1.159162	0.38816
H	-1.142226	-2.137455	-0.081593
H	-1.1069	-1.318369	1.473468

H	-4.000705	-0.268727	0.881289	C	-3.34791	-0.648786	-0.39762
H	-4.000895	-0.268235	-0.88094	H	-3.564301	-1.706071	-0.49785
H	-3.54131	-1.732752	-0.000278	H	-4.147031	0.048785	-0.621434
N	1.883616	1.249752	0.000006	N	1.352004	-1.483581	0.014128
N	1.356069	-1.527333	-0.000006	N	1.782188	1.280043	-0.06835
Energy	-457.2022 Hartree			Energy	-497.1683 Hartree		

## References

1. A. S. Mahadevi and G. N. Sastry, *Chemical Reviews*, 2016, **116**, 2775-2825.
2. W. R. Carroll, C. Zhao, M. D. Smith, P. J. Pellechia and K. D. Shimizu, *Organic Letters*, 2011, **13**, 4320-4323.
3. D. Vijay, H. Zipse and G. N. Sastry, *The Journal of Physical Chemistry B*, 2008, **112**, 8863-8867.
4. T. M. Krygowski, J. E. Zachara-Horeglad, M. Palusiak, S. Pelloni and P. Lazzeretti, *The Journal of Organic Chemistry*, 2008, **73**, 2138-2145.
5. P. Zhou and K. Han, *Acc Chem Res*, 2018, **51**, 1681-1690.
6. A. S. Klymchenko, *Acc Chem Res*, 2017, **50**, 366-375.
7. J. Zhao, S. Ji, Y. Chen, H. Guo and P. Yang, *Physical Chemistry Chemical Physics*, 2012, **14**, 8803-8817.
8. C. Azarias, S. Budzak, A. D. Laurent, G. Ulrich and D. Jacquemin, *Chem Sci*, 2016, **7**, 3763-3774.
9. Y. Houari, A. Charaf-Eddin, A. D. Laurent, J. Massue, R. Ziessel, G. Ulrich and D. Jacquemin, *Phys Chem Chem Phys*, 2014, **16**, 1319-1321.
10. B. J. Lampkin, Y. H. Nguyen, P. B. Karadakov and B. VanVeller, *Phys Chem Chem Phys*, 2019, **21**, 11608-11614.
11. C.-H. Wu, L. J. Karas, H. Ottosson and J. I.-C. Wu, 2019, 20303-20308.
12. P. J. Carter, G. Winter, A. J. Wilkinson and A. R. Fersht, *Cell*, 1984, **38**, 835-840.
13. A. Horovitz and A. R. Fersht, *Journal of Molecular Biology*, 1990, **214**, 613-617.
14. A. Camara-Campos, D. Musumeci, C. A. Hunter and S. Turega, *Journal of the American Chemical Society*, 2009, **131**, 18518-18524.
15. M. S. Ardejani, E. T. Powers and J. W. Kelly, *Accounts of Chemical Research*, 2017, **50**, 1875-1882.
16. S. L. Cockroft and C. A. Hunter, *Chemical Society Reviews*, 2007, **36**, 172-188.
17. M. Solà, *Frontiers in Chemistry*, 2017, **5**, 22.
18. T. M. Krygowski, H. Szatyłowicz, O. A. Stasyuk, J. Dominikowska and M. Palusiak, *Chem Rev*, 2014, **114**, 6383-6422.
19. P. v. R. Schleyer and F. Pühlhofer, *Organic Letters*, 2002, **4**, 2873-2876.

20. W. M. Haynes, D. R. Lide and T. J. Bruno, *CRC handbook of chemistry and physics: a ready-reference book of chemical and physical data*, CRC Press, Boca Raton, Florida, 97 edn., 2016.
21. Y. H. Nguyen, B. J. Lampkin, A. Venkatesh, A. Ellern, A. J. Rossini and B. VanVeller, *J Org Chem*, 2018, **83**, 9850-9857.
22. N. C. Baird, *Journal of the American Chemical Society*, 1972, **94**, 4941-&.
23. C. Azarias, Š. Budzák, A. D. Laurent, G. Ulrich and D. Jacquemin, *Chemical Science*, 2016, **7**, 3763-3774.
24. T. M. Krygowski, K. Ejsmont, B. T. Stepień, M. K. Cyrański, J. Poater and M. Solà, *The Journal of Organic Chemistry*, 2004, **69**, 6634-6640.
25. M. Baranac-Stojanović, *The Journal of Organic Chemistry*, 2020, **85**, 4289-4297.
26. T. Mutai, H. Sawatani, T. Shida, H. Shono and K. Araki, *The Journal of Organic Chemistry*, 2013, **78**, 2482-2489.
27. E. D. Raczyńska, W. Kosińska, B. Ośmiałowski and R. Gawinecki, *Chemical Reviews*, 2005, **105**, 3561-3612.
28. G. Pareras, M. Palusiak, M. Duran, M. Solà and S. Simon, *The Journal of Physical Chemistry A*, 2018, **122**, 2279-2287.
29. T. Kakeshpour, J. P. Bailey, M. R. Jenner, D. E. Howell, R. J. Staples, D. Holmes, J. I. Wu and J. E. Jackson, *Angewandte Chemie International Edition*, 2017, **56**, 9842-9846.
30. T. Kakeshpour, J. I. Wu and J. E. Jackson, *Journal of the American Chemical Society*, 2016, **138**, 3427-3432.
31. J. I. Wu, J. E. Jackson and P. v. R. Schleyer, *Journal of the American Chemical Society*, 2014, **136**, 13526-13529.
32. P. Gilli, L. Pretto, V. Bertolasi and G. Gilli, *Accounts of Chemical Research*, 2009, **42**, 33-44.
33. R. Hoffmann, *American Scientist*, 2015, **103**, 18.

34. M. J. Frisch, G. W. Trucks, H. B. Schlegel, G. E. Scuseria, M. A. Robb, J. R. Cheeseman, G. Scalmani, V. Barone, G. A. Petersson, H. Nakatsuji, X. Li, M. Caricato, A. V. Marenich, J. Bloino, B. G. Janesko, R. Gomperts, B. Mennucci, H. P. Hratchian, J. V. Ortiz, A. F. Izmaylov, J. L. Sonnenberg, Williams, F. Ding, F. Lipparini, F. Egidi, J. Goings, B. Peng, A. Petrone, T. Henderson, D. Ranasinghe, V. G. Zakrzewski, J. Gao, N. Rega, G. Zheng, W. Liang, M. Hada, M. Ehara, K. Toyota, R. Fukuda, J. Hasegawa, M. Ishida, T. Nakajima, Y. Honda, O. Kitao, H. Nakai, T. Vreven, K. Throssell, J. A. Montgomery Jr., J. E. Peralta, F. Ogliaro, M. J. Bearpark, J. J. Heyd, E. N. Brothers, K. N. Kudin, V. N. Staroverov, T. A. Keith, R. Kobayashi, J. Normand, K. Raghavachari, A. P. Rendell, J. C. Burant, S. S. Iyengar, J. Tomasi, M. Cossi, J. M. Millam, M. Klene, C. Adamo, R. Cammi, J. W. Ochterski, R. L. Martin, K. Morokuma, O. Farkas, J. B. Foresman and D. J. Fox, *Journal*, 2016.
35. Z. Chen, C. S. Wannere, C. Corminboeuf, R. Puchta and P. Schleyer, *Chem Rev*, 2005, **105**, 3842-3888.

## CHAPTER 6. GENERAL CONCLUSIONS

The work presented in this dissertation is focused on the Excited-State Intramolecular Proton Transfer (ESIPT) fluorescent pathway of 2-(2'-hydroxyphenyl)benzoxazole (HBO) chromophores. ESIPT has been known for decades and the ESIPT capabilities of HBO have been known for a little less. Despite being an already thoroughly studied system, the functional group tolerance and main driving forces to ESIPT were unclear. Furthermore, the applications of ESIPT dyes, although existent, are scarce, and in my opinion, do not take full advantage of the unique properties ESIPT dyes possess. This work is the culmination of my attempts to address these unknowns in ESIPT fluorescence and showcase its effectiveness as fluorescent probe. In a way, the organization of this dissertation is backwards where the application of an ESIPT dye preceded the mechanistic studies. However, it was the, what could be considered a naïve approach, and puzzling observations that inspired the rest of this work.

Having fluorogenic dye/protein complexes is critical to elucidating biological processes. ESIPT fluorescence is an attractive mechanism of fluorogenicity for biological applications. Its dual emission and thus ratiometric output as well as its large Stokes shift achieved after excited state isomerization sets it apart from many other organic chromophores. However, use of ESIPT dyes in biological applications often relied on nonspecific interactions with a protein target that resulted in poor *turn-on* keto emission. In adapting a protein that already bound a benzoxazole core with high affinity, we demonstrated that coupling binding site mutagenesis with HBO chromophore engineering, *turn-on* fluorescence was achieved upon probe binding. Further, we showed that this *turn-on* fluorescence upon binding was coupled to a *turn-off* of the blue-shifted enol emission channel thus validating ESIPT potential for ratiometric sensing. This study will be



the foundations towards developing a fluorescent risk-factor diagnostic of TTR amyloidosis which will aim to enable rapid and large scale screening populations prone to amyloidosis.

In the design of the HBO chromophores to bind an engineered TTR pocket, we quickly realized that the functional group tolerance of HBO scaffolds was not well characterized. A few standalone studies have been conducted on HBO dyes but generalized design principles were limited to computational studies. We sought to address this void by studying the photophysical properties of 25 unique, monosubstituted HBO dyes across four different solvents to characterize both the solvent and electronic coordinates that influence ESIPT photochemistry. While only a few comprehensible trends emerged, we found that substitution in the 5' position (para to the phenol hydroxy group) had the greatest effect on all aspects of ESIPT fluorescence of HBO chromophores. Interestingly, to our knowledge, functionalization at the 5' position is rare in the literature suggesting that the influence of this position is not well known. More electron withdrawing groups increase the ratio of keto to enol emission whereas more electron donating groups increases the Stokes shift of the keto emission channel. Additionally, when a cyano group is at the 5' position, HBO quantum yield of fluorescence is 0.15 which is among the brightest HBO dyes known in free solution!

Aside from the functional group tolerance, we were intrigued by the excited state isomerization. What was unclear was that for ESIPT to occur, the excited state isomerization is clearly an energetically favorable process. However, the HBO dye isomerizes from an aromatic molecule to being nonaromatic. Several reports in the literature suggested that aromaticity plays a roll but no explanation was provided. We demonstrated, both theoretically and experimentally, that ESIPT works as a function of Baird's rule – where a ground state aromatic molecule becomes (anti)aromatic in the lowest lying excited state, and vice versa. Although previously

defined only for the lowest triplet state, this study was the first demonstration that Baird's rule is effective for the first singlet state. This study also demonstrated that there is a complementarity to Baird's rule. In using HBO and a Naphthalene derivative of HBO, we showed that the more ground state aromatic a molecule is, the more excited state that same molecule becomes in the excited state. We used this design principle to rationalize the photophysical behavior of Naphthalene derived HBO analogs of which was not previously described.

The prior two studies demonstrated the importance of the 5' substituent (effectively the acidity of the phenol OH) and phenol aromaticity in ESIPT photophysics. Because both a ring's electron density and aromaticity exist in the cyclic  $\pi$  system, we postulated that these two effects are interrelated. We therefore designed an experimental system that systematically alters the ring's aromaticity and the ring's electron density to evaluate any co-dependency, if any. This experimental system resembles a double mutant cycle where each factor of interest is mutated individual and then simultaneously. Where this system differentiates from the traditional double mutant cycle used in structural biology is that it explores the effects of effectively two intramolecular interactions. The results from this study suggest that the ring electron density and aromaticity function independently of one another with respect to ESIPT fluorescence

Overall, I anticipate that this dissertation will inform the future design of ESIPT HBO chromophores for its continued use in biological and material science applications. Much as an intimate knowledge of an organic reaction mechanism allows for the improvement of its methodology, knowledge of the ESIPT fluorescent mechanism will better inform the design and synthesis of brighter and more robust ESIPT dyes. It is my hope that the continued development of ESIPT dyes will lead to a greater use by the chemical community.